2019

LIGNIN-DERIVED CARBON AND NANOCOMPOSITE MATERIALS FOR ENERGY STORAGE APPLICATIONS

Wenqi Li
University of Kentucky, wenqi.li@uky.edu
Digital Object Identifier: https://doi.org/10.13023/etd.2020.002

Recommended Citation

Li, Wenqi, "LIGNIN-DERIVED CARBON AND NANOCOMPOSITE MATERIALS FOR ENERGY STORAGE APPLICATIONS" (2019). *Theses and Dissertations--Biosystems and Agricultural Engineering*. 68.
https://uknowledge.uky.edu/bae_etds/68

STUDENT AGREEMENT:

I represent that my thesis or dissertation and abstract are my original work. Proper attribution has been given to all outside sources. I understand that I am solely responsible for obtaining any needed copyright permissions. I have obtained needed written permission statement(s) from the owner(s) of each third-party copyrighted matter to be included in my work, allowing electronic distribution (if such use is not permitted by the fair use doctrine) which will be submitted to UKnowledge as Additional File.

I hereby grant to The University of Kentucky and its agents the irrevocable, non-exclusive, and royalty-free license to archive and make accessible my work in whole or in part in all forms of media, now or hereafter known. I agree that the document mentioned above may be made available immediately for worldwide access unless an embargo applies.

I retain all other ownership rights to the copyright of my work. I also retain the right to use in future works (such as articles or books) all or part of my work. I understand that I am free to register the copyright to my work.

REVIEW, APPROVAL AND ACCEPTANCE

The document mentioned above has been reviewed and accepted by the student’s advisor, on behalf of the advisory committee, and by the Director of Graduate Studies (DGS), on behalf of the program; we verify that this is the final, approved version of the student’s thesis including all changes required by the advisory committee. The undersigned agree to abide by the statements above.

Wenqi Li, Student

Dr. Jian Shi, Major Professor

Dr. Donald Colliver, Director of Graduate Studies

LIGNIN-DERIVED CARBON AND NANOCOMPOSITE MATERIALS FOR ENERGY STORAGE APPLICATIONS

DISSERTATION

A dissertation submitted in partial fulfillment of the
requirements for the degree of Doctor of Philosophy in the
Colleges of Agriculture and Engineering
at the University of Kentucky

By
Wenqi Li
Lexington, Kentucky
Advisor: Dr. Jian Shi, Assistant Professor of Biosystems and Agricultural Engineering
Lexington, Kentucky
2019

ABSTRACT OF DISSERTATION

LIGNIN-DERIVED CARBON AND NANOCOMPOSITE MATERIALS FOR ENERGY STORAGE APPLICATIONS

With a growing demand for electrical energy storage materials, lignin-derived carbon materials have received increasing attention in recent years. As a highly abundant renewable carbon source, lignin can be converted to a variety of advanced carbon materials with tailorable chemical, structural, mechanical and electrochemical properties through thermochemical conversion (e.g. pyrolysis). However, the non-uniformity in lignin structure, composition, inter-unit linkages and reactivity of diverse lignin sources greatly influence lignin fractionation from plant biomass, the pyrolysis chemistry, and property of the resulting carbon materials.

To introduce a better use of lignocellulosic biomass to biofuels and co-products, it is necessary to find novel ways to fractionate lignin and cellulose from the feedstock at high efficacy and low cost. Deep eutectic solvent (DES) was used to extract lignin from high lignin-content walnut and peach endocarps. Over 90% sugar yields were achieved during enzymatic hydrolysis of DES pretreated peach and walnut endocarps while lignins were extracted at high yields and purity. The molecular weights of the extracted lignin from DES pretreated endocarp biomass were significantly reduced. The native endocarp lignins were SGH type lignins with dominant G-unit. DES pretreatment decreased the S and H-unit which led to an increase in condensed G-units, which may contribute to a higher thermal stability of the isolated lignin.

Lignin slow pyrolysis was investigated using a commercial pyrolysis–GC/MS system for the first time to link pyrolysis chemistry and carbon material properties. The overall product distributions, including volatiles and solid product were tracked at different heating rates (2, 20, 40 ℃/min) and different temperature regions (100-200, 200-300 and 300-600 ℃). Results demonstrate that changes in reaction chemistry as a factor of pyrolysis conditions led to changes in yield and properties of the resulting carbon materials. Physical and chemical properties of the resulting carbon material, such as porosity, chemical composition and surface functional groups were greatly affected by lignin slow pyrolysis temperature and heating rate.

Lignin-derived activated carbons (AC) were synthesized from three different lignin sources: poplar, pine derived alkaline lignin and commercial kraft lignin under identical conditions. The poplar lignin-derived ACs exhibited a larger surface area and total mesopore volume than softwood lignin-derived AC, which contribute to a larger electrochemical capacitance over a range of scan rates. The presence of oxygen-containing functional groups in all lignin-derived ACs, which participated in redox reaction and thus contributed to an additional pseudo-capacitance. By delineating the carbonization and activation parameters, results from this study suggest that lignin structure and composition are important factors determining the pore structure and electrochemical properties of the derived carbon materials.

A 3-dimensional, interconnected carbon/silicon nanoparticles composite synthesized from kraft lignin (KL) and silicon nanoparticles (Si NPs) is shown to have a high starting specific capacity of 2932 mAh/g and a retaining capacity of 1760 mAh/g after 100 cycles at 0.72 A/g as negative electrode in a half-cell lithium-ion battery (LIB) test. It was found the elemental Si and C of the C/Si NPs were most likely linked via Si-O-C rather than direct Si-C bond, a feature that helps to alleviate the mechanical degradation from Si volume change and assure a sound electronic and ionic conductivity for enhanced electrochemical performance. EGA-MS and HC-GC/MS analyses suggest that the interaction of the Si, O and C can be tailored by controlling pyrolysis conditions.

This study systematically investigated the interconnecting aspects among lignin source, pyrolysis chemistry, characteristics of the derived carbon materials and electrochemical performance. Such knowledge on the processing-structure-function relationships serves as a basis for designing lignin-based carbon materials for electrochemical energy storage applications.

KEYWORDS: Lignin, pyrolysis, energy storage materials, supercapacitor, biorefinery, lithium-ion battery

Wenqi Li

(Name of Student)

12/08/2019

Date

LIGNIN-DERIVED CARBON AND NANOCOMPOSITE MATERIALS FOR ENERGY STORAGE APPLICATIONS

By
Wenqi Li

Jian Shi
Director of Dissertation

Donald Colliver
Director of Graduate Studies

12/08/2019
Date

DEDICATION

I dedicate this dissertation in memory of my maternal grandmother, Shuhua Gao, my father, Xinping Xue and my paternal grandfather, Renzong Xue.

ACKNOWLEDGMENTS

I would like to express the deepest appreciation to my advisor Dr. Jian Shi, not only for his excellent guidance, endless support and help to me and my family, and providing me with open-minded, free atmosphere to do research, but more importantly, giving me confidence. I will never forget the words he encouraged me, which makes me believe I am not worse than anyone else on doing research. Without the confidence, I would never be able to finish my PhD work.

I would also like to thank Dr. Yang-Tse Cheng and Dr. Doo Young Kim for their generous authorizing me to access their lab, immediate guidance and help whenever I need. Also, I would like to thank my committee members, Dr. Sue Nokes and Dr. Michael Montross and Dr. Conners as outside examiner for their valuable and constructive advices that help me to initial research proposal and enrich it with practical details.

I would also like to thank my former and current group members, Dr. Lalitendu Das, Enshi Liu, Nguyen Truc, Siquan Xu, Luke Dodge, Ryan Kalinoski, Joseph Stevens, Makua Vin-Nnajiofor, Can Liu, Dr. Binling Ai and Yuxuan, Zhang, and student from Dr. Yang-Tse Cheng's lab, Dr. Tao Chen, Dr. Yikai Wang, Dr. Jiazhi Hu, Ming Wang, Dingying Dang and student from Dr. Doo Young Kim's lab, Dr. Yan Zhang, Namal Wanninayake, Rosemary Lynn Calabro for their valuable help, assistance and each enjoy moment we spent together.

I would also like to thank all the faculty, staff and graduate students and those undergraduates that once worked in Shi lab. Everyone in this department is so nice to me, which make me never feel lonely, although far away from home.

Finally, I would like to my lovely mom. Although she has no idea what I have been doing in the U.S. no matter how many times I try to explain to her, she just uses her practical actions to support me without any complain.

TABLE OF CONTENTS

LIST OF FIGURES

LIST OF TABLES

CHAPTER 1. INTRODUCTION

1.1 Lignin: nature, origin and chemistry

1.1.1 Molecular structure of lignin

Lignocellulosic biomass consists of three major organic polymers: cellulose, hemicellulose and lignin. Lignin is a heterogeneous polymer, which fills the spaces between cellulose, hemicellulose, and pectin in cell wall and plays a crucial role for the structural support of plant biomass [1]. It is widely accepted that the fundamental units of lignin are biosynthesized from three main phenylalanine-derived monomers, also referred as monolignols, *p*-coumaryl (H), coniferyl (G), and sinapyl (S) alcohols, which are differentiated in the extent of methoxylation on their aromatic rings [2]. The chemical structures of the three major monolignol monomers are shown in **Figure 1.1**. Through combinatorial free radical reactions, these monomers assemble into an intricate racemic macromolecule to form p-hydroxyphenyl (H), guaiacyl (G) and syringyl (S) subunits of lignin [3]. Content and compositions of lignin vary among plant species, usually ranging from 10 to 30%, with much higher lignin content of up to 50% in endocarp tissues [4]. In general, lignin in hardwood (from angiosperms) consists of primarily G and S units, while lignin in softwood (from gymnosperms) is mostly composed of G units. Similar levels of G and S units plus a small amount of H units are usually found in the lignin of grasses [5, 6].

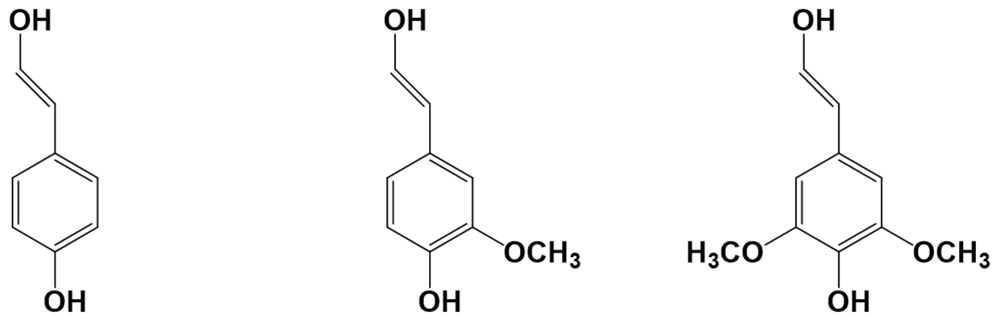

***P*-coumaryl alcohol** **Coniferyl alcohol** **Syringyl alcohol**

Figure 1.1 Three phenylpropanoid units in lignin structure

The monolignols are connected by a heterogeneous networks of inter-unit linkages, as shown in **Figure 1.2**. The most abundant inter-unit linkage involves the β carbon of one benzene ring coupled with the phenolic hydroxyl of the other, referred as β-*O*-4 (β-aryl ether) linkage. Other major linkages include ether bonds, α-*O*-4 (α-aryl ether) and 4-*O*-5 (diaryl ether), as well as C-C bonds, β−β (resinol), β-5 (phenylcoumaran), 5−5 (biphenyl) and β-1 (spirodienone) [7, 8]. The abundance of inter-unit linkages presented in some respective biomass species has been determined by Idaho National Laboratory, as summarized in **Table 1.1**. The heterogeneity in both monolignol composition and inter-unit linkages contributes to the recalcitrant nature of lignin, Such heterogeneity also posed challenges in selective lignin depolymerization while keeping glucan and xylan intact [9]. Seeking an effective biomass fractionation method based on an understanding of lignin composition, structure and cross-linking is essential for co-generating a sugar stream for biofuel production and a lignin stream for valorization [10].

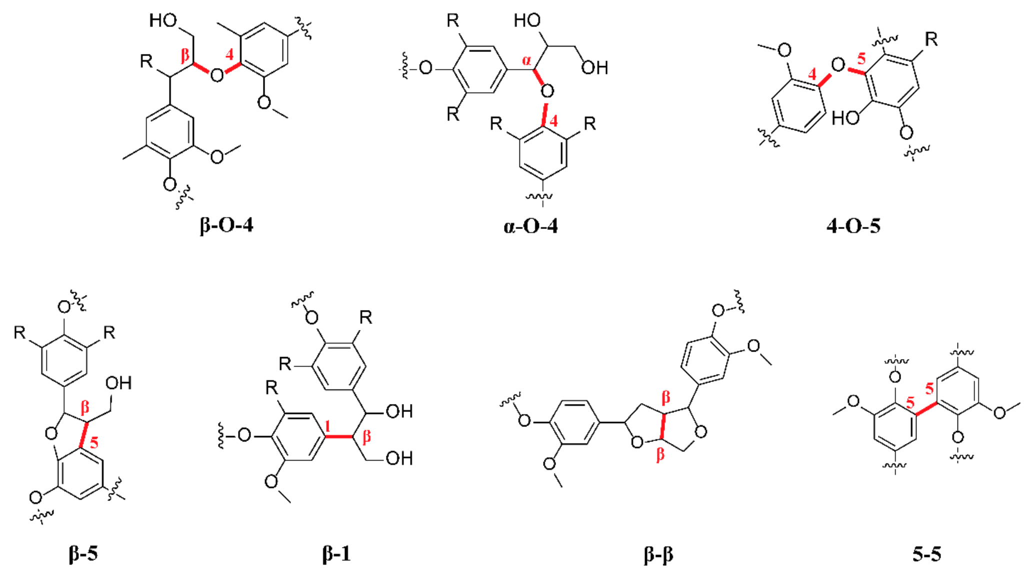

β-O-4 α-O-4 4-O-5

β-5 β-1 β-β 5-5

Figure 1.2 The main inter-unit linkages in lignin structure [11]

Table 1.1 Proportions of types of linkages connecting the phenylpropane units in respective lignin sources [12]

Biomass feedstocks	**β-O-4 (%)**	**β-5 / α-O-4 (%)**	**β-β (%)**	**5-5 /4-O-5 (%)**
Poplar	90	7	3	0
Pine	73	21	4	1
Switchgrass	94	5	1	0
Wheat straw	89	10	1	0

1.1.2 Fractionation of lignin

Pretreatment is an important unit operation in a biorefinery, which is usually followed by enzymatic hydrolysis to convert cellulose into fermentable sugars. During a typical pretreatment, the lignin and hemicellulose sheathing over cellulose were removed, since the presence of lignin blocks the access of cellulolytic enzymes to cellulose [13]. A number of pretreatment techniques have been studied over the years, of which hot water, dilute acid, alkali, and ionic liquid (IL) pretreatment have received the most extensive investigation [14]. Because of the variations in pretreatment chemistry and processing condition, selection of pretreatment technology significantly affects the structural and compositional properties of the extracted lignin. Acid pretreatment methods generally break down hemicellulose to improve accessibility of cellulose to enzymatic hydrolysis. Although little lignin is removed from the pretreated solids, during acid pretreatment lignin is dissolved and reprecipitated onto the solids thus most of the lignin ends in the solid residue after enzymatic hydrolysis [15]. In contrast, alkali-based pretreatments can effectively fragment and dissolve a large portion of lignin and some of hemicellulose. Lignin can be recovered from the alkaline solution by adjusting the pH to acidic [16].

Organosolv pretreatment removes and modifies lignin via a mixture of water and organic solvents, such as methanol, ethanol and acetone, with either acid or base catalysts. The organosolv pretreatment results in significant lignin deconstruction by hydrolyzing the lignin-carbohydrate ester linkages and some inter-unit ether bonds. Condensed S and G units were commonly observed in lignin derived from organosolv pretreatment as compared to dilute acid and ammonia pretreatment [17]. IL is a group of salts with melting points below some arbitrary temperature, such as 100 °C. The near infinite potential combinations of anions and cations to form ILs offer opportunities to fine tune their property and function, therefore ILs are often called “designer solvents” [18, 19]. It was found the fragmentation of lignin macromolecules was related with the anions of ILs and the effect of IL anion on reducing lignin molecular weight is in an order of sulfates > lactate > acetate > chlorides > phosphates [20]. Under neutral or basic conditions, strong nucleophiles such as HS^- or SO_3^{2-} lead to the cleavage of β-*O*-4 to form a new α carbon-carbon double bond; while the weak nucleophiles generate a vinyl ether from the β-*O*-4 linkage instead of cleaving it [20]. Despite of recently development in IL pretreatment, subsequent hydrolysate conditioning, high solvent and processing equipment cost, IL recycling and waste stream treatments hinder industrial relevant application of IL pretreatment technology [21-23].

Recent advances in deep eutectic solvents (DES) provide a new approach for biomass fractionation and lignin extraction. DES is a mixture of Lewis or Brønsted acids and bases acting as either hydrogen-bond donor (HBD) or hydrogen-bond acceptor (HBA) [24]. **Table 1.2** shows the combination of HBDs and HBAs that mixed at 60 °C [25]. DES pretreatment is capable of delivering comparable effectiveness as certain ILs towards dissolving lignin from biomass while the chemical costs much less than many ILs due to low precursor price, simple synthesis and better recyclability [26]. The interactions between HBD and HBA of the DES offer a dual acid/base catalysis system facilitating a controlled cleavage of labile ether linkages among phenylpropane units, and thus lead to lignin depolymerization [27]. By selecting the appropriate HBD and HBA, DES pretreatment can generate a low molecular weight lignin product while maintain most of the properties and activity of native lignin [28].

The efficacy of a pretreatment method largely depends on the selection of biomass feedstock; at the same time, the selection of a pretreatment technology greatly influences biomass decomposition, sugar release, and lignin extraction [29, 30]. There is a gap in linking the diverse chemical complexity of lignin with pretreatment chemistry and the properties of the extracted lignin in respect of how to separate and utilize the lignin stream as a feedstock for making carbon materials for electrochemical energy storage devices. Such knowledge is necessary for rational design of lignin fractionation methods that are adaptable to various biomass feedstocks and downstream thermochemcial conversion for material applications.

Table 1.2 Hydrogen bond donor and hydrogen bond acceptor combinations that create clear DES [25]

Hydrogen bond donor	Molar ratio	Hydrogen bond acceptor
Lactic acid	**9:1**	Alanine
Lactic acid	**2:1**	Betaine
Lactic acid	**1.3:1 to 15:1**	Choline chloride
Lactic acid	**9:1**	Glycine
Lactic acid	**5:1 to 9:1**	Histidine
Lactic acid	**1:1 to 4:1**	Proline
Malic acid	**1:1**	Alanine
Malic acid	**1:1**	Betaine
Malic acid	**1:1.2 to 1.2:1**	Choline chloride
Malic acid	**1:1**	Glycine
Malic acid	**1:1 to 2:1**	Histidine
Malic acid	**9:1**	Nicotinic acid
Malic acid	**1:3 to 3:1**	Proline
Oxalic acid (anhydrous)	**1:1**	Alanine
Oxalic acid (anhydrous)	**1:1.5 to 1.5:1**	Choline chloride
Oxalic acid (anhydrous)	**1:1 to 1.5:1**	Proline
Oxalic acid (dihydrate)	**2:1**	Alanine
Oxalic acid (dihydrate)	**1:1**	Betaine
Oxalic acid (dihydrate)	**1:1**	Choline chloride
Oxalic acid (dihydrate)	**1:1 to 3:1**	Glycine
Oxalic acid (dihydrate)	**1:1**	Histidine
Oxalic acid (dihydrate)	**1:1**	Proline
Oxalic acid (dihydrate)	**9:1**	Nicotinic acid

1.2 Functionalization synthesis processes of lignin-derived advanced materials

Carbon can form many allotropes, such as diamond and graphite, because of its valency. In the last several decades, more allotropes have been discovered such as graphene [31], carbon nanotubes [32] and buckminsterfullerene [33]. With good electric conductivity and tailorable structure and surface (shape, surface area, porosity, and pore size distribution), carbon materials have demonstrated potential in various functional material applications, such as electrochemical energy storage, absorbent, catalyst, soil amendment, etc. [34] Recently, biomass as a carbonaceous precursor has received increasing interests for its sustainability, abundance, and low cost compared with other alternatives, such as coal and petroleum [35]. Thermochemical conversion technologies, including pyrolysis and hydrothermal process, are the most important technologies to convert biomass into different functional materials [36].

The growing demands in the field of catalysts, energy storage and soil amendments have attracted increasing interests in the synthesis of low-cost carbon materials from biomass with designed functions [34]. Thermochemical processes, including pyrolysis and hydrothermal carbonization, have been widely applied to generate carbon material from biomass. The reaction mechanisms of the thermochemical processes are very complex, which depend on the properties of lignin and the reaction conditions, such as temperature and heating rate [37]. The original biochar derived from thermochemical processes has limited functional groups and pore structure. Multiple synthesis approaches were developed to functionalize biochar with specific purposes.

1.2.1 Pyrolysis carbonization

Pyrolysis is a process for thermal decomposition of materials at elevated temperatures in an inert atmosphere, which has been intensively studied in recent years [38]. Based on the heating rates, pyrolysis can be categorized into fast pyrolysis and slow pyrolysis. Fast pyrolysis, carried out at temperatures (around 500 °C) and short reaction times (1 to 5 seconds), has been considered as an effective method for bio-oil production from biomass (normally around 60 to 70 wt%) in addition to biochar (20%) and gas (15%). However, slow pyrolysis, at low to moderate temperatures (around 300 °C) and long reaction times (up to days), converts biomass to high yield of biochar at the expense of bio-oil and gaseous products.

The behavior of lignin in the pyrolysis process is affected by several factors, including the lignin origin (i.e., softwood, hardwood and grass lignin), lignin extraction/pretreatment method, pyrolysis heating rate and reaction temperature [39], and selection of catalyst [40]. The main products acquired from the lignin pyrolysis includes gaseous compounds (e.g., H_2, CH_4, CO, and CO_2), phenolic volatiles and other polysubstituted phenols. Besides the abovementioned liquid and gaseous compounds, depending on pyrolytic temperature and heating rate, a fraction of lignin is converted to a thermally stable solid product, usually referred to as biochar. With plenty of surface functional groups (e.g., C-O, C=O and OH), this carbon material can be applied to functional materials when subjected to various functionalization processes.

Pyrolysis of cellulose and hemicelluloses generates a range of volatile products, primarily short chain carboxylic acids, ketones and aldehydes, such as furan, formic acid, 5-hydroxymethyl furfural and levoglucosenone, etc. [41] Compared to cellulose and hemicellulose pyrolysis, the reaction mechanism of lignin pyrolysis is more complex due to the heterogeneity in lignin composition and possible multiple reaction phases involving prime and secondary reactions [34, 38]. During pyrolysis, the deploymerization of lignin starts with the cleavage of the relative weak ether bonds, such as β-*O*-4 linkages at low temperature and produce primarily guaiacol and syringol type monomers along with a variety of other products [42, 43]. It is believed that the prime reaction of lignin pyrolysis related with the cleavage of β-*O*-4 linkages to generate vinylphenols. The primary products undergo a series of secondary reactions to produce a variety of H, G and S type monomers. Lignin pyrolysis involves free radical reactions and the monomer products are presented as free radicals [37, 38]. Since free radical reaction are chain reactions, it would not terminate as long as the free radicals are present. Hence, the originally volatilized H, G and S type would subsequently go through repolymerization and condensation into oligomers and finally form solid fractions, namely char and coke. A portion of the monomers capture hydrogen radicals entering into liquid fraction [37, 38]; while other portion of the monomers further decompose into gases, such as CH_4, CO, CO_2 and H_2 [43]. As the reactions continue, the free radicals chain reaction within char and coke was forced to terminate after devolatilization and depletion of hydrogen, leaving some free radicals to serve as active sites for the activation to activated carbon [44].

1.2.2 Hydrothermal carbonization (HTC)

Hydrothermal carbonization is a wet biomass thermochemical conversion technology, which mimics the natural process of coal formation but in a short period of just minutes to hours. Being placed in a closed reactor, such as an autoclave, the biomass or biomass-based precursors are surrounded by water and treated at approximately 130-

280 °C under self-generated steam pressure. The final products include solid residue, referred to as hydrothermal biochar, soluble organic compounds and gaseous products, mainly composed of CO_2. Compared to pyrolysis carbonization, HTC generates more biochar while less gases [45]. In addition, with higher H/C and O/C ratios, the chemical structure of hydrothermal biochar is more analogous to natural coal rather than pyrolytic biochar [46]. The primary advantage of HTC over pyrolysis is that it can directly deal with the high-moisture biomass feedstock without energy-intensive preprocessing/drying [47]. However, the high pressure of HTC reaction requires special reactor and process design, leading to high capital investments. Under high pressure, feeding solid biomass into reactors becomes an engineering challenge, which hinders the scaling up of HTC process [47].

Although it is believed that HTC process is generally governed by dehydration and decarboxylation, the complex reaction networks are not fully understood yet. So far, only a series of separate reaction mechanisms are proposed and identified, which include hydrolysis, dehydration, decarboxylation, polymerization and aromatization [48]. Hydrolytic reactions start from the cleavage of the ester and ether bonds of the bio-macromolecules within biomass in the presence of water. The wide range products of hydrolytic reactions include saccharides of cellulose and hemicellulose and phenolic fragments of lignin, which are followed by further dehydration into various sugar derivatives (e.g., 5-HMF) [49]. Chemical dehydration significantly lowers the O/C and H/C ratios [50]. HTC causes partial elimination of carboxyl groups [51, 52]. When reaction temperature increases over 150 °C, both carbonyl and carboxyl groups degrade rapidly and generate CO and CO_2 [53]. Depending on the severity of HTC condition, elimination of carbonyl and carboxyl groups during decarboxylation leaves plenty of unsaturated compounds that are very reactive and prone to repolymerization [54]. The rate of carbonization is determined by the degree of aromatic condensation. Aromatization can happen under both non-hydrous and hydrothermal conditions, even from cellulose and hemicellulose derived carbohydrates [55, 56]. Alkaline condition appears to promote the aromatization [57]. It should be noted that all of the separate reactions mentioned above are not consecutive steps but rather a parallel pathway network, and that the relative significance of the reactions within the whole network primarily depends on the type of feedstocks and HTC conditions [48].

1.2.3 Functionalization of biochar

The original biochar derived from thermochemical conversion has insufficient functional groups and limited surface area and porosity, restricting the application of biochar as functional carbon materials. Abundant surface functional groups provide extra pseudo-capacitance, and large surface area and appropriate pore structure facilitate efficient permeation of electrolyte, all preferable features for energy storage applications. Therefore, functionalization of biochar is critical for upgrading of the raw material before it can be used as a functional material. Surface modification and activation, as primary functionalization approaches, are reviewed below.

Surface modifications

Pseudo-capacitance is the electrochemical storage of electricity in an electrochemical capacitor, is accompanied by the charge transfer between electrolyte and electrode. Pseudo-capacitance of carbon materials obtained from lignin-derived carbon materials is due to the presence of functional groups, such as OH, NH_2, COOH, and SO_3H [34]. The most widely applied heteroatoms or surface functionalities, including oxygen, nitrogen and metal oxide, are discussed as follows.

The presence of oxygen-containing functional group on carbons is unavoidable, since the empty valencies remaining from high temperature treatment are highly reactive. The basic oxygen functional groups, such as carbonyl, carboxyl, can be formed when the biochar is exposed to atmospheric environment [58, 59]. On the other hand, the activation process usually contributes to the addition of acidic oxygen functionalities to the carbon surface [59]. Self-discharge is a phenomenon in energy storage devices in which internal chemical reactions reduce the stored charge of the devices without any connection between the electrodes. Self-discharge is believed to be affected by the oxygen content of the carbon materials. Carbons with acidic surface functionalities showed high rates of self-discharge [60]. In addition, the presence of oxide functionalities often promotes gas evolvement during charging and discharging.

Ammoxidation is an industrial process that dope elemental N into benzene ring via pyrolysis. The N-enrichment process can be performed by reaction of ammonia or its derivatives, such as urea, ammonium carbonate, hydrazine and hydroxylamine [61-63]. Addition of nitrogen containing functional groups greatly improves the specific capacitance of electrode material even though surface area decreases after ammoxidation. The effect of nitrogen highly depends on its location in the graphene network. The electron-donor effect of pyridine group, N-6, is not observed, while quaternary group, N-Q, exhibits enhanced electron-donor effect. The pyrrolic group, N-5, forms if a proton is donated to the nitrogen system [63]. It has been found that the pyridinic forms N-6 and N-Q increase as the pyrrolic forms N-5 decrease [64]. The nitrogen atoms, initially introduced from various types of precursors (e.g. ammonia or its derivatives, ammonium carbonate, hydrazine, hydroxylamine, urea, etc.), are doped into six-membered ring into pyridinic nitrogen, via thermochemical conversion processes or oxidized with nitric acid [63, 64]. During pyrolysis, starting from 450 °C, pyridinic nitrogen is gradually reformed into quaternary nitrogen. Above 800 °C, pyrrolic nitrogen and pyridones are converted to pyridinic nitrogen, quaternary nitrogen and nitrogen oxide species. Until 1000 °C, pyridinic nitrogen to quaternary nitrogen remained to a constant ratio [62]. It is worth noting, however, that the continuous increase in nitrogen content does not always lead to the increase in capacitance because the addition of nitrogen is usually at the expense of surface area.

Tuning of the porosity and surface area

Surface modification introduces various functional groups, but it has no positive effect on increasing porosity and surface area of the carbon materials. Compared with activated carbon (AC), the original biochar generated from thermochemical conversion of biomass possesses significantly lower surface area and porosity. Therefore, an activation process is necessary before the biochar can be applied as a functional material for applications in electrochemical energy storage. Depending on mechanisms, physical and chemical activation, are the two primary approaches to increase porosity and surface area of the biochar.

For physical activation, the most reactive carbon sites of biochar are selectively eliminated by either CO_2, steam or their mixture. Reaction mechanisms of the CO_2 and steam activation are shown as follows:

$$\mathrm{C + H_2O \rightarrow CO\uparrow + H_2\uparrow}$$

$$\mathrm{C + CO_2 \rightarrow 2CO\uparrow}$$

$$\mathrm{CO + H_2O \rightarrow CO_2\uparrow + H_2\uparrow}$$

The pore structure of the biomass-derived AC is greatly affected by activation operation conditions, including temperature, heating rate and holding time. The ash content (mainly Na_2CO_3 and Na_2SO_4) in the kraft lignin had a significant effect on the micropore volume of lignin-derived AC for the physical activation, especially for CO_2, due to the catalytic reactions promoted by ash [65, 66].

Chemical activation is generally performed by pyrolyzing biochar with chemical activating reagents such as KOH, H_3PO_4, $ZnCl_2$, etc. at enhanced temperature (700-1000 °C) [34]. KOH is one of the most commonly used reagents for generating pore structure in carbon materials, but the activation mechanism is not fully understood. It is believed that the reactions between KOH and carbon begin with solid-solid reactions, which are followed by solid-liquid reactions [67]. The activation process consists of several simultaneous and/or sequential reactions. KOH dehydrates at 400 °C to produce K_2O. Carbon will be oxidized by water to produce CO, CO_2 and H_2. The reactions between K_2O

and CO_2 intermediates finally produce K_2CO_3. The reaction processes can be illustrated as follows [68]:

$$2KOH \rightarrow K_2O + H_2O$$

$$C + H_2O \rightarrow CO\uparrow + H_2\uparrow$$

$$CO + H_2O \rightarrow CO_2\uparrow + H_2\uparrow$$

$$CO_2 + K_2O \rightarrow K_2CO_3$$

As catalysts, H_3PO_4 and $ZnCl_2$ promote formation of pore structure via pyrolysis [34]. Montane et al. investigated the mechanisms of H_3PO_4 catalyzed activation during lignin pyrolysis using Thermogravimetric (TG) and differential Thermogravimetric (DTG) analyses. The reactions start from dehydration of phosphoric acid to produce vapor and P_2O_5, lignin pyrolysis to produce carbon and volatiles, following by partial volatilization of the carbon (to CO and CO_2) to produce activated carbon with well-developed pore structure and large surface area [69]. $ZnCl_2$ is also widely applied in activation of lignin. Because of the high boiling point (732 °C), throughout the pyrolysis process, $ZnCl_2$ remains in a liquid phase (melting point: 290 °C). Melting $ZnCl_2$ swells lignin at low temperature while facilitating depolymerization of lignin- at high temperature, which contribute to an even and well-developed pore network [70].

In addition to physical and chemical activation, the templating method is also widely used to create porosity in biochar. In a typical templating process, a template agent such as Pluronic F127 [71] or colloidal silica [72] is first infiltrated into the lignin precursor. The mixture is then subjected to pyrolysis to obtain the templated char. After the template agent is removed, the templated char is then subjected to either physical or chemical activation to enlarge pore volume and create connection between pores. Finally, activated carbons with tailored ratios of micro-, meso- and macropores are acquired. The advantage of templated activation is the tunable pore structure. However, template agents are usually expensive and cannot be easily recycled, and highly toxic and corrosive acid, such HF or H_2SO_4 is needed to remove the template agents. Both drawbacks impede commercialization of the templated activation technology.

1.3 Electrochemical energy storage application

1.3.1 Supercapacitor

A supercapacitor is a high-power energy storage device widely used in transportation vehicles, power grids and consumer electronics [73]. Compared to batteries, such as lithium-ion batteries (LIBs), supercapacitors are favored because of their high-power density and long lifespan, which are suitable for short-term energy storage and burst power delivery. As shown in **Figure 1.3**, a typical supercapacitor is made up of two conductive electrodes with high surface area, separated by an electron-insulating but ion permeable membrane and fully soaked in electrolyte. As the ions of electrolyte spontaneously transfer toward/apart the surface of electrodes with electrons moving between the two electrodes but no charge transfer occurring across the electrode and electrolyte interface during charging and discharging, the capacitance acquired is called electric double-layer (EDL) capacitance. The EDL capacitance is simply achieved by physical adsorption of ions without chemical reactions involved on the interface between electrolyte and electrodes during charging and discharging. Although EDL is mainly attributed to the primary capacitance originated from the electrode made of carbon materials, many carbon materials contain functionalities or have modification on their surface, which contribute to extra capacitance obtained via redox reactions between the electrolyte and electrode, referred as electrochemical pseudocapacitance [74].

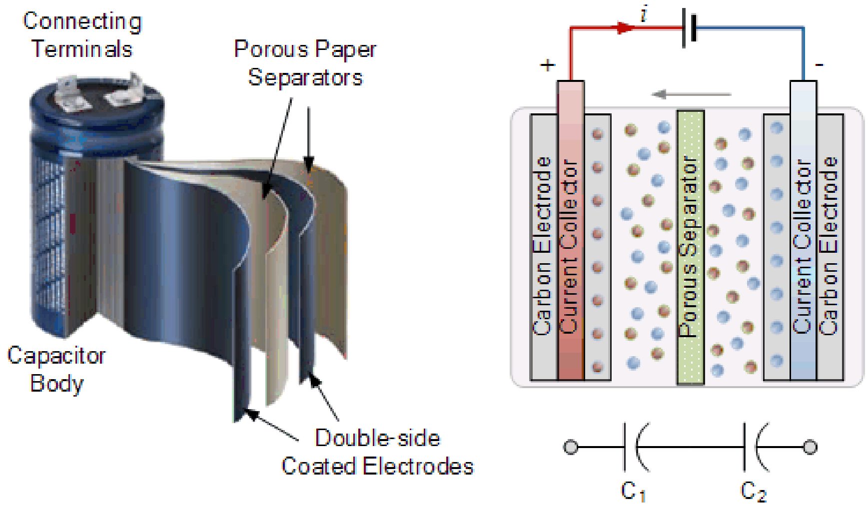

Figure 1.3 Configuration and working principle of an EDL supercapacitor [75]

Based on the principles of EDL capacitance, porous materials, especially activated carbon, have received the most attention as electrode material of supercapacitor not only due to their impressive surface area and electric conductivity but also their tailorable pore structure (shape, pore size distribution) [76]. Lignin has been considered as a favorable precursor for porous carbon materials owing to its high carbon content, highly branched and cross-linked structure, and low feedstock cost [44]. Additionally, plenty of oxygen-containing functional groups formed on the surface of prepared carbon materials offer extra pseudocapacitance to the total capacitance [71]. Therefore, lignin-derived carbon materials have received extensive investigation for the potential application as supercapacitor's electrode in the last decade, with some literature summarized in **Table 1.3**. To obtain higher specific surface area and conductivity and tailored surface functionality for overall performance, various synthesis strategies have been examined in the lignin-derived carbon materials for supercapacitor application. Reviewed here are lignin-derived activate carbon and carbon fibers, surface modification of the lignin-derived carbon materials and lignin-derived carbonaceous composite materials.

Table 1.3 Summary of lignin-derived carbon materials for supercapacitor application

Lignin source	Target materials	Carbonization	Activation	Modification	SSA (m^2/g)	Capacitance (F/g)	Electrolyte	Ref.
Hardwood lignin	AC	Pyrolysis	KOH (700 °C, 2h)	N/A	907	165@ 50 mV/s	1 M H_2SO_4	[77]
Poplar extracted lignin; Pine extracted lignin	AC	Pyrolysis (700 °C, 1h)	KOH (700 °C, 1h)	N/A	621.25; 314.95	86.7, 48.3 @ 0.5 A/g	1 M H_2SO_4	[44]
Alkaline lignin	AC	N/A	$ZnCl_2$ (700 °C, 1h) KOH (700 °C, 1h) K_2CO_3 (700 °C, 1h)	N/A	866, 1191, 1585	142.09, 251.04, 263.46 @ 50 mA/g	6 M KOH	[78]
Corn stover lignin	AC	Hydrothermal (180 °C, 18h)	KOH (800 °C, 3h)	N/A	1660	420 @ 0.1 A/g	6 M KOH	[79]
Black liquor lignin	AC	Pyrolysis (900 °C, 2h)	KOH (900 °C, 2h)	N/A	1406	87 @ 5 mV/s	1.5 M NEt_4BF_4/ACN	[80]
Alkali lignin	AC	Pyrolysis (500 °C, 1h)	KOH (800 °C, 1h)	N/A	3775	286.7 @ 0.2 A/g	6 M KOH	[81]
Kraft lignin, ethanol extracted lignin, alkali extracted lignin	AC	Pyrolysis (950 °C, 6h)	N/A	N/A	1092, 519, 126	91, 35, 53 @ 0.5 A/g	1 M H_2SO_4	[82]
Softwood Kraft lignin	AC	N/A	KOH (800 °C, 1h)	N/A	1800	200 @ 10 A/g	EMIBF4	[83]
Kraft lignin	AC	Pluronic F127 Pyrolysis (1000 °C, 15 min)	CO_2 (875 °C, 35 min) KOH (1000 °C, 35 min)	N/A	624 1148	102.3, 91.7 @ 2 mV/s	6 M KOH	[71]
Acid washed lignin	AC	Pyrolysis (900 °C, 15 min)	Pluronic P123, $EO_{20}PO_{70}EO_{20}$	N/A	803	97.1 F/cm^{-3}@ 289 mA/cm^{-2}	6 M KOH	[84]
Alcell lignin	AC	Pyrolysis (900 °C, 2h)	Zeolites Y template	N/A	1085	250 @ 50 mA/g	1 M H_2SO_4	[85]
Alcell lignin	AC	Pyrolysis (900 °C, 2h)	Zeolites β template	N/A	930	140 @ 1 A/g	1 M H_2SO_4	[86]
Alkali lignin, low sulfur	ECNF mats	Pyrolysis (600 °C, 1h)	KOH (900 °C, 2h)	N/A	2005	205 @ 0.3 A/g	0.5 M Na_2SO_4	[87]
Alkali lignin	ECNF mats	Pyrolysis (1200, 1h)	N/A	N/A	583	64 @ 0.4 A/g	6 M KOH	[88]
Alkali lignin	ACF	N/A	KOH (850 °C, 0.5h)	N/A	N/A	344 @ 10 mV/s	6 M KOH	[89]
Alkali lignin	ECNF mats	Pyrolysis (900, 2h)	CO_2 (850 °C, 3h)	N-doped	1113	410 @ 1 A/g	6 M KOH	[90]
Poplar lignin	AC	Hydrothermal (200 °C, 24h)	KOH (800 °C, 1h)	N-doped	2218	312 @ 1 A/g	6 M KOH	[91]
Sodium lignosulfonate	AC	Pyrolysis (900 °C, 3h)	TEOS template	S-doped	1054	328 @ 0.2 A/g	6 M KOH	[92]
Kraft lignin	MnO_2/ECNF mats	Pyrolysis (1400 °C, 0.5h)	N/A	N/A	N/A	171.6 @ 5 mV/s	1 M Na_2SO_4	[93]
Acetic acid lignin	Iron oxide/HCNF	Pyrolysis (900 °C, 1h)	N/A	N/A	281	121 @ 0.5 A/g	1 M Na_2SO_3	[94]
Sodium lignosulfonate	NiO/AC	Pyrolysis (600 °C, 2h)	Pluronic F127	N/A	802	880.2 @ 1 A/g	6 M KOH	[95]
Alkali lignin	Graphene/C	Hydrothermal (240 °C, 16h)	N/A	N/A	1804	190 @ 0.5 A/g	6 M KOH	[96]
Sodium lignosulfonate	SWCNT/C	Hydrothermal (180 °C, 12h)	N/A	N/A	150.5	292 @ 0.5 A/g	1 M Li_2SO_4	[97]

Lignin derived activated carbons

Activated carbon (AC) has been widely applied as electrode materials of supercapacitor due to its high specific surface area favored by the EDL capacitance. Through flexibly combining various strategies and parameters of carbonization and subsequent activation process, lignin can be converted to structure tailorable carbon materials and consistently emerging highly porous carbonaceous structures have been examined as supercapacitor purpose. Aiming to investigate the effect of activation agent on the lignin-derived porous carbon materials, Wu et al. synthesized different structured activated carbons from alkaline lignin-by a one-step activation process using $ZnCl_2$, KOH and K_2CO_3. Although the different chemical agent displayed little effect on the formation of functional groups at the surface of prepared carbon materials, it demonstrated a critical impact on the specific surface area (SSA). The SSAs of the ACs activated by $ZnCl_2$, KOH and K_2CO_3 were 866, 1191 and 1585 m^2/g, which lead to 142.09, 251.04 and 263.46 F/g, respectively, at a current density of 40 mA/g [78].

With black liquor as carbon precursor and KOH as activation agent, Zhang et al. systematically examined the effect of operation conditions, including KOH/lignin ratio (1:1 to 1:5), carbonization temperature (500 and 800 °C) and activation temperature (700, 800 and 900 °C) on electronical performance of supercapacitors. High carbonization temperature does not favor ideal specific capacitance. When carbonization temperature increased from 500 to 800 °C, the specific capacitance was reduced from 253.5 to 203.3 F/g. The KOH/lignin ratio had significant effect on formation of meso- and micropores, which lead to an impressive SSA of 3775 m^2/g at activation temperature of 800 °C. When activation temperature increased from 800 to 900 °C, the SSA and pore volume significantly decreased as a possible result of over-etched pore structure. Consequently, the electrode carbonized at 500 °C and activated at 800 °C with KOH/lignin ratio of 4:1 exhibited highest specific capacitance of 286.7 F/g at a current density of 0.2 A/g and retained 207.1 F/g at a high current density of 8 A/g [81].

In addition to the processing conditions, the effect of heterogeneity in structure and composition of lignin precursors on the structure of porous carbon material and supercapacitance performances were also investigated. Compared to pine (softwood) lignin-derived AC, poplar (hardwood) lignin-derived AC exhibited a higher level of specific surface area and volume of both mesopores and micropores because of the variations in structure and composition of lignin between softwood and hardwood. As a result, the poplar lignin-derived AC had a higher value of specific capacitance at each current scan rate than the softwood lignin-derived AC [44].

According to International Union of Pure and Applied Chemistry (IUPAC), pores can be classified into macropores, mesopores and micropores [76]. A macroporous material is a material containing pores with diameters larger than 50 nm. Mesoporous materials contain pores with diameters between 2 nm and 50 nm while microporous materials have pores with diameters smaller than 2 nm. It is believed that a bimodal porous structure involving micropores and a narrow distribution of pores between mesopores and micropores is preferred of energy storage purpose [76]. The macropores are beneficial to the fast ion transportation while the mesopores and micropores offer sufficient surface area that bulk ion absorption relies. Therefore, to synthesize organized porous materials with narrow distributions of mesopores and micropores, a lot of templates have been applied

[71, 84-86]. With the assistance of the Pluronic F127 template, Saha et al. synthesized lignin-derived mesoporous carbon material. The volume of mesopores enhanced to 58% and 66% by subsequent physical (CO_2) and chemical (KOH) activation so that obtain SSA of 624 and 1148 m^2/g, respectively. As a result, the synthesized mesoporous carbon materials showed specific capacitance of 102.3 and 91.7 F/g at 2 mV/s for the CO_2- and KOH-activated carbons, respectively [71].

Lignin-derived carbon fibers

In addition to AC, lignin-derived carbon fibers (LCFs) have also received increasing attention for supercapacitor application [98]. A LCFs mat is able to provide a relatively high surface area even without activation process [88]. Additionally, it offers potential to develop flexible electrode materials due to its nature of mechanically flexible [88, 89]. Lai et al. prepared an electrospun carbon nanofiber (ECNF) mat through electrospinning aqueous mixture of alkali lignin and polyvinyl alcohol into fiber mat followed by stabilization and carbonization. As the mass ratio of lignin/PVA was 70/30, the ECNFs mat exhibited a specific surface area of 583 m^2/g without the assistance of activation process. As a result, the ECNFs (70/30) mat delivered 50 F/g at a current density of 2 A/g and the capacitance retained 90% after 6000 cycles. With the assistance of an activation process, the specific surface area of the ECNFs mat was enhanced significantly. Ago et al. produced ECNFs mat from lignin/PVA (75/25) as carbon precursor followed by a separated KOH process and obtained a superior specific surface area of 2005 m^2/g, which led to a high value of specific capacitance of 205 F/g at current density of 0.3 A/g.

Surface modification of lignin-derived carbon materials

Carbon materials have been widely applied to produce EDL capacitor due to their good conductivity and high specific surface area that is available from diverse activation approaches. Doping heteroatoms, such as N, O, S and P, into the carbon matrix is a straightforward approach to incorporate pseudocapacitors into EDL capacitor which improve the overall performance of electrode materials. Yang et al. developed an N-doped electrospun carbon fiber by electrospinning aqueous mixture of lignin and plant protein (hordein/zein, 50/50 wt%). When the ratio of lignin/protein was 80/20, the prepared N-doped electrospun carbon fiber acquired a nitrogen content of 1.33% along with a specific surface area of 1113 m^2/g, both of which resulted in high capacitance of 410 F/g at 1 A/g and retained 95% of the initial capacitance after 3000 cycles at 5 A/g [90]. Tian et al. fabricated a hierarchical S-doped porous carbon material using sodium lignosulfonate as carbon precursor through TEOS template activation. The prepared material exhibited a surface area of 1054 m^2/g and sulfur content of 2.9 wt%. The S-doped carbon material delivered a specific capacitance of 328 F/g at 0.2 A/g [92].

Lignin-derived carbonaceous composite materials

Despite the fact that transition metal oxide nanoparticles offer superior redox-derived electrochemical pseudocapacitance, metal oxides usually have a high electrical resistance, which leads to a low power density for supercapacitor application [99]. A practical strategy is to incorporate transition metal oxide nanoparticles into conductive materials, but the synthesis process requires binder material to integrate all the components. Using a lignin-derived carbon/transition metal oxide composite offers an inexpensive approach to improve electric conductivity of supercapacitor electrode with a binder-free matrix. MnO_2 nanocrystals were successfully deposited on the surfaces of lignin-derived

ECNF mats by hydrothermal degradation of aqueous $KMnO_4$ and the MnO_2/ECNF composite exhibited a capacitance of 171.6 F/g at 5 mV/s [93]. Iron oxide nanoparticles embedded in lignin-derived hollow carbon nanofiber were synthesized by a coaxial electrospinning process, which delivered a specific capacitance of 121.5 F/g at 5 A/g [94]. With the assistance of Pluronic F127, a NiO-containing mesoporous carbon material was synthesized through pyrolysis. When applied as a supercapacitor electrode, the prepared MPC/NiO composite exhibited a superior specific capacitance of 880.2 F/g at a current density of 1 A/g [95].

1.3.2 Lithium-ion batteries

Batteries, such as LIBs are the most widely used energy storage technology for electric transportation and portable consumer electronics [100]. The important criteria to evaluate an electric energy storage material are energy density, power density, efficiency, life span and costs [101]. Energy density is measured in watt-hours per kilogram by determining the amount of energy that a device can store in a given volume, while power density is measured in watts per hour by determining the amount of power that a device can generate in a given volume. LIBs have a higher energy density than supercapacitors, while a supercapacitor has a higher power density than a LIB. This difference makes LIBs capable of storing more energy; while supercapacitors release energy more quickly. Another important characteristic that must be considered when comparing these two devices are the life span during charging/discharging cycles. Supercapacitors exhibit a cycle life that is two orders of magnitude larger than that of lithium batteries under full charging/discharging [100].

Lithium is the lightest metal as well as the most electropositive element LIBs [100]. The configuration of a LIB consists of a cathode (Li^+ host material) and an anode (with Li^+ accessible inter-atomic sites), which are immersed in electrolyte and isolated by a separator, as shown in **Figure 1.4**. The intercalation and deintercalation of lithium-ions causes electrons transfer between cathode and anode during charging and discharging, which fulfill the conversion between chemical energy and electrical energy [74].

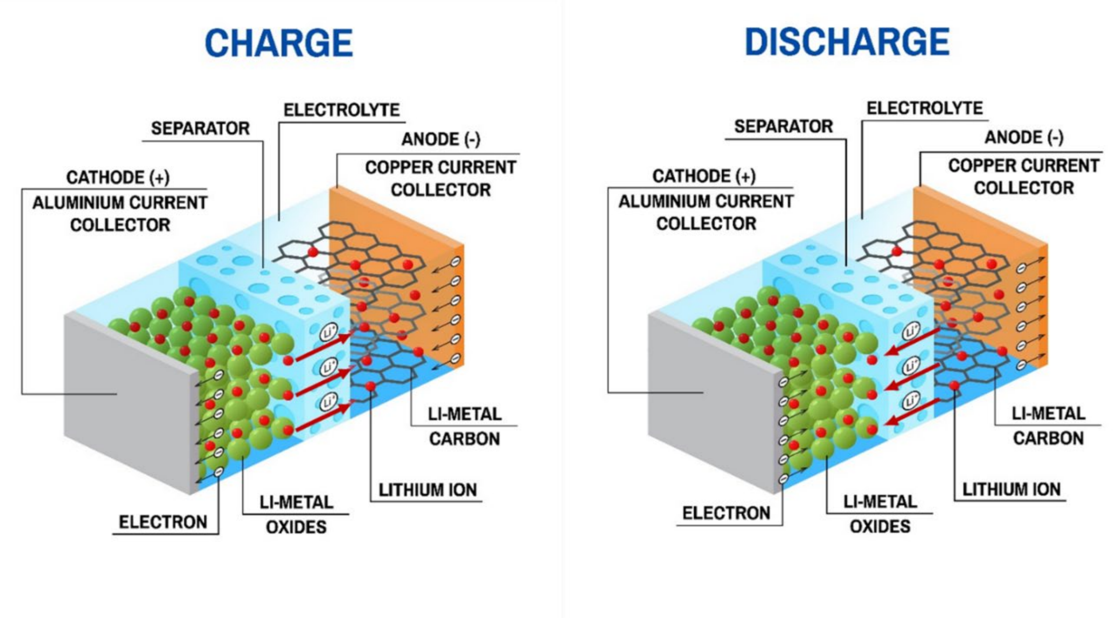

Figure 1.4 Configuration and working principle of LIBs

Lignin-derived non-graphitic carbon LIB anode

Since LIBs s became commercially available in 1991, graphitic carbon materials have become the most widely applied negative electrode material for LIBs. Graphite is a crystal of elemental carbon, which is formed by graphene layers bonded by van der Waals forces [102]. The intercalation of Li^+ between the graphene layers allows good electrical conductivity, mechanical stability and Li-ions dispersion, which makes graphite an attractive anode material with low cost but moderate energy density and good cycling stability [103]. However, for graphite, at the end of Li intercalation, it is thermodynamically favorable to form LiC_6, which makes graphite have a theoretical capacity limitation of 372 mAh/g [104].

Non-graphitic carbons are generally able to be divided into “hard carbon” and “soft carbon” in terms of bonding strength between sp2 layers (graphene) [105]. Hard carbon can be derived from precursors with high oxygen content, such as lignin and cellulose fractions [104]. A strong cross linking of hard carbon crystallites immobilizes the carbon layers and incorporates the crystallites in a rigid mass [106]. Soft carbon is typically synthesized from aromatic hydrocarbons with low oxygen content, such as petroleum and coal. The layers of soft carbon are mobile under weak cross linking, which can be converted to graphite like crystallites under high temperature [104].

With the better understanding of mechanism model for ions intercalation and the development of diverse modification strategies for carbonaceous materials, a variety of non-graphitic carbon materials have been evaluated as anode material for LIB application [107]. Of all synthetic carbon-based materials, hard carbon materials attracted extensive investigation as LIB anode materials. The “house of cards” model can also be used to explain the intercalation mechanisms of hard carbon in LIB and sodium-ion battery (SIB) negative electrode [108]. The small graphitic grains with disordered orientation in hard carbons not only contribute to the insertion of Li-ions between graphene layers but also provide nanopores and defects that offers additional gravimetric capacity, allowing a higher capacity than the theoretical capacity limitation of graphite [109]. Biomass such as cellulose and lignin, can be easily converted to hard carbon materials and the lignin-derived hard carbons have been evaluated as negative electrode materials of lithium-ion materials [110, 111].

The first attempt at lignin-derived hard carbon for LIB anode application can be dated back to 1980s. A series of pyrolytic carbonaceous materials derived from biomass-based precursors, including lignin, were direct mounted with lithium metal and evaluated as anode material of LIB, which offered improved stability and capacity [112]. Afterwards, with the hypothesis that the nanovoids and pore openings of hard carbon contribute to a large capacity for LIB, a variety of hard carbons derived from sugars, endocarps, woods, and lignin under different operation conditions (pyrolysis temperature, heating rate and flow rate of argon) were characterized with XRD, SAXS and BET, and lignin-derived hard carbon exhibited a capacity of 440 mAh/g as anode material for LIBs [113]. In order to acquire lignin-derived hard carbon with higher capacity, various synthetic strategies have been applied to develop nanocarbon materials, including carbon fiber, mesoporous carbon and graphene. Blending with 10% of polyethylene oxide, lignin-derived electrospun carbon fiber mat delivered a capacity of 412 mAh/g at a current density of 30 mA/g [114]. Mesoporous carbon materials offer extraordinary interface between electrode and electrolyte and facilitate ion transfer and diffusion in the anode. A hierarchical mesoporous carbon material generated from lignin demonstrated a capacity of 470 mAh/g after 400 cycles at a current density of 200 mA/g [115]. The theoretical capacity of graphene is as high as 744 mAh/g, which is much higher than that of graphite. A graphene-like carbon / Fe_3O_4 nanocomposite material derived from black liquor was characterized as LIB anode material and exhibited a capacity of 750 mAh/g after 1400 cycles at a current density of

1A/g [116].

Although the theoretical limitation of graphite can be broken through diverse modification or synthetic approaches, the capacity of carbon-based LIBs is still relatively low. Therefore, several other anode materials have been investigated to replace carbon-based materials.

Lignin-derived Carbon/Silicon nanoparticle composite as LIB anode

With a specific capacity of about 3600 mAh/g, silicon has been considered as one of the most promising candidates to replace graphite as active material of next generation LIB anode [117]. However, the capacity and electronic and ionic conductivity of Si composite electrode degrade quickly because of irreversible volume change, delamination, and fracture of the Si, and loss of physical contacts caused by the relentless volume expansion/shrinkage during insertion/extraction of Li ions, [118, 119]. Additionally, development of the solid electrolyte interphase (SEI) on the freshly damaged Si particles surface leads to continuous loss of lithium ions and electrolytes [120], further contributing to capacity fading of LIBs [121]. Therefore, considerable effort has been devoted to improve the electrochemical performance of Si-based LIBs through various approaches [122], including structurally engineered Si (e.g. nanostructured Si [123], 3D porous Si particles [124], coating [125] etc.), flexible current collector [126], pre-lithiation [127], electrolyte additives [128], and improved binder materials [129-131].

Among these approaches, composite material combining nanostructured Si core with a protecting shell has been considered a promising strategy [132, 133]. Taking advantage of this strategy, several lignin-derived carbon/silicon core-shell nanoscale composite have been examined as anode of LIBs [134]. Rios et al. embedded Si nanoparticles on electrospun carbon fibers which derived hard wood lignin from organosolv in a core-shell structure. As a result, the composite retained a specific capacity about 400 mAh/g at a current density of 0.84A/g after 40 cycles [135]. Niu et al. synthesized a self-assembly lignin coated silicon nanoparticles composite under the assistance of phytic acid, which exhibited a 2950 mAh/g at a current density of 0.3A/g after 100 cycles. Most recently, Chen et al. developed a lignin-derived C/Si NPs composite via a one-pot, binder-free thermochemical conversion process, which showed 1390 mAh/g at a current density of 0.54A/g after 100 cycles [136]. Afterwards, by optimizing pyrolysis temperature from 800 to 600 °C while keep other condition the same, the lignin-derived C/Si NPs composite exhibited an enhanced electrochemical performance by retaining 2378 mAh/g after 100 cycles at 1 A/g [133]. The synthesis process represented a comparable electrochemical performance when Si NPs were replaced with SiO_x nanoparticles. After 250 cycles, the lignin-derived C/SiOx composite maintained about 900 mAh/g at 0.2 A/g when tested as a LIB anode [137].

1.4 Conclusion and research motivation

Currently, the commercial potential of lignocellulosic biofuel is hindered by lack of appropriate application for lignin fraction. With extensive research focus in the last few years, great strides have been made in developing lignin valorization strategies. With the rapid development of modern industries and fast-changing electronic technology, the demand for energy storage materials is increasing. Having high carbon content, highly branched and cross-linked structure and low feedstock cost, lignin has been considered as a promising precursor for energy storage materials. However, despite the increasing interest on lignin derived energy storage materials, it is not clear whether the properties of lignin itself, such as the plant origin, fractionation method, structure, and composition, affect the electrochemical characterization of the derived carbon materials for energy storage applications. In addition, despite the wide use of slow pyrolysis to produce carbon materials from lignin, little information is available about the effects of slow pyrolysis conditions on reaction chemistry and correlation between pyrolysis chemistry and properties of the resulting carbon materials.

Therefore, in the present study, we aim to develop a novel lignin fractionation method to extract lignin from various biomass feedstocks. Due to limited information available on fractionating high-lignin content endocarp biomass, DES made of choline chloride and lactic acid would be tested to pretreat two representative endocarps (peach stone and walnut shell) for efficient production of both sugar stream and high-quality lignin stream. Besides, based on fundamental investigation of slow pyrolysis, we will further investigate 1) the effect of lignin sources on the pore structure formation of lignin-derived ACs; 2) the lignin-nanoparticle interactions during thermal processing and characterize the chemical, structural, mechanical and electrochemical proprieties of the derived nanocomposite materials. We will explore applications of the lignin-derived activate carbon and nanocomposite materials for energy storage application such as supercapacitors and for the anode of lithium ion batteries. It is our hope to establish processing-structure-function relationships as the end goal which will provide critical knowledge and guidance on designing lignin-based carbon materials for electrochemical energy storage applications.

1.5 Organization of Chapters

The first chapter serves as a literature review.

The second chapter aims to develop a novel feedstock-agnostic fractionation process based on deep eutectic solvent that is suitable for a variety of biomasses such as switchgrass, poplar (hardwood), pine (softwood) and high lignin content endocarp biomass with respect to quality, and capital and operating cost projections at industrial scale. A suite of analytical tools was used to characterize the lignin stream from DES pretreatment.

The third chapter investigated the effect of pyrolysis temperature and heating rate on the reaction mechanisms and lignin pyrolysis chemistry. This chapter covers determination of the overall product distribution of lignin pyrolysis at different heating rates in different temperature region, as well as systematical characterizations of morphology, pore structure and interfacial chemical property of as prepared solid residues. The pyrolysis is the primary process that is applied to thermochemically convert lignin into diverse carbonaceous energy storage materials. Knowledge obtained in the third chapter provides a fundamental understanding of lignin slow pyrolysis process and serves as a foundation to understand synthesis of lignin derived functional carbon materials in the next two chapters.

The fourth chapter is a study to examine the impact of lignin sources on supercapacitors applications in addition to operation conditions. The lignins were isolated from different biomass categories which vary from structure to composition. The objective of the study is to validate our hypothesis that the non-uniformity in lignin structure, composition and reactivity of diverse lignin sources could contribute to different thermochemical conversion pathway of lignin and lead to different pore structures and size distribution of the derived AC materials and thus influence the electrochemical behavior for supercapacitor applications.

The fifth chapter investigated the formation mechanisms of lignin-derived C/Si NPs composites which can be used as high-performance anode of LIBs. The objectives of this chapter were to determine: 1) the interaction between the Si NPs and C in the composite; 2) the correlation among the structural, chemical, mechanical and electromechanical properties; 3) the connection between the thermochemical conversion conditions and the characteristics of C/Si composite. This study is the first attempt to understand the processing-structure-property relation of lignin derived C/Si NPs composite materials; such relation serves a basis to advancing the development of lignin-derived C/Si NP composite anode material.

CHAPTER 2. FRACTIONATION AND CHARACTERIZATION OF LIGNIN STREAMS FROM UNIQUE HIGH-LIGNIN CONTENT ENDOCARP FEEDSTOCKS

[*] The chapter in whole has been published in *Biotechnology for Biofuels*.

Abstract

Background: Lignin is a promising source of building blocks for upgrading to valuable aromatic chemicals and materials. Endocarp biomass represents a non-edible crop residue in an existing agricultural setting which cannot be used as animal feed nor soil amendment. With significantly higher lignin content and bulk energy density, endocarps have significant advantages to be converted into both biofuel and bioproducts as compared to other biomass resources. Deep eutectic solvent (DES) is highly effective in fractionating lignin from a variety of biomass feedstocks with high yield and purity while at lower cost comparing to certain ionic liquids.

Result: In the present study, the structural and compositional features of peach and walnut endocarp cells were characterized. Compared to typical wood biomass, endocarp biomass exhibits significantly higher bulk density and hardness. The sugar yields of DES (1:2 ChCl:Lac) pretreated peach pit (*Prunus persica*) and walnut shell (*Juglans nigra*) were determined and the impacts of DES pretreatment on the physical and chemical properties of extracted lignin were characterized. Enzymatic saccharification of DES pretreated walnut and peach endocarps gave high glucose yields (over 90%); meanwhile, compared with dilute acid and alkaline pretreatment, the significantly higher lignin removal rates were achieved for DES pretreatment (64.3% and 70.2% for walnut and peach endocarps, respectively) with impressive purities (94.0% and 92.7% for walnut and peach endocarps, respectively). The molecular weights of the extracted lignin from DES pretreated endocarp biomass were significantly reduced. ^{1}H-^{13}C HSQC NMR results demonstrate that the native endocarp lignins were SGH type lignins with dominant G-unit (86.7% and 80.5% for walnut and peach endocarps lignins, respectively). DES pretreatment decreased the S and H-unit while led to an increase in condensed G-units, which may contribute to a higher thermal stability of the isolated lignin.

Conclusion: The high lignin content endocarps have unique cell wall characteristics when compared to the other lignocellulosic biomass feedstocks. DES pretreatment was highly effective in fractionating endocarps to produce both sugar and lignin streams while the DES extracted lignins underwent significant changes in SGH ratio, interunit linkages, and molecular sizes.

Keywords: *Endocarp, Deep eutectic solvent, Pretreatment, Lignin, Biofuel, Biorefinery*

Background

Almost one quarter of the world's population has unmet basic energy needs and the unprecedented green-house gases emission is causing global climate change [138]. These grand challenges have promoted the development of renewable fuels and materials as alternatives to the petroleum based fuels and chemicals [139]. Lignocellulosic biomass is a complex conglomerate of different biopolymers (such as polysaccharides, lignin and protein). From a biorefinery perspective, polysaccharides provide a sugar stream for biofuel fermentation; while the value of lignin has not been fully tapped, the aromatic nature of lignin makes it a potential source of chemicals and materials [140]. Biofuels community are now increasingly interested in fractionating and upgrading lignin to building blocks for high value-added chemicals and materials. Lignin based co-products will greatly enhance the economic viability of a biorefinery [141].

As an existing underutilized feedstock from horticultural fruit crops, endocarp is the hardened inedible portion of the fruit which encases the seed and is discarded. Based on the year 2015 USDA Fruit and Tree Nuts Yearbook, the estimated overall annual yield of endocarp biomass from U.S. processing plants reached nearly 1 million dry tons, which breaks down to almonds: 517.0, walnut: 120.0, peach: 63.6, pistachios: 35.0, olives: 22.7, cherries: 16.5, apricots: 2.2, prunes and plums: 0.13, in thousand dry tons [142]. The hardened drupe endocarp represents the highest lignin content of any biomass source produced in appreciable amounts, up to 50% weight percent [143]. The lignin rich biomass can be a preferable feedstock for biorefinery to produce both biofuel and value-added chemicals and materials. In addition to provide plenty of lignin resources as feedstock, the bulk densities of ground endocarp biomass (i.e., walnut and peach) are 3-4 times higher than the other bioenergy feedstocks such as switchgrass, poplar and pine, as shown in **Figure 2.1**. The bulk and energy density of the feedstock plays a significant role in the overall energy and cost balance of a biorefinery [144]. A biomass feedstock with high bulk and energy density is more efficient to convert into a biofuel than one with a lower bulk and energy density due to the relatively low energy requirements for transportation, storage, and distribution of the feedstock from the field to the biorefinery gate [145]. Furthermore, the endocarp biomass can be readily collected from the well-established fruit and tree nut processing industry, representing a significant advantage in terms of feedstock supply chain stability and logistics.

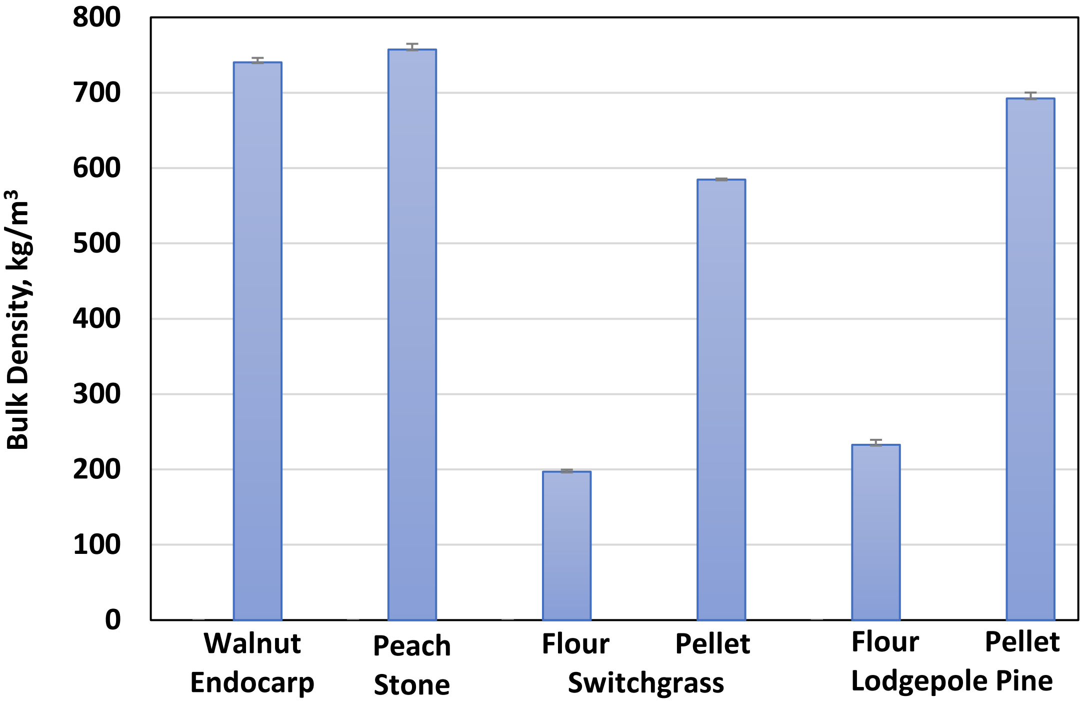

Figure 2.1 Bulk density of endocarp biomass in flour form in comparison with switchgrass and lodge pole pine in flour and pellet forms [144];

To introduce a better use of lignocellulosic biomass to biofuels and lignin-based co-products, it is necessary to find a way to fractionate lignin and cellulose from the feedstock at high efficacy and low cost. Several pretreatment techniques have been studied over the years, with hot water, dilute acid, alkali, and ionic liquid (IL) being the most extensively inverstigated [14]. Hot water pretreatment is effective in releasing hemicellulose sugars and improving cellulose digestibility to glucose by cellulolytic enzymes [146, 147]. Compared with hot water pretreatment, dilute acid pretreatment can process a wider range of biomass types and achieve higher monomeric sugar yields [148, 149]. In contrast, pretreatment can also be effective at higher pH levels by adding reagents such as lime, calcium carbonate, green liquor, potassium hydroxide, and sodium hydroxide, all of which tend to remove a high fraction of the lignin while removing much less hemicellulose than for dilute acids [150]. During an alkali pretreatment, the ester bonds cross-linking between lignin and xylan are typically cleaved, thus increasing the accessibility of cellulose and hemicullose enriched fractions to enzymatic digestion [151-153]. IL is named to reflect the unique property of a group of molten salts with melting points below 100 °C. The near infinite possible combinations of cations and anions to form ILs provide opportunities to fine tune their property and functionality, therefore ILs are often called "designer solvents" [18, 19]. However, the subsequent hydrolysate conditioning to remove inhibitors, the higher cost for reaction vessels and solvents, and the waste stream treatment can add extra cost to the overall process, and thus seriously curb the commercialization of these traditional pretreatment techniques [21-23].

Recent advances in deep eutectic solvents (DES) provided a new way for biomass fractionation and lignin extraction application. DES is a mixture of two or more chemicals acting as either hydrogen-bond donors (HBD) or hydrogen-bond acceptors [24]. DES can be as effective as certain IL towards dissolving lignin from plant materials while costs much less than many ILs due to low precursor price, simple synthesis and better recyclability [26]. The interactions between HBD and HBA of the DES provide a dual acid–base catalysis mechanism which will facilitate controlled cleavage of labile ether linkages among phenylpropane units and thus lead to lignin depolymerization [27]. This chemistry can be tuned by selecting suitable HBD and HBA which will generate a low molecular weight lignin product while maintaining most of the properties and activity of native lignin [28]. A few studies have reported applications of DES for extracting lignin from grass and agricultural residues [154, 155]. Recent studies also investigated deploying this new lignin extraction method to both hardwood and softwood, and characterized the resulting DES extracted lignin product [28, 156]. The resulting lignin product has several distinctive characteristics: high purity, lower and narrowly distributed molecular weight compared to mill wood lignin, and the highly cleaved ether linkages [28].

The efficacy of a pretreatment method largely depends on the selection of biomass feedstock; at the same time, the selection of a pretreatment technology greatly influences biomass decomposition and sugar release [29, 30]. However, very limited information is available on fractionating endocarp biomass, especially using DES. Therefore, to demonstrate the feasibility of DES pretreated endocarp biomass for efficient production of both sugar stream and high-quality lignin, a choline chloride and lactic acid DES solvent was applied to pretreat peach and walnut endocarp biomass. Sugar yields of pretreated solids were recorded and the mass balances for DES pretreatment and enzymatic hydrolysis for both endocarps were determined. Fractionated lignin streams were characterized using thermogravimetric, spectrometric, gel permeation chromatography and NMR analyses.

This study provides insights on how to fractionate and upgrade the underutilized endocarp feedstocks for biofuels and products.

Results and Discussion

Structural and compositional analysis of raw endocarps

Compared to other biomass feedstocks, endocarp biomass exhibits distinctive compositional and physical properties, such as high lignin content, high bulk density, and hardness. It is not clear how these properties correlate to the plant cell wall structure and its recalcitrance; such knowledge will guide the selection of a suitable pretreatment technology. In comparison with well-known biomass feedstock, such as switchgrass and pine, the structural property of walnut and peach endocarp feedstocks was examined using scanning electron microscopy (SEM) and confocal laser scanning microscopy (CLSM). As can be seen from SEM images in **Figure 2.S1**, the switchgrass and pine wood samples retained fibrous nature, while the edges were partially disrupted due to mechanical cutting and grinding. In contract, the walnut and peach endocarps samples showed particulate nature and smaller sample sizes, indicating that the endocarps are brittle. CLSM reveals a three-dimensional cell wall structure of endocarp and biomass samples by capturing multiple two-dimensional images at different depths. Calcofluor white was used to stain cellulose and chitin and is commonly used in plant biology to stain cell walls [157]. **Figure 2.2** compared walnut and peach endocarps to switchgrass and pine wood via CLSM. It is evident that peach and walnut endocarps exhibit a smaller cellular shape and an increase in cellular density when compared to switchgrass and pine wood samples.

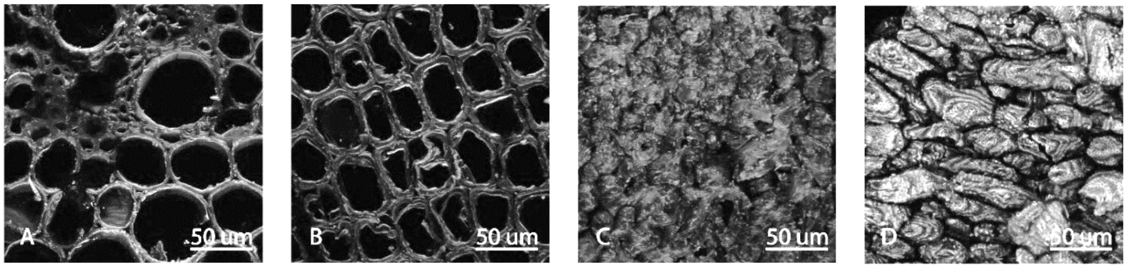

Figure 2.2 Confocal microscopy of Calcoflour White stained raw biomass: A) switchgrass, B) pine, C) walnut endocarp and, D) peach endocarp.

Additionally, light microscopy was employed to determine the location and distribution of lignin within all four biomass types, as shown in **Figure 2.3**. The anatomy of Arabidopsis cross sectional tissue beneath the first leaf is well characterized and multiple metachromatic and monochromatic dyes have been used to determine cross sectional composition [157]. Therefore, the use of well characterized stains when applied to Arabidopsis can easily be used as a reference when staining other tissues, such as endocarps. **Figure 2.3 (A – B)** depicts primary and secondary cell wall staining of Arabidopsis through the use of two dyes 1) Toluidine Blue and 2) Phloroglucinol. Toluidine blue is a metachromatic cationic dye that binds to negatively charged compounds with a primary use in detecting pectin and lignin [158, 159]. Toluidine blue will react with carboxylated polysaccharides and turn pinkish purple, greenish blue or bright blue with poly-aromatic substances, and purplish or greenish blue with nucleic acids [157]. **Figure 2.3-A** shows a blue staining in the metaxylem that is consistent with proper lignin deposition. **Figure 2.3 (C**, **E**, **G**, and **I)** show a similar blue color after Toluidine blue staining, in what we called, metaxylem-like tissue. The relative abundance of metaxylem-like tissues within switch grass and pine (**C**, **E**) seemed comparable to those within peach and walnut biomass (**G** and **I**). To further analyze lignin deposition within tissues, a phloroglucinol stain can be employed [160]. Although it is not a true lignin stain, such that it only stains cinnamaldehyde groups, it is the most common stain for lignin determination. This stain yields a cherry red color in the metaxylem where these groups are present [161]. **Figure 2.3-B** shows a cherry red color in the metaxylem due to the presence of lignin and, therefore, lignin is abundantly present in the endocarp of peach and walnut (**H and J**) when compared to switch grass and pine (**D** and **F**).

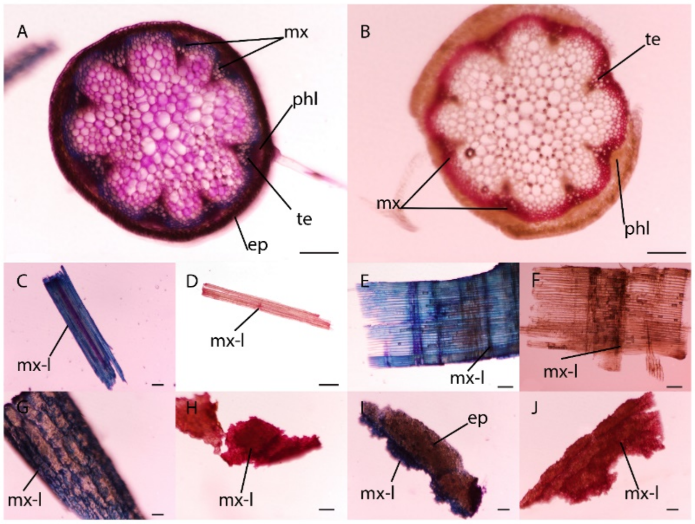

Figure 2.3 Histochemical evaluation of the lignified nature of peach and walnut endocarps.

Evaluation of endocarp used the anatomically characterized Arabidopsis stem section from the lower stem (before first leaf) that have primary and secondary cell walls developed. Abbreviations mx = metaxylem, phl = phloem, te = tracheary elements, ep = epidermis (note that the cortex is not well defined and grouped with the epidermis), mx-l = metaxylem-like staining. A) Toluidine blue staining of transverse cross sections of Arabidopsis stem tissue revealed clear demarcation of the metaxylem in blue, which was also reflected as being highly lignified in the phloroglucinol (B) stained stem cross section due to its cherry red color. The switchgrass and pine shavings stained with toluidine blue (C and E) display a metaxylem-like tissue at a very similar capacity when compared to peach and walnut (G and I). Phloroglucinol staining displays a marked increase in lignin abundance within the peach and walnut endocarps (H and J) when compared to the switchgrass and pine samples (D and F). Scale Bars (100 µM = C, G, I, J / 200 µM = A, B, E, F H / 500 µM = D). Magnification (2x = D / 4x = E, F / 5x = A, B, H / 6.3x = C, G, I, J).

The compositions of walnut and peach endocarps before and after DES pretreatment are shown in **Table 2.1**. Unlike other plant materials, lignin contents were much higher, 45.4% and 45.0 % for walnut and peach endocarp, respectively. The xylan contents for both endocarps were about 15%, comparable to other biomass feedstock, however, the cellulose contents were lower than woody and herbaceous biomass [12, 40]. Only trace amount (<1%) of galactan, mannan, and arabinan were detected in endocarps, indicating that the plants inherit the hardwood characteristics of peach and walnut trees. Glucan and xylan in total accounting about 30-35%, despite low, still represent a substantial portion of the endocarp biomass. It is worth noting that the extractives were low, however, about 10.2 % of walnut and 16.9 % of peach endocarp contents were not accounted as lignin or sugars. Those are likely pectins that glue the endocarp cell wall together.

Table 2.1 Composition of raw endocarps and DES pretreated solids.

	Peach (%)		**Walnut (%)**	
	Raw	DES	Raw	DES
Solid recovery	-	34.2 ± 2.8	-	40.5 ± 3.2
Glucan	17.6 ± 2.0	47.1 ± 0.9	20.9 ± 1.1	47.4 ± 3.7
Xylan	15.3 ± 0.0	4.7 ± 0.2	14.9 ± 0.6	4.2 ± 0.6
Galactan	0.4 ± 0.0	ND	0.9 ± 0.0	ND
Arabinan	0.5 ± 0.0	ND	0.4 ± 0.0	ND
Lignin	45.0 ± 3.6	39.2 ± 1.4	45.4 ± 1.2	40.0 ± 2.7
Extractives	2.8 ± 0.1	ND	7.1 ± 0.2	ND
Ash	1.2 ± 0.3	ND	0.6 ± 0.0	ND

DES pretreatment and enzymatic saccharification

Impact of DES pretreatment on the compositions of pretreated biomass was summarized in **Table 2.1**. Compared with the raw endocarps, the DES pretreated walnut endocarp had higher glucan content (47.4 %) but lower xylan (4.2%) and lignin (40.0%) contents. Similar trend was observed for DES pretreated peach endocarp (47.1% of glucan, 4.7% of xylan and 39.2% of lignin). The purity of DES pretreated lignin can achieve up to 92.1 % and 93.7 % for the extracted walnut and peach lignin, respectively. In addition, the DES pretreatment exhibited a more efficient lignin solubility than the alkaline and dilute acid pretreatment in the present study. As shown in the **Figure 2.4**, lignin removal for DES pretreated walnut and peach endocarp were 64.3% and 70.2%, respectively, which were significantly higher than that of the dilute acid pretreatment (28.5% and 22.2% for walnut and peach endocarp, respectively) and the alkaline pretreatment (50.9% and 48.7% for walnut and peach endocarp, respectively).

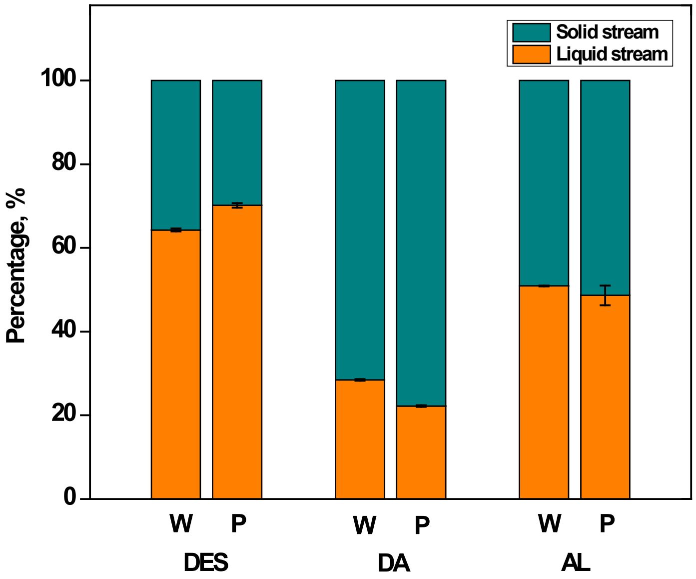

Figure 2.4 Effects of three pretreatment methods using deep eutectic solvent (DES), dilute acid (DA), and alkaline (AL) on lignin fractionation into pretreatment liquid and solid residue streams for peach (P) and walnut (W) endocarps;

Several other pretreatment technologies were also reported to promote sugar release from enzymatic hydrolysis of endocarp biomass. By sequential use of diluted H_2SO_4 and

NaOH pretreatment, 88% of hemicellulose and 64.4% of lignin within buriti (*Mauritia flexuosa*) endocarp were removed, respectively, which lead to a glucose yield of 86% [162]. Steam-explosion pretreated olive stones (200–236 °C for 2–4 min) contributed to an 87.7% glucose yield in first 8 hours of saccharification [163]. It is well known that low pH pretreatment technologies contribute more to the hydrolysis of hemicellulose, while high pH value strategies mainly remove lignin but leave a large portion of hemicellulose in the pretreated solid [164, 165]. Our results suggest that DES pretreatment is highly effective in lignin removal, which agrees with previous reports on choline chloride/lactic acid (ChCl:Lac) based DES pretreatment of poplar and Douglas fir [28], rice straw [155], and willow [156]. Results from this work along with previous studies demonstrate that DES pretreatment was a feedstock agnostic pretreatment method capable of fractionating lignin from a variety of biomass feedstocks, including endocarp biomass, with high lignin recovery and purity.

The effect of DES pretreatment on endocarp biomass was further evaluated by enzymatic saccharification of the pretreated endocarp solids, as shown in the **Figure 2.5**. For untreated endocarps, low sugar yields of 10.5 % and 9.5 % were achieved with saccharification of walnut and peach endocarp, respectively. The DES pretreated endocarps solids showed significantly higher 72-h saccharification sugar yields of 94.8 and 94.5% for walnut and peach endocarps, respectively. Results indicate that DES pretreatment can greatly enhance enzymatic saccharification of both endocarps due to the substantial removal of xylan and lignin as discussed earlier. SEM images of the DES pretreated endocarps and the extracted lignin further illustrated the structural changes (**Figure 2.S2**). As compared to the intact and highly ordered structure of untreated endocarp samples, the pretreated samples exhibited deeply etched surfaces and reduced sample sizes, which can be attributed to the deconstructive impact of DES solvent due to the removal and re-arrangement of lignin in addition to dissolve of xylan. The extracted lignin appeared as amorphous globusses reflecting the dissolution and re-precipitation of lignin during the pretreatment and ethanol-water precipitation and washing process. SEM results provide further evidence that DES pretreatment is effective in enhancing enzymatic hydrolysis by disrupting cell structure and making cellulose more accessible to enzymes.

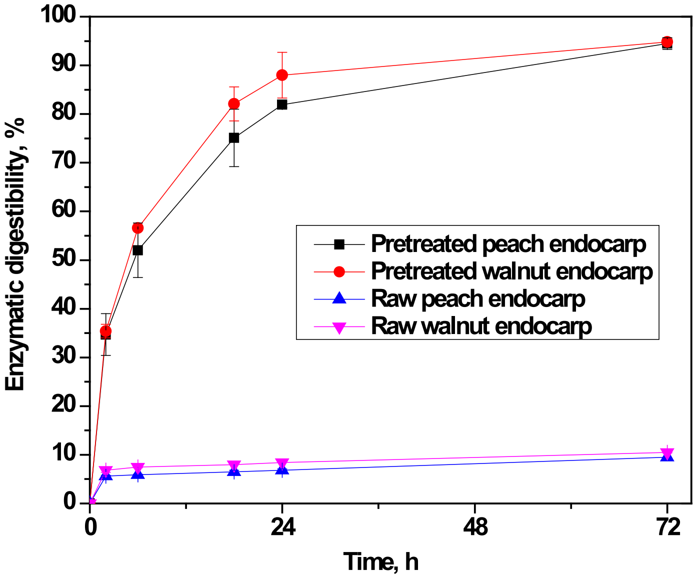

Figure 2.5 Enzymatic hydrolysis profiles of untreated and DES pretreated peach and walnut endocarps.

The mass balances of the major components, glucan, xylan, and lignin for the DES pretreatment and enzymatic hydrolysis of walnut and peach endocarps are shown in the **Figure 2.6**. In general, a similar mass flow and allocation can be observed for both endocarps. Upon DES pretreatment, 40.5 and 34.2 g of pretreated solids were recovered for walnut and peach endocarps, respectively, based on 100 g dry untreated endocarp. The solid streams contain the majority of glucan, a portion of lignin and a slim of xylan. On the same basis, 29.2 g walnut endocarp lignin (64.3 % of total) and 31.6 g peach endocarp lignin (70.2 % of total) with a small amount of glucan and xylan went to the liquid fractions after pretreatment. Furthermore, approximately 19.1 g glucose and 1.8 g xylose from walnut endocarp and 15.8 g glucose and 1.6 g xylose from peach endocarp were recovered from the liquid streams of enzymatic hydrolysis. The overall yield of glucose from liquid stream were 87.5% and 87.5% for walnut and peach endocarps.

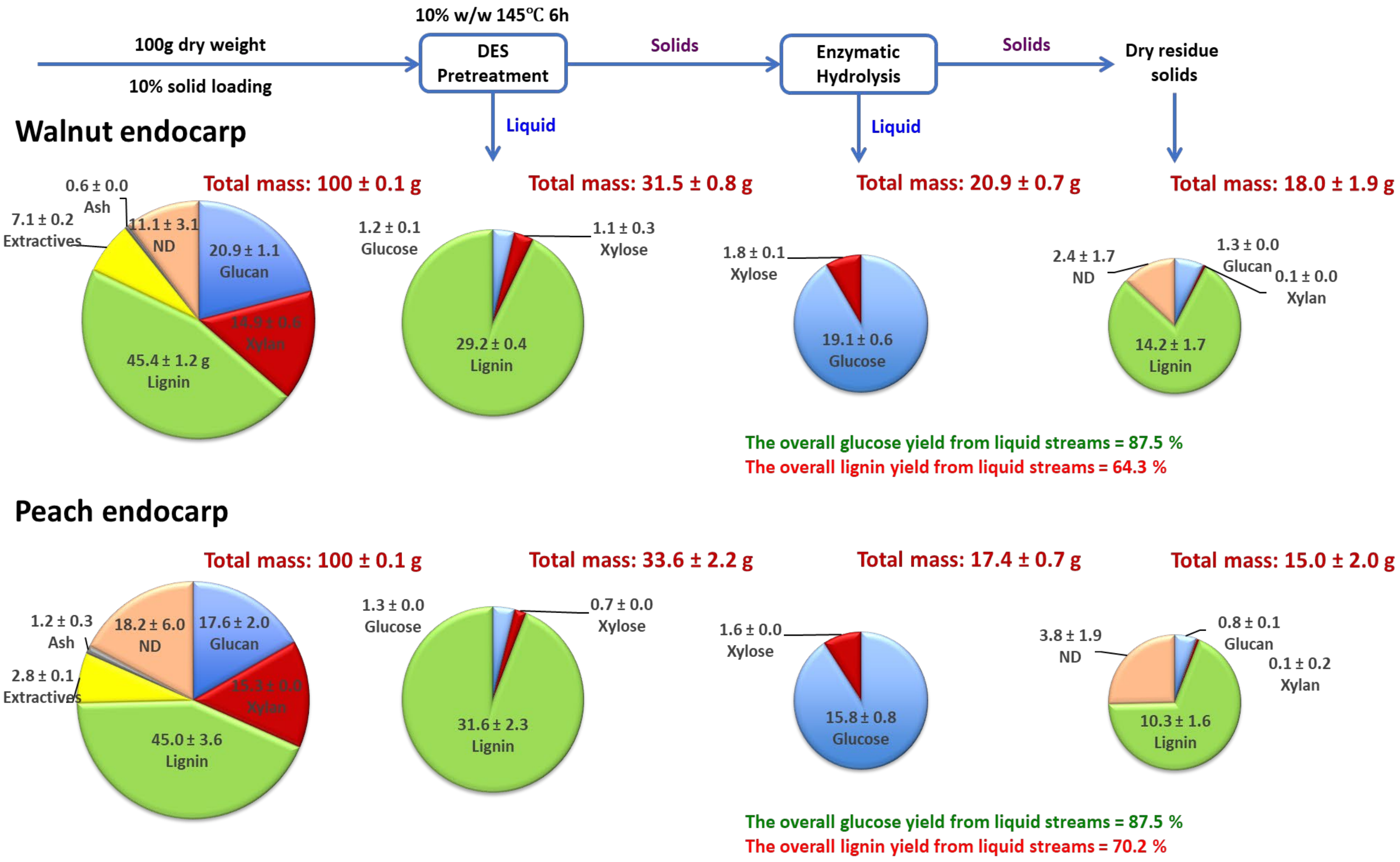

Figure 2.6 Mass flow of lignin, glucan, and xylan during DES pretreatment and enzymatic saccharification of walnut and peach endocarps. ND: not detected.

In comparison with the high overall glucan balance closure, the mass balance for xylan was not well matched up. The overall balance closures of xylan were 17.2 % for walnut endocarp and 13.3 % for peach endocarp, respectively. Low xylose yield has been reported in a previous study using DES pretreatment of corncob [166]. Although it is challenging to compare results between various biomass types, DES solvent systems and operation conditions, we hypothesize that xylan underwent decomposition during DES pretreatment. To verify this hypothesis and better understand the reaction pathway of xylan, pure xylan was employed as a model compound in DES under the same pretreatment condition and quantified the products recovered in the liquid fraction. As shown in the **Table 2.S1**, only a slight portion of xylose (6.9 %), can be detected in the pretreatment liquid. However, a total 37.6 wt% other products were recovered, including furfural, formic acid and levulinic acid; while 25.8 wt% of the starting material remained as solid residue. These preliminary results suggest that xylan was degraded during DES pretreatment, but future work is warranted to better understand the reaction kinetics and the impact of DES solvents on xylan degradation pathways and products.

Thermogravimetric and spectrometric analysis of lignin streams

TGA analysis:

The normalized thermogravimetric (TG) and differential thermogravimetric (DTG) curves of lignin samples, including Kraft lignin (KL), cellulolytic enzyme lignin (CEL), residual lignin in pretreated solid (RL) and DES extracted lignin (DESL) are shown in **Figure 2.7**. Overall, continuous mass loss was observed over a wide temperature range and the first intense mass loss appeared between room temperature to 130 °C, which can be attributed to the evaporation of free and bound water in the lignin samples. The decomposition began around 150 °C and two major DTG phases can be observed from all lignin samples. The first phase appeared between 150 to 300 °C, which can be attributed to the decomposition of low molecular weight lignin polymers and the release of CO, CO_2 and H_2O from cleavage of the side chains of lignin molecules [167]. Following the first phase, the second phase, between 300 and 830 °C, showed the most intense peaks, indicating the release of volatiles from the degradation of large phenolic polymers.

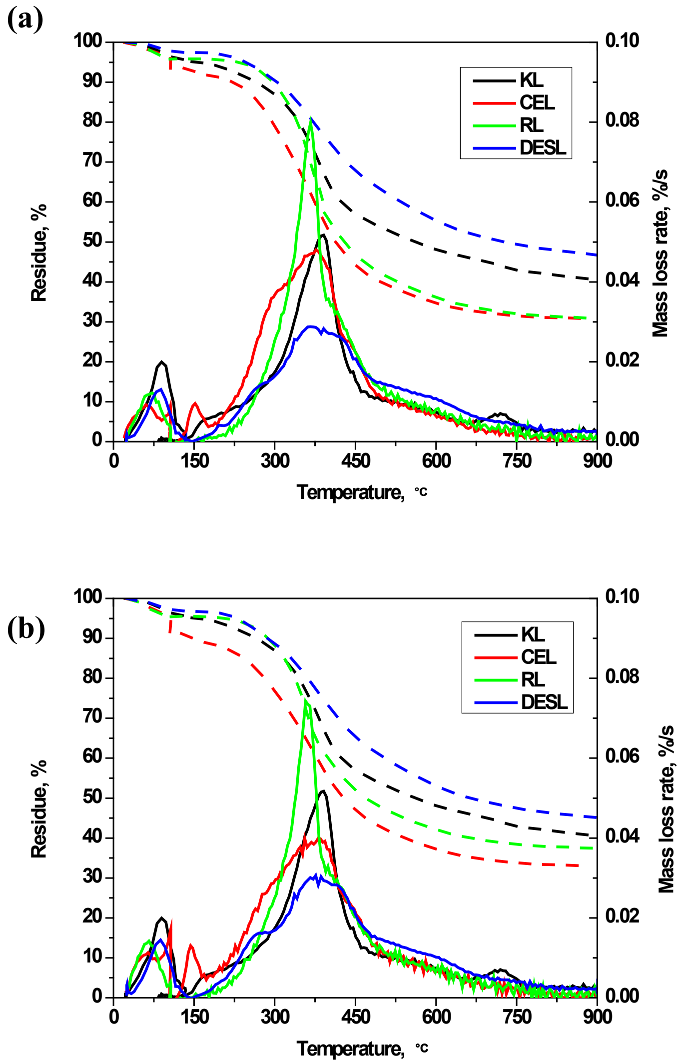

Figure 2.7 TG (solid lines) and DTG (dot lines) curves of Kraft lignin (KL), cellulolytic enzyme lignin (CEL), residue lignin (RL) and DES extracted lignin (DESL) from a) peach and b) walnut endocarps.

Unlike CEL and DESL, RL demonstrated a different decomposition profile. The DTG curve commenced at 150 °C, rapidly rising to a maximal mass loss rate of 0.080 and 0.074 %/s for peach and walnut RL, respectively. A slight mass loss rate shoulder was observed at approximately 400 °C before the peak finally finished at 830 °C. The significantly higher mass loss rate of RL before the shoulder when compared with CEL and DESL may be attributed to the impurities, including glucan, xylan and other un-determined contents; while the peak after the shoulder revealed the decomposition of lignin remained in RL [168, 169]. At the end of thermal degradation, the residual mass fraction followed an increase order of CEL < RL < KL < DESL. The significantly higher residue fraction of DESL than that of CEL and RL may be attributed to the arduousness of lignin decomposition due to the condensation during DES pretreatment, which can also explain why the DESL have a broader but lower DGT peak as compared to CEL and RL.

FTIR analysis:

FTIR spectra of CEL, RL and DESL of peach and walnut endocarps were used to investigate the structural changes and chemical variations of DES pretreatment on endocarp lignins, as shown in **Figure 2.S3**. All lignin samples exhibited a broad absorption band at 3400 cm^{-1}, representing to the O-H stretching vibrations in phenolic and aliphatic O-H groups [170]; The intensity of this band decreased in DESL which can be attributed to the depolymerization and condensation reactions during DES pretreatment. The decreased peaks in DESL between 2920 and 2840 cm^{-1} represents CH_n bonds [171], suggesting the removal of alkane side chains. The bands at 1600, 1500 and 1420 cm^{-1} were attributed to aromatic ring stretch vibrations (C=C) and the C-H deformation bonding with aromatic ring vibration at 1450 cm^{-1} [172]. The increased peaks in DESL at 1220 and 1280 were corresponding to C-C, C-O and C=O stretching [173], which can be attributed to lignin condensation and side chains transfer. The bands at 1140 and 1120 cm^{-1} were associated with guaiacyl (S) and syringyl (G) units of lignin, respectively [173, 174]. The more intense band at ~1700 cm^{-1} in DESL than that of either CEL or RL suggested presence of more unconjugated C=O units. The significantly reduced S unit in DESL than CEL can be found in both peach and walnut endocarp, which were corresponding to the NMR analysis.

Molecular weight distribution analysis of lignin streams

To better understand the lignin depolymerization process during DES pretreatment of endocarps, gel permeation chromatography (GPC) was applied to determine the molecular weight distribution. The weight average molecular weight [175], number average molecular weight (Mn) and polydispersity index (PDI) of the CEL, RL, and DESL are shown in **Table 2.2**. The molecular weights of CEL, representing the intact lignin in native plant, were significantly higher than that of RL and DESL, indicating that DES pretreatment is effective in depolymerizing the native lignin. The extent of size reduction was however less intense as compared to IL pretreated lignin with $[C_2C_1Im][OAc]$ [20, 176]. It is possible that the depolymerized lignin partially repolymerized during DES pretreatment, which has been seen in a previous study on DES extracted sorghum lignin [177]. The PDI values reveal the heterogeneity of the size distribution of the lignin samples. The relative PDI value of RL was significantly higher than that of CEL and DESL for both peach and walnut endocarps. Results suggest that the CEL and DESL were more uniform in molecular weight than RL after DES pretreatment. The increasing in heterogeneity of the RL may be explained by either the simultaneous depolymerization and repolymerization of lignin oligomers during DES pretreatment or the uncompleted deconstruction due to inadequate contact.

Table 2.2 The number-average (Mn) and weight-average [175] molecular weights of Kraft lignin (KL) and cellulolytic enzyme lignin (CEL), residue lignin (RL) and DES extracted lignin (DESL) from peach and walnut endocarps.

	CEL from raw biomass			**Lignin in pretreated solids**			**Precipitated lignin**		
	M_w (g/mol)	**M_n (g/mol)**	**PDI**	**M_w (g/mol)**	**M_n (g/mol)**	**PDI**	**M_w (g/mol)**	**M_n (g/mol)**	**PDI**
Kraft	ND	ND	ND	ND	ND	ND	4952	2600	1.9
Peach	6129	2805	2.2	4780	1490	3.2	4344	2431	1.8
Walnut	7426	3551	2.1	4880	1616	3.0	4200	2460	1.8

NMR characterization of lignin streams

To examine the change in chemical structure of endocarp lignins through DES pretreatment, 2D ^{1}H-^{13}C HSQC NMR was applied to characterize the endocarp CELs and DES extracted lignins. The aromatic region (6.0-8.0/100-150 ppm) of the lignin samples, revealed key lignin monolignol subunits, as shown in the **Figure 2.8a**. 2D NMR spectra of aromatic regions showed that both walnut and peach CELs are SGH type lignin, and dominated by G unit accounting for up to 80 % of all compositional units. The peach lignin had a much higher S unit (15.0%) than the walnut lignin (1.7%) and a lower H units (4.5% vs. 11.6%). The S/G ratios of peach and walnut CEL are 0.19 and 0.02, respectively. After DES pretreatment, a large portion of S and all of H units were removed. In addition, a large amount of condensed G unit was observed after DES pretreatment, which can be explained by its high reactivity toward condensation during pretreatment [172]. The structural changes of lignin subunits in the endocarp lignins, i.e., removal of H and condensation of G units, are consistent with the results observed in the sorghum lignin treated with DES [177].

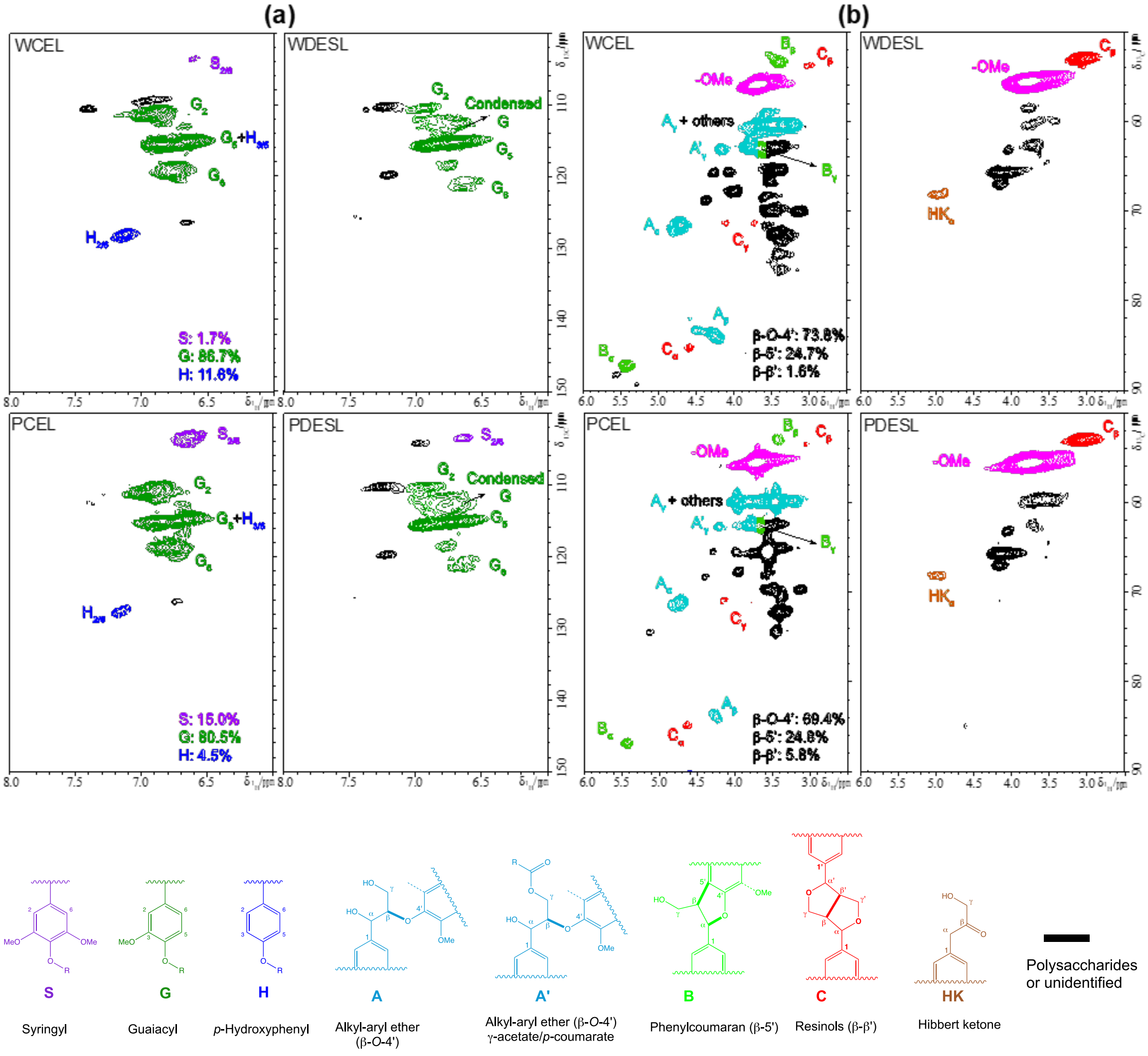

Figure 2.8 13C-1H (HSQC) spectra of aromatic regions (a, top left) and aliphatic region (b, top right) of walnut CEL (WCEL), walnut DES extracted lignin (WDESL), peach CEL (PCEL) and peach DES extracted lignin (PDESL). The structures of lignin compositional units and side-chain linkages were coded with colors corresponding to the cross peaks in the spectra.

The aliphatic region (2.5-6.0/50-90 ppm) of the lignins, revealed the lignin inter-units and side chains, was shown in the **Figure 2.8b**. Both peach and walnut CELs were found to be dominated by β-*O*-4’ and β-5’ units accompanied with a minor amount of β-β’ linkages. After DES pretreatment, β-β’ linkages were significantly increased, at the expense of the removal of β-*O*-4’ and β-5’ linkages. The presence of Hibbert’s ketone (HK) (68.6/4.93 ppm) in DES lignin corroborates the cleavage of β-*O*-4’ linkages by DES. The results of side-chain linkages changes, i.e., substantial decreases of β-*O*-4’ and β-5’, increase of β-β’, and the formation of HK, in endocarp lignins are consistent with the DES treated sorghum lignin [177] and Douglas fir lignin [178]. The NMR spectra revealed that the endocarp lignins of peach and walnut undergo a similar structural change during DES treatment as other lignin species, such as sorghum and Douglas fir.

Conclusions

Walnut and peach endocarps have high lignin content, bulk density, and energy density compared to common biomass feedstocks, attributing to the unique plant cell wall structures. DES pretreatment was shown to be an effective method to fractionate endocarps in order to produce both sugar and lignin streams. More specifically, >90% sugar yields were achieved during enzymatic hydrolysis of DES pretreated peach and walnut endocarps. Lignins were extracted at high yields of 64.3% for walnut and 70.2% for peach endocarps with more than 92% purity. Characterization of the recovered lignin streams demonstrated that DES pretreatment is effective in depolymerizing the native lignin while at the same time keeping thermal stability. The native walnut and peach CELs are SGH type lignin with dominant G units. The DES pretreatment significantly removes the S and H unit while condenses the G unit. Meanwhile, the relative abundance of β-β’ linkages in DES extracted lignin increased; nearly all β-*O*-4’ and a large portion of β-5’ linkages were removed during DES pretreatment.

Methods

Materials

The two endocarp feedstocks: peach pit (*Prunus persica*) and walnut shell (*Juglans nigra*) were collected in 2017 from Center for Crop Diversification at University of Kentucky. The remaining pericarp and mesocarp tissues were manually removed from the endocarps and the recovered endocarps were washed with DI water, and dried at 40 °C in a convection oven. Hybrid poplar (*Populus deltoides x P. nigra*, clone OP-367/433) and lodge pole pine (*Pinus contorta*), were obtained from the Idaho National Laboratory. The raw biomass feedstocks were grounded by a Wiley Mill to pass through a 20 mesh screen. Then the grounded biomass was sieved to acquire a particle size range of 0.25 to 0.425 mm. All chemicals and reagents were of analytical grade and purchased from Sigma-Aldrich (St. Louis, MO, USA) and Fisher Scientific (Waltham, MA, USA). Enzymes, cellulase (Cellic® CTec2) and hemicellulase (Cellic® HTec2) were provided by Novozymes North America (Franklinton, NC, USA).

Compositional analysis

The percentage of biomass composition, including moisture, extractives, ash, glucan, xylan and lignin, was determined with a two-stage acid hydrolysis according to a NREL laboratory analytical procedure [179]. Following the two-stage acid hydrolysis, acid insoluble lignin was determined by the acid insoluble residue excluding the ash content.

The quantity of acid soluble lignin was determined by UV-vis spectrometer at the absorbance of 205 nm. The amount of monomeric sugars, glucose and xylose, were measured by a Dionex Ultimate 3000 HPLC equipped with a refractive index detector and a Biorad Aminex HPX-87H column, using 5mM H_2SO_4 as mobile phase at a flow rate of 0.4 ml/min and a column temperature set of 50 °C. Galactose, mannose, and arabinose contents were low or absent in raw biomass as analyzed by HPLC using Biorad Aminex HPX-87P column using water as mobile phase thus HPX-87H column was used for sugar analysis.

Pretreatment

<u>Deep eutectic solvent (DES) pretreatment and lignin recovery</u>:

The DES in the present study was synthesized from choline chloride and lactic acid with a molar ratio of 1:2. The eutectic mixture was prepared by mixing the two components in a beaker at their solid state, followed by heating the mixture in an oil bath at 60 °C with constant stirring until a homogeneous and transparent DES liquid (ChCl-Lac) was gained. For DES pretreatment, 2 g of endocarp biomass was slurried in an 18 g of DES. The endocarp biomass (10% biomass loading) was pretreated with the ChCl-Lac solvent in an ACE glass pressure vessel reactor at 145 ± 2 °C in an oil bath for 6 hours. The pretreatment was carried out with a constant stirring at 200 rpm. After pretreatment, the slurry was rinsed with 20 ml ethanol and centrifuged at 4000 rpm for 10 min to separate the pretreated solid and liquid fraction. Lignin was precipitated from the liquid fraction by adding water to the liquid until reaching a water: ethanol ratio of 1:9 [178]. Precipitated lignin was washed five times with a 1:9 ethanol/water solvent and the pretreated biomass was washed five time with ethanol to fully remove any remained DES solvent. And then the washed pretreated solids and lignin were freeze-dried for future use.

Dilute acid (DA) pretreatment:

2 g of endocarp biomass was slurried in 18 g of 1% (w/w) sulfuric acid solution in a 20 ml SS316 stainless steel reactor and pretreated at 160 ± 2 °C in an oil bath for 40 min. After pretreatment, the slurry was centrifuged at 4000 rpm for 10 min to separate the solids and liquid. The recovered biomass solids were washed four times with 35 ml of hot DI water to remove any residual sugars and excess sulfuric acid and kept at 4 °C for further analysis.

Alkaline (AL) pretreatment:

2 g of endocarp biomass was slurried in 18 g of 2% (w/w) NaOH and 0.5% H_2O_2 solution in a 20 ml SS316 stainless steel reactor and pretreated at 160 ± 2 °C in an oil bath for 60 min. After pretreatment, the slurry was centrifuged at 4000 rpm for 10 min to separate the solids and liquid. The recovered biomass solids were washed four times with 35 ml of hot DI water to remove any residual sugars and excess alkali and kept at 4 °C for further analysis.

Enzymatic hydrolysis and mass balance

Enzymatic saccharification of untreated and pretreated endocarps were carried out according to the NREL laboratory analytical procedure [180]. The cellulase (Cellic® CTec2, protein content 188 mg/ml) was applied at enzyme loading of 20 mg CTec2 protein/g glucan supplemented with hemicellulase (Cellic® HTec2, protein content 27 mg/ml) loading of 0.26 mg/g glucan. The saccharification was performed at 50 °C, 0.05 M citrate buffer and pH 4.8 in an orbital shaker. After 72 h of hydrolysis, the remaining solids were collected by centrifugation and washed four times with DI water to remove residual sugars, while the supernatant liquid fractions were analyzed by HPLC for the monosaccharides as mentioned in the composition analysis section. Mass balances (Glucan, xylan and lignin) were closed on the liquid and solid streams of fractionated endocarps after DES pretreatment and enzymatic hydrolysis on dry basis of 100 g starting biomass.

Characterization of lignin and untreated and treated endocarps

Confocal laser scanning microscopy (CLSM):

Calcoflour White Stain (Sigma Aldrich, St Louis MO) was prepared by mixing Calcoflour White Stain with 10% Potassium Hydroxide at 1/1 (v/v) and specimens were soaked under the coverslip in solution for 1 minute prior to imaging. Specimens were imaged under an Olympus FV1200 Laser Scanning Microscope at 60x. All images were captured using Fluoview software version 4.2 with the same settings: excitation wavelength of 405 nm, dichroic beam splitter of 405/488/559 nm, and a bright field range of 70 nm starting at 410 nm. Minimal processing was performed aside from fluorescence normalization. The figure was cropped and edited in Adobe Photoshop and Illustrator.

Staining and Imaging for Light Microscopy:

A solution of Toluidine Blue was made by mixing 0.05% (w/v) Toluidine Blue (Sigma Aldrich, St Louis MO) with distilled water and a phloroglucinol stain was prepared fresh using 50% 1M HCL and 50% distilled water with a 5% (w/v) of phloroglucinol. Biomass samples were briefly exposed to these solutions by immersing them between 3-5 minutes. Specimens were imaged under an Olympus stereomicroscope in bright field conditions. Images were captured using cellSens Dimension software (Olympus).

Scanning electron microscopy (SEM):

Images of the raw, pretreated endocarps and DES extracted lignin samples were obtained by a FEI Quanta 250 FEG SEM operating at SE mode under low vacuum (0.40–0.65 Torr). Samples were prepared for imaging by freeze-drying using an AdVantage 2.0 bench top lyophilizer (SP Scientific, Warminster, PA). The dried biomass samples were sputter-coated in gold and the imaging was performed at beam accelerating voltages of 2 kV.

Gel permeation chromatography (GPC) analysis:

The samples were acetylated using acetic acid and acetyl bromide as published protocol for GPC analysis [181]. The weight-average molecular weight [175] and number-average molecular weight (Mn) of the lignin samples were determined by a Dionex Ultimate 3000 HPLC system, which equipped with a Mixed-D PLgel column (5 µm particle size, 300 mm x 7.5 mm i.d., linear molecular weight range of 200 to 400,000 u) and ultraviolet [182] detector at wavelength of 280 nm.

Fourier transform infrared spectroscopy (FTIR):

A Nicolet Nexus 870 FTIR was used to obtain FTIR spectra of the lignin samples. Spectra were obtained using an average of 64 scans between 400 and 4000 cm^{-1} with a spectral resolution of 2 cm^{-1}. The raw FTIR spectra were baseline corrected and normalized using Omnic 6.1a software and compared in the range 700-2000 cm^{-1}.

Thermogravimetric analysis (TGA):

All TG and differential thermogravimetric (DTG) data were acquired using a Thermo Scientific Q500 TGA analyzer. In brief, 10 mg of lignin sample was placed in a crucible, heated in a nitrogen environment from room temperature to 105 °C ramping at 10 °C/min and held for 40 min to determine the moisture content. Then, temperature was increased to 900 °C ramping at 10 °C/min and held for 20 min to measure volatile content.

Cellulolytic enzyme lignin (CEL):

The untreated endocarps were extracted with a mixture of toluene-to-ethanol ratio of 2:1 (v/v) [183, 184]. The extractives-free samples were grinded using a SPEX SamplePrep 8000D ball mill loaded with 10×10 mm balls at 550 RPM in a frequency of 5 min with 5 min pauses in-between for 1.5 h time in total. The milled fine powder was then subjected to enzymatic hydrolysis with a mixture (1:1 by volume) of Cellic® CTec2 and HTec2 at 50 °C, 0.05 M citrate buffer and pH 4.8 in an orbital shaker for 48 h. The residue was isolated by centrifugation and enzymatic hydrolyzed one more time with fresh enzymes. The lignin-enriched residue was extracted with dioxane-water (96% v/v, 10.0 mL/g biomass) for 24 h. After separation of supernatant with residue, dioxane extraction was repeated one more time. The extracts were combined, roto-evaporated to reduce the volume at less than 45 °C and freeze dried. The obtained lignin samples, designated as CEL, was used for further analysis.

Nuclear magnetic resonance (NMR) spectroscopic analysis:

Two-dimensional heteronuclear single-quantum correlation NMR (2D HSQC NMR) spectroscopy of lignins were obtained at 25 °C on a Bruker Avance III HD 500-MHz spectrometer incorporated with a 5 mm N_2 cryogenically cooled BBO H&F probe using Bruker pulse sequence (hsqcetgpspsi2.2). Test samples were prepared by dissolving 20 mg of CEL in 100 mg DMSO-d_6 in a micro-NMR tube, while 40 mg of DES lignin in 0.5 mL DMSO-d_6 in 5 mm NMR tube. The HSQC experiments were performed with the following acquisition parameters: spectra width 12 ppm in F2 (^{1}H) dimension with 1024 data points (acquisition time 85.2 ms), 166 ppm in F1 (^{13}C) dimension with 256 increments (acquisition time 6.1 ms), a 1.0-s delay, a $^1J_{C\text{–}H}$ of 145 Hz, and 128 scans. The central DMSO-d_6 solvent peak (δ_C/δ_H at 39.5/2.49) was used for chemical shifts calibration. Assignment and the relative abundance of lignin compositional subunits and inter-unit linkage were estimated as described in literatures [183, 185]. For volume integration of monolignol compositions of syringyl (S), guaiacyl (G), and *p*-hydroxyphenyl (H), the cross peaks of $S_{2/6}$, G_2, and $H_{2/6}$ contours were used with G_2 integrals doubled. The C_α signals were used for volume integration for inter-unit linkages estimation. The abundances of aromatics and side-chain linkages were presented as percentage of total SGH units.

Declarations

Acknowledgements

This work is supported by the USDA National Institute of Food and Agriculture under project accession no. 1015068 and the National Science Foundation under Cooperative Agreements 1355438. The information reported in this paper is part of a project of the Kentucky Agricultural Experiment Station and is published with the approval of the Director. Oak Ridge National Laboratory is managed by UT-Battelle, LLC under Contract DE-AC05-00OR22725 with the U.S. Department of Energy (DOE). This work was partially supported by the BioEnergy Science Center (BESC) and the Center for Bioenergy Innovation (CBI). The BESC and CBI are U.S. DOE Bioenergy Research Centers supported by the Office of Biological and Environmental Research in the DOE Office of Science. The views and opinions of the authors expressed herein do not necessarily state or reflect those of the United States Government or any agency thereof. Neither the United States Government nor any agency thereof, nor any of their employees, makes any warranty, expressed or implied, or assumes any legal liability or responsibility for the accuracy, completeness, or usefulness of any information, apparatus, product, or process disclosed, or represents that its use would not infringe privately owned rights. We thank Novozymes for providing enzyme samples and the Idaho National Laboratory for providing biomass materials.

Competing interest

The authors declare that they have no competing interests.

Authors' contributions

WL, JS, SD and YC conceived the scope and structure of this study. WL carried out the pretreatment, enzymatic saccharification, partial lignin characterization and drafted the manuscript. KA carried out the confocal imaging and helped in drafting the manuscript and participated in discussion on the results and analysis of this study. ML, YP and AR carried out the NMR analysis and helped in drafting the manuscript.

Electronic Supplemental Information

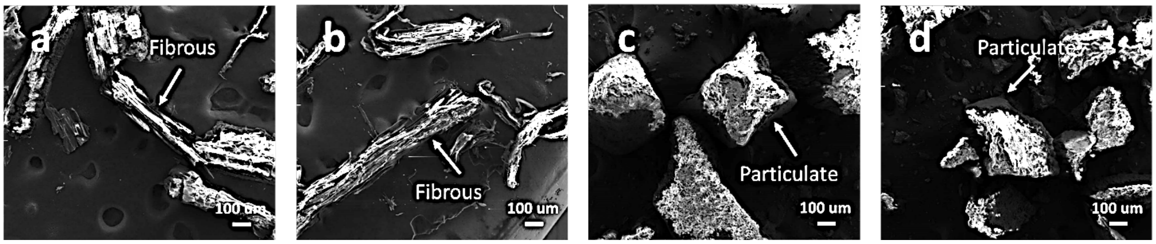

Figure 2.S1 SEM images of raw biomass samples: a) switchgrass, b) pine wood, c) walnut endocarp, d) peach endocarp.

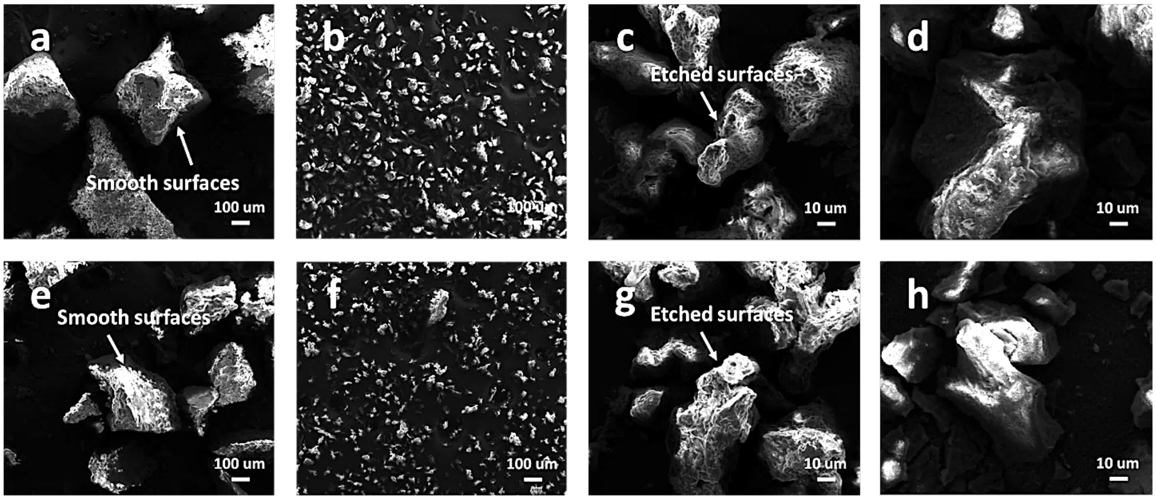

Figure 2.S2 SEM images of unpretreated, DES pretreated and extracted lignin of walnut and peach endocarp: a) unpretreated walnut endocarp, b) and c) DES pretreated walnut solid, d) extracted walnut lignin, e) unpretreated peach endocarp, f) and g) DES pretreated peach solid, h) extracted peach lignin.

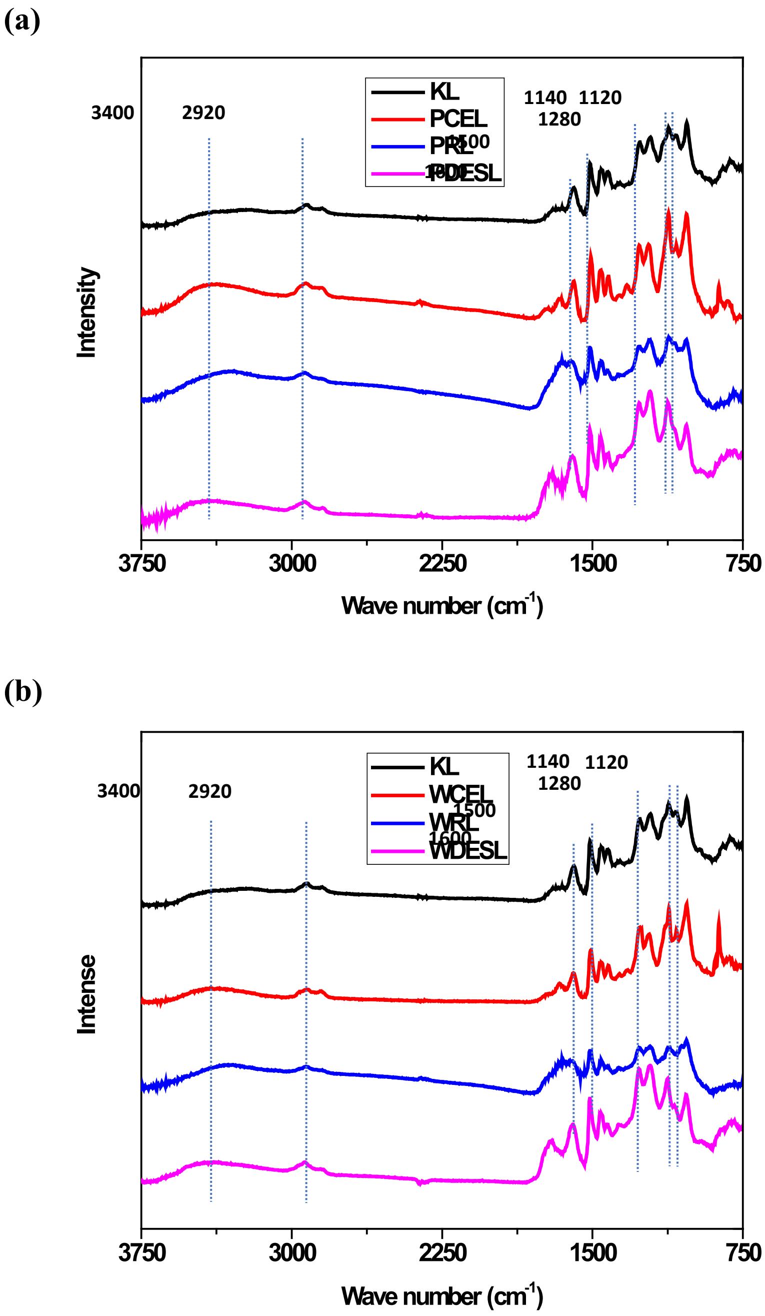

Figure 2.S3 FTIR spectra of Kraft lignin (KL) and cellulolytic enzyme lignin (CEL), residue lignin (RL) and DES extracted lignin (DESL) from a) peach and b) walnut endocarps.

Table 2.S1 Composition analysis for DES pretreatment of xylan and liquid fraction of endocarps

	Glucose, %	Xylose, %	Lignin, %	Residue, %	5-HMF, %	Furfural, %	Formic Acid, %	Levulinic Acid, %	ND, %
Xylan	ND	6.9 ± 0.2	ND	25.8 ± 0.0	0.7 ± 0.0	33.9 ± 6.5	2.9 ± 0.1	0.2 ± 0.0	29.6 ± 6.8
Peach endocarp	0.0 ± 0.0	0.2 ± 0.0	31.6 ± 0.7	15.0 ± 0.8	0.2 ± 0.0	2.8 ± 0.1	overlapped	overlapped	16 ± 3.7
Walnut endocarp	0.1 ± 0.0	0.3 ± 0.1	29.2 ± 0.3	18.0 ± 1.3	0.4 ± 0.0	2.3 ± 0.0	overlapped	overlapped	9.2 ± 3.3

CHAPTER 3. UNDERSTANDING SLOW PYROLYSIS OF LIGNIN BY LINKING PYROLYSIS CHEMISTRY AND CARBON MATERIAL PROPERTIES

Abstract

As a highly abundant renewable carbon source, lignin can be converted to a variety of advanced carbon materials with tailorable properties through slow pyrolysis. However, unlike fast pyrolysis of lignin which has been extensively investigated, the process of lignin slow pyrolysis is so far not well understood especially for the purpose of producing carbon materials. Therefore, in this study, slow pyrolysis of kraft lignin was investigated with a commercial pyrolysis–GC/MS system. The overall product distributions, including volatiles and solid product were tracked at different heating rates (2, 20, 40 ℃/min) and different temperature regions (100-200, 200-300 and 300-600 ℃). Solid residues were further characterized using a suite of analytical tools to determine the morphology, pore structure, conductivity, and interfacial chemical properties for potential material applications. This study provides insights into lignin slow pyrolysis chemistry and properties of the resulting carbon material thus helps a better design and control of lignin slow pyrolysis processes for synthesizing functional carbon material.

Keywords: Carbon materials, electrochemical storage, analytical pyrolysis, lignin, morphology

Introduction

Increasing frequency of extreme weather events and environmental deterioration as a result of anthropogenic climate change, has become a great threat around the globe. According a special report on global warming by the Intergovernmental Panel on Climate Change of the United Nations in 2018, the “human caused” carbon dioxide emissions has to be cut by 45% of the 2010 level by 2030 to avoid a rapid, far-reaching possibility of irreversible environmental damage [186]. In 2017, carbon dioxide emissions from burning fossil fuels for energy accounted for about 76% of total U.S. anthropogenic greenhouse gas emissions and about 93% of total U.S. anthropogenic CO_2 emissions [187]. Lignocellulosic-based biofuels are promising carbon-neutral alternatives to fossil fuels [188]. Lignocellulosic biomass consists primarily of cellulose, hemicelluloses and lignin. From a biorefinery perspective, polysaccharides (cellulose and hemicelluloses) provide a sugar stream for biofuel fermentation; while the value of lignin has not been fully tapped [4].

Lignin is the second most abundant biopolymers on earth after cellulose, which constitutes approximately one quarter of the terrestrial plant biomass [189]. Lignin polymer is made of three major phenylpropanes, namely *p*-hydroxybenzyl alcohol, coniferyl alcohol, and sinapyl alcohol, arranged in a hyperbranched topology through ether and/or C-C bonds [44]. Unlike cellulose, a straight chain polymer of glucose units, lignin is a highly cross-linked polyphenolic polymer with on ordered repeating units [190]. The highly heterogeneous structure of lignin makes it a difficult substrate for catalytic conversion to make molecules at high yield and selectivity. Proceeding from necessity of improving economy viability of biorefinery operation, a thrust on converting lignin into fuels and value-added products through thermochemical technologies has attracted new incentives.

Thermochemical conversion technologies, including pyrolysis, liquefaction, combustion and gasification, have attracted increasing interests as they offer a flexible and relatively simple way to convert biomass into electric power, heat, fuels and chemicals [191]. Fast pyrolysis, as a representative thermochemical conversion technique, has been favored for its capability of maximized conversion of biomass into a liquid oil (up to 70 wt.%) [192-194]. Numerous studies have reported using fast pyrolysis as a depolymerization method to obtain phenolic compounds from lignin [195]. Although it is generally accepted that pyrolysis of lignin involved with free phenoxyl radicals that formed by thermal decomposition [196], the formation mechanism of monomeric and oligomeric products has not been fully elucidated [38, 197-202]. According to a model proposed by Piscorz et al., lignin was first cracked into phenolic oligomers, from which a variety of phenolic monomers were formed during the secondary reactions [203]. A competing model proposed by Pushkaraj et al. believed that the oligomers were formed at secondary reactions through repolymerization of monomers generated from the primary reaction of lignin pyrolysis [204].

Over the last decade there has been a growing interest in converting lignin into functional carbon materials for various applications. For example, lignin, lignin-derived biochar and activated carbon as adsorbents to remove pollutant in water, including Pb, Cu, Zn, Cd, Ca, Sr, Cd, Cr, Sr and Li, have been examined [205]. Generated through thermochemical conversion and/or activation methodologies, lignin-derived carbon materials have demonstrated potential applications in energy storage materials, such as supercapacitor [44], anode [206] and cathode [207] of lithium-ion batteries. By doping functional groups, such as COOH, NH_2 and SO_3H, lignin-derived carbon material also found applications as metal-free solid acid catalysts which can be applied in a variety of acid catalyzed reactions, e.g. esterification and hydrolysis [34, 208]. Despite the fact that slow pyrolysis is one of the most commonly-used thermochemical methods to convert lignin into carbonaceous materials, operation parameters of slow pyrolysis and performance of the prepared carbon materials vary significantly in the literature [44]. For example, when converting lignin into activated carbon materials though slow pyrolysis for supercapacitor application, the temperature ranged from 500 to 1400 °C and heating rate ranged from 2 °C to 20 °C/min [34, 35, 44, 111]. Contradictory results have been reported on regarding how pyrolysis/carbonization temperature affect electrochemical performance of lignin-derived carbon material as electrode of supercapacitor. Activate carbon prepared from lignin-rich black liquor had a specific capacitance of 41.4 F/g when carbonized at 600 °C; while the capacitance decreased to 21 F/g when carbonized at 900 °C [209]. In another study, however, specific capacitance increased to 87 F/g at carbonization temperature of 900 °C using the same carbon precursor and activate agent [80]. Chen et al. reported lignin-derived C/Si nanoparticles composite through a one-pot, slow pyrolysis process. When lignin and Si nanoparticles were co-pyrolyzed at 800 °C and heating rate of 2 °C/min, the resulting material had a specific capacity of 1390 mAh/g [136] as compared to a much higher specific capacity of 2378 mAh/g at pyrolysis temperature of 600 °C [133].

Despite the wide use of slow pyrolysis to produce carbon materials from lignin, little information is available about the effects of slow pyrolysis conditions on reaction chemistry and correlation between pyrolysis chemistry and properties of the resulting carbon materials. In this study, slow pyrolysis of kraft lignin was investigated using a commercial pyrolysis–GC/MS system to recover and examine the multi-phased products generated from lignin thermal decomposition over the time course. The overall product distributions, including volatile and solid products were tracked at different heating rates (2, 20, 40 °C/min) and different temperature regions (100–200, 200–300 and 300–600 °C). Solid residues were further characterized to determine the morphology, pore structure, conductivity, and interfacial chemical properties for potential material application. The study provides mechanistic insights on the formation of intermediate monomers and oligomers and biochar during lignin slow pyrolysis, serving a basis for developing lignin-derived functional carbon materials.

Experimental

Materials

Phenol, acetic acid, acetone and methanol were purchased from Fisher Scientific Company. Kraft lignin, guaiacol, 4-propylphenol, vanillin and syringaldehyde were purchased from Sigma-Aldrich Company.

Evolved gas analysis-mass spectrometer (EGA-MS) analysis

At the EGA-MS mode, the micro-pyrolyzer was directly connected to a mass spectrometry (MS) detector (7890B/5977A, Agilent, Santa Clara, CA) through a deactivated metal tube (UA-DTM-2.5 N, Frontier Lab, Fukushima, Japan). Volatiles were able to be detected in real time by the MS without further separation by a GC column. For a typical EGA-MS analysis, 200 ± 10 μg of the kraft lignin placed in a deactivated stainless-steel cup was heated from 100 °C to 800 °C in a micro-pyrolyzer (EGA/PY-3030D, Frontier Lab, Fukushima, Japan) at a desired heating rate (2, 20 and 40 °C/min). The total ion thermogram (TIT) was displayed by recording total ion intensity of MS versus the programmed temperature.

Slow pyrolysis and heart-cutting-GC/MS (HC-GC/MS)

Pyrolysis tests were performed in a micro-pyrolyzer (EGA/PY-3030D, Frontier Lab, Fukushima, Japan). The temperature of the reactor can be precisely controlled from 40 to 900 °C with 1 °C intervals at preset heating rate. For each test, 1100 ± 50 μg of kraft lignin was put in the deactivated stainless-steel cup, loaded into the micro-pyrolyzer and pyrolyzed at set conditions. Helium was used as the carrier gas and the molecules generated by the micro-pyrolyzer were send to a GC/MS (7890B/5977A, Agilent, Santa Clara, CA) for composition analysis. The GC was equipped with a two-way splitter which directed the gas stream into both MS and flame ionization detector (FID). The MS was used for compound identification, which was connected with GC via a capillary column (Ultra Alloy-5, Frontier Lab, Fukushima, Japan). The FID detector was used for compound quantification. The calibration curves of the products were created using five different concentrations of acetic acid (carbohydrates), toluene (aromatic hydrocarbons), phenol (H type substances, C6 and C6C1), 4-propylphenol (H type substances, C6C2), guaiacol (G type substances, C6C1), vanillin (G type substances, other than C6C1), syringaldehyde (S type substances, PAHs, and long chain fatty acid) as standard compounds. The micro-pyrolyzer system was also equipped with a MicroJet Cryo-Trap suite (1030Ex, Frontier Lab, Fukushima, Japan) at the head of the GC column to selectively trap volatiles generated from desired temperature regions (100-200, 200-300, and 300-600 °C) with liquid nitrogen before transferring to GC/MS for detailed composition analysis, which is referred as heart-cutting (HC) in this study. The GC oven was hold at 40 °C for 2 min and then heated from 40 to 320 °C at a heating rate of 20 °C/ min then hold at 320 °C for an additional 10 min.

Characterization of lignin-derived solid residues

Scanning electron microscopy (SEM):

Images of the solid residue samples were obtained by a SEM (Quanta 250 FEG, Thermo Fisher Scientific, Madison, WI) operating at SE mode under low vacuum (0.40–0.65 Torr). The residue samples were sputter-coated in gold and the imaging was performed at beam accelerating voltages of 10 kV.

Fourier Transfer Infrared Spectrometry (FTIR):

IR analysis of KL and pyrolyzed KL samples was performed on a FTIR (Nicolet iS50, Thermo Fisher Scientific, Madison, WI) at a resolution of 4 cm^{-1} for 32 scans in the range of 450 to 4000 cm^{-1}. For a typical analysis, a background spectrum was obtained before pressing the powders samples against a diamond crystal to acquire data -. The background spectrum was subtracted, and each spectrum was baseline corrected using OMNIC 8.2 software.

Raman spectrometry:

Raman spectra of the samples were recorded with a DXR micro-Raman instrument (Thermo Scientific, West Palm Beach, FL). A diode-pumped Nd:YVO_4 green laser was used as an excitation source (λ=532 nm excitation). Each spectrum was deconvoluted using pseudo-Voigt function into four peaks around ~1190 cm^{-1}, ~1348 cm^{-1}, ~1474 cm^{-1} and ~ 1600 cm^{-1} corresponds to D1, D, D2 and G, respectively. D/G band ratio was evaluated by using both intensity/height ratio (I_D/I_G) and area ratio (A_D/A_G). Finally, the lateral size of a domain, L_a(nm) was calculated according to following equations [210].

$$L_{a,I} = (C_0 + \lambda C_1)\left(\frac{I_D}{I_G}\right)^{-1} \text{ and } L_{a,A} = (C_0 + \lambda C_1)\left(\frac{A_D}{A_G}\right)^{-1}$$

Where,

$L_{a,I}$ = lateral size of a domain based on peak height (nm)

$L_{a,A}$ = lateral size of a domain based on peak area (nm)

C_0 = Wavelength-dependent prefactor (-12.6 nm)

λ = laser wavelength (532 nm)

C_1 = Wavelength-dependent prefactor (0.033)

I_D/I_G = Height ratio of D to G peak

A_D/A_G = Area ratio of D to G peak

Brunauer–Emmett–Teller (BET):

The BET surface area was determined using a gas adsorption analyzer (TRISTAR 3000, Micromeritics Instruments, Norcross, GA). In each test, approximately 100 mg of sample was used. Nitrogen was the adsorption gas and the analysis were performed at the boiling temperature of liquid nitrogen. Samples were degassed under vacuum at 160 °C overnight before the BET measurements to obtain the specific surface areas.

X-ray photoelectron spectroscopy (XPS):

KL and pyrolyzed samples were prepared by pressing into a pallet and mounted on a conductive silicon wafer using conductive carbon tape. XPS (K-Alpha, Thermo Fisher Scientific, Madison, WI) measurements were conducted by focusing on monochromatic Al K-α radiation (energy of 1486.6 eV) onto a 400 μm diameter focused spot on the sample.

Results and discussion

EGA-MS analysis of lignin slow pyrolysis

Figure 3.1 shows the total ion thermogram (TIT) obtained from the EGA-MS analysis of kraft lignin from 100 to 800 ℃ at different heating rates. At the heating rate of 2 ℃/min, there were two continuous peaks can be observed from the TIT profile at around 220 ℃ and 334 ℃. Similar trend can be observed from differential thermogravimetric (DTG) curves, where the first peak is primarily related to the release of light phenols and gas molecules (H_2, CO and CO_2) derived by the cleavage of lateral β-ethers; while the second peak representing the formation of phenolic monomer, dimers and oligomers as the scission of aryl ether bonds [211, 212]. The volatiles evolved from lignin decomposition terminated at approximately 500 ℃ thus nearly no signal was detected at temperatures > 500 ℃. In comparison, at heating rate of 20 ℃/min, there was an additional peak appeared at 175 ℃ and the overall EGA profile was shifted toward higher temperature. The volatiles evolved from lignin decomposition terminated at approximately 600 ℃ at heating rate of 20 ℃/min. As heating rate further increasing to 40 ℃/min, no clear difference was observed as compared to the profile obtained at heating rate of 20 ℃/min. The EGA profiles provided a rough snapshot about lignin decomposition and products distribution across 100 to 800 ℃, with which we can use to divide the pyrolysis course into three continuous regions, 100–200, 200–300 and 300–600 ℃ to investigate the detailed volatiles composition for each temperature region.

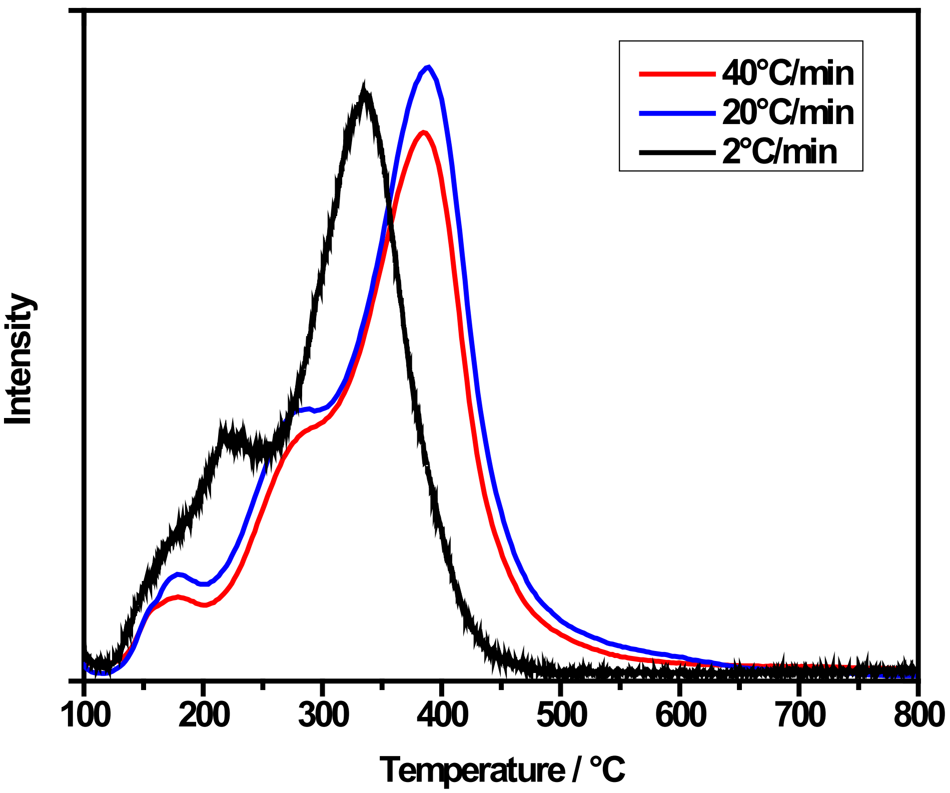

Figure 3.1 Total ion thermogram (TIT) of kraft lignin using EGA-MS analysis from 100 to 800 °C at a heating rate of 2 °C/min, 20 °C/min and 40 °C/min.

Products distribution of lignin slow pyrolysis at 2 °C/min heating rate

Table 3.1 shows the yields of GC/MS detectable volatile compounds and solid residues from kraft lignin slow pyrolysis at different heating rates (2, 20 and 40 °C/min) and three temperature regions: 100–200, 200–300 and 300–600 °C. In order to understand the effect of temperature, the product distribution was first compared at heating rate of 2 °C/min. It was not surprising that the overall volatiles yield increased when temperature increases. For example, the decomposition of lignin slow pyrolysis started at low temperature and the volatiles yield was 1.73 g/100g lignin, 5.78 g/100g lignin and 16.38 g/100g lignin at 100–200, 200–300 and 300–600 °C, respectively. Regardless of the heating rates, 2-methoxy-4-vinylphenol was the most primary product (22.4–25.5 g/100g lignin) and other major products include hydrocarbons (2-butene, benzene, toluene and xylenes), carbohydrates (acetic acids, acetone and several long chain fatty acids), phenolic compounds (phenol, 2-methylphenol, guaiacol, 2,4-dimethylphenol, cresol, 4-ethyl-2-methoxyphenol, 2-methoxy-4-propenylphenol, homovanillic acid, 3,5-dimethoxy-4-hydroxyacetophenone, etc.) and polycyclic aromatic hydrocarbons (PAHs) (2,3,8-thihydroxy-4-isopropyl-6-methyl-1-naphthaldehyde, 6-methoxyhemigossypol, 5-methoxy-7-methylbenz(a)anthracene, benzo[vwx]hexaphene). The detailed product distribution and formation mechanism of each category during slow pyrolysis was discussed under heating rate of 2 °C/min.

Table 3.1 Product distribution of kraft lignin slow pyrolysis at multiple temperature regions

Compound name	**2** °C **/ min**			**20** °C **/ min**			**40** °C **/ min**		
	100-200 °C	**200-300** °C	**300-600** °C	**100-200** °C	**200-300** °C	**300-600** °C	**100-200** °C	**200-300** °C	**300-600** °C
2-butene	0.04 ± 0.06	0.42 ± 0.03	0.24 ± 0.01	0.06 ± 0.02	0.22 ± 0.04	0.26 ± 0.06	0.03 ± 0.01	0.16 ± 0.01	0.26 ± 0.02
acetone	-	0.01 ± 0.00	0.07 ± 0.02	-	0.01 ± 0.00	0.08 ± 0.01	-	-	0.07 ± 0.01
benzene	-	0.01 ± 0.00	0.37 ± 0.00	-	-	0.28 ± 0.03	-	-	0.50 ± 0.05
acetic acid	0.01 ± 0.01	-	0.48 ± 0.01	0.05 ± 0.02	-	0.15 ± 0.00	0.05 ± 0.01	-	0.13 ± 0.08
toluene	0.01 ± 0.00	0.02 ± 0.00	0.64 ± 0.02	-	0.01 ± 0.00	0.65 ± 0.08	-	-	0.57 ± 0.04
3-furaldehyde	0.01 ± 0.00	0.07 ± 0.00	0.01 ± 0.00	-	0.12 ± 0.02	0.07 ± 0.00	-	0.10 ± 0.01	0.08 ± 0.02
ethylbenzene	-	-	0.01 ± 0.00	-	-	0.01 ± 0.00	-	-	0.01 ± 0.00
xylenes	-	0.03 ± 0.00	0.30 ± 0.02	-	0.01 ± 0.00	0.29 ± 0.06	-	0.01 ± 0.00	0.25 ± 0.03
phenol	0.06 ± 0.01	0.07 ± 0.00	1.53 ± 0.04	0.04 ± 0.01	0.06 ± 0.01	1.64 ± 0.12	0.05 ± 0.00	0.04 ± 0.00	1.66 ± 0.18
methylphenols	-	0.11 ± 0.01	1.53 ± 0.01	-	0.12 ± 0.03	1.32 ± 0.09	-	0.09 ± 0.01	1.32 ± 0.05
guaiacol	0.16 ± 0.02	0.12 ± 0.00	0.86 ± 0.00	0.15 ± 0.01	0.08 ± 0.03	1.27 ± 0.07	0.14 ± 0.00	0.05 ± 0.02	1.26 ± 0.05
dimethylphenols	0.08 ± 0.01	0.03 ± 0.00	1.01 ± 0.05	0.08 ± 0.00	0.05 ± 0.02	1.03 ± 0.04	0.07 ± 0.00	0.04 ± 0.01	1.01 ± 0.05
creosol	-	0.15 ± 0.02	2.01 ± 0.00	-	0.05 ± 0.00	2.31 ± 0.03	-	0.03 ± 0.00	2.35 ± 0.06
3,4-dimethoxytoluene	-	-	0.12 ± 0.00	-	-	0.10 ± 0.00	-	-	0.09 ± 0.00
1,2-bizenediol,3-methyl	-	0.02 ± 0.00	0.45 ± 0.06	-	0.02 ± 0.01	0.45 ± 0.02	-	0.01 ± 0.00	0.46 ± 0.03
4-ethyl-2-methoxyphenol	0.01 ± 0.00	0.03 ± 0.01	0.57 ± 0.05	0.01 ± 0.00	0.01 ± 0.00	0.84 ± 0.01	0.01 ± 0.00	0.01 ± 0.00	0.85 ± 0.02
2-methoxy-4-vinylphenol	0.11 ± 0.03	2.32 ± 0.06	3.67 ± 0.07	0.03 ± 0.01	0.82 ± 0.14	4.69 ± 0.22	0.02 ± 0.00	0.49 ± 0.03	5.20 ± 0.08
2,6-dimethoxyphenol	0.05 ± 0.00	0.04 ± 0.00	0.26 ± 0.02	0.05 ± 0.00	0.02 ± 0.01	0.39 ± 0.03	0.04 ± 0.00	0.02 ± 0.01	0.39 ± 0.01
trans-isoeugenol	-	0.03 ± 0.00	0.11 ± 0.01	-	0.02 ± 0.00	0.13 ± 0.01	-	0.02 ± 0.00	0.16 ± 0.01
2-methoxy-4-propylphenol	-	-	0.07 ± 0.01	-	-	0.11 ± 0.00	-	-	0.10 ± 0.00
4-ethylcatechol	-	0.01 ± 0.00	0.13 ± 0.02	-	-	0.11 ± 0.01	-	-	0.10 ± 0.00
vanillin	0.08 ± 0.03	0.11 ± 0.01	0.06 ± 0.00	0.05 ± 0.00	0.12 ± 0.00	0.12 ± 0.00	0.04 ± 0.00	0.10 ± 0.01	0.14 ± 0.00
isoeugenol	0.01 ± 0.00	0.30 ± 0.01	0.48 ± 0.01	-	0.18 ± 0.00	0.75 ± 0.02	-	0.13 ± 0.01	0.84 ± 0.02
apocynin	0.07 ± 0.00	0.06 ± 0.00	0.10 ± 0.00	0.04 ± 0.00	0.06 ± 0.00	0.16 ± 0.00	0.03 ± 0.00	0.06 ± 0.00	0.15 ± 0.01
benzene, 1,2,3-trimethoxy-5-methyl-	0.04 ± 0.02	0.16 ± 0.04	0.22 ± 0.01	0.02 ± 0.00	0.03 ± 0.00	0.43 ± 0.02	0.02 ± 0.00	0.02 ± 0.00	0.44 ± 0.02
2-propanone, 1-(4-hydroxy-3-methoxyphenyl)-	0.02 ± 0.00	0.10 ± 0.01	0.06 ± 0.00	0.01 ± 0.00	0.08 ± 0.01	0.14 ± 0.00	-	0.06 ± 0.01	0.16 ± 0.01
3,5-dimethoxyacetophenone	-	0.06 ± 0.01	0.08 ± 0.01	-	0.02 ± 0.00	0.09 ± 0.00	-	0.01 ± 0.00	0.10 ± 0.00
methyl homovanillate	-	-	0.03 ± 0.02	-	-	0.04 ± 0.01	-	-	0.06 ± 0.00

3-ethoxy-4-methoxybenzaldehyde	0.08 ± 0.01	0.16 ± 0.01	0.25 ± 0.07	0.04 ± 0.00	0.08 ± 0.00	0.30 ± 0.04	0.02 ± 0.00	0.08 ± 0.01	0.38 ± 0.01
homovanillic acid	0.21 ± 0.00	0.18 ± 0.01	0.11 ± 0.01	0.07 ± 0.00	0.26 ± 0.01	0.21 ± 0.01	0.04 ± 0.00	0.24 ± 0.01	0.24 ± 0.01
2,6-dimethoxy-4-allylphenol	0.04 ± 0.02	0.10 ± 0.01	0.10 ± 0.00	0.01 ± 0.00	0.07 ± 0.00	0.15 ± 0.01	0.01 ± 0.00	0.06 ± 0.00	0.21 ± 0.00
acetophenone, 4'-hydroxy-3,5-dimethoxyphenhl	0.25 ± 0.01	0.22 ± 0.01	0.18 ± 0.01	0.05 ± 0.03	0.34 ± 0.03	0.34 ± 0.06	0.03 ± 0.02	0.28 ± 0.01	0.38 ± 0.07
hexadecanoic acid	0.28 ± 0.11	0.02 ± 0.00	0.01 ± 0.00	0.17 ± 0.18	0.30 ± 0.12	0.05 ± 0.04	0.13 ± 0.17	0.19 ± 0.12	0.03 ± 0.01
oleic acid	0.16 ± 0.21	0.08 ± 0.00	0.01 ± 0.00	0.01 ± 0.01	0.24 ± 0.18	0.11 ± 0.10	0.01 ± 0.01	0.35 ± 0.17	0.11 ± 0.12
octadecanoic acid	0.16 ± 0.12	0.05 ± 0.00	0.01 ± 0.00	0.07 ± 0.08	0.29 ± 0.03	0.06 ± 0.06	0.05 ± 0.06	0.27 ± 0.19	0.04 ± 0.01
2,3,8-thihydroxy-4-isopropyl-6-methyl-1-naphthaldehyde	0.01 ± 0.00	0.08 ± 0.01	0.07 ± 0.00	-	0.05 ± 0.01	0.16 ± 0.01	-	0.04 ± 0.01	0.18 ± 0.01
6- methoxyhemigossypol	-	0.04 ± 0.00	0.11 ± 0.01	-	0.06 ± 0.03	0.38 ± 0.08	-	0.03 ± 0.02	0.36 ± 0.07
5-methoxy-7-methylbenz(a)anthracene	0.02 ± 0.02	0.48 ± 0.02	0.12 ± 0.00	-	0.21 ± 0.11	0.37 ± 0.00	-	0.17 ± 0.05	0.45 ± 0.01
secoisolariciresinol	-	0.33 ± 0.02	0.16 ± 0.01	-	0.07 ± 0.00	0.42 ± 0.04	-	0.04 ± 0.01	0.47 ± 0.02
benzo[vwx]hexaphene	-	0.37 ± 0.02	0.24 ± 0.01	-	0.06 ± 0.03	0.48 ± 0.07	-	0.04 ± 0.01	0.55 ± 0.03
Total volatiles yield	1.73 ± 0.70	5.78 ± 0.31	16.38 ± 0.56	0.97 ± 0.33	3.71 ± 0.86	20.03 ± 1.41	0.77 ± 0.28	2.92 ± 0.71	21.08 ± 1.13
Char weight		47.46 ± 2.95			42.02 ± 3.31			41.57 ± 2.49	
Total yield		71.35 ± 4.52			66.73 ± 5.91			66.33 ± 4.62	

Although it is commonly believed that lignin pyrolysis goes through two-step reactions, primary and secondary, the formation mechanism of intermediate products has not reached a general agreement. Demirbaş suggested that the phenolic compounds and their alkyl substituted products were formed by recombination and cyclization reactions from C2, C3 and C4 fragments via aldol condensation [213]. Branca et al. believed that guaiacol and syringol were the intermediate species of pyrolysis and phenols were formed by demethylation rather than demethoxylation from guaiacol in the secondary reactions [201, 202]. Li et al. proposed that vinylphenols (4-vinylphenol and 2-methoxy-4-vinylphenol) were the principle products generated from the cleavage of β-*O*-4 linkages; while the other phenolic compounds (H and G type), including phenol, ethylphenol, guaiacol, methylguaiacol, ethylguaiacol, trans-isoeugenol and vanillin were generated via the secondary reactions from the vinylphenols [38]. Results from our study at heat rate of 2 °C/min, show the yield of 2-methoxy-4-vinylphenol was 6.1 g/100g lignin, accounting for 25.5% of total yield of GC/MS detectable phenolic compounds from 100-600 °C. Particularly, in the temperature region of 200–300 °C and at a heating rate of 2 °C/min, the yield of 2-methoxy-4-vinylphenol was 2.32 g/100g lignin, accounting for 40.14% of total phenolic compounds yield at that temperature region. The dominant yield of 2-methoxy-4-vinylphenol supports that vinylphenols are the preferential products of β-*O*-4 cleavage linkages during pyrolysis of lignin.

Interestingly, unlike a previous report [38] in which both 4-vinylphenol and 2-methoxy-4-vinylphenol were the dominant products, there was no 4-vinylphenol seen in the present study. After evaluated the kraft lignin with ^{13}C-^{1}H Heteronuclear Single Quantum Coherence Nuclear Magnetic Resonance (HSQC NMR), we believed the lignin source might contribute to the absence of 4-vinylphenol. As can be seen from **Figure 3.S1**, the NMR spectra of aromatic regions revealed the chemical structure of kraft lignin was dominated by G-unit (96.4%) along with S (3.6%) and no H-units were observed. Whereas the corn stover lignin mentioned in a previous study [38] had roughly the same amount of H (36 mol%), G (34 mol%) and S (30 mol%) units[214], which explained the presence of 4-vinylphenol in pyrolysis products. Therefore, 4-vinylphenol and 2-methoxy-4-vinylphenol were the primary products corresponding to a cleavage of the β-O-4 linkages that connect with H-units and G-units. For kraft lignin, no 4-vinylphenol was produced due to the absence of H-unit.

In addition to 2-methoxy-4-vinylphenol, a variety of other phenolic monomers were detected. The compounds were categorized into p-hydroxyphenyl (H), guaiacyl (G) or syringyl (S) type. At heating rate of 2 °C/min, the overall yield of G type compounds was 12.05 g/100g lignin (guaiacol, creosol, 4-ethyl-2-methoxyphenol, 2-methoxy-4-vinylphenol, 2-methoxy-4-propylphenol, vanillin, isoeugenol, apocynin, guaiacylacetone, methyl homovanillate, and homovanillic acid), accounting for 50.44% of total GC/MS detectable volatiles yield. The overall yields of H-type (phenol, methylphenols, dimethylphenols, and 4-ethylcatechol) and S-type (2,6-dimethoxyphenol, 2,6-Dimethoxy-4-allylphenol) compounds were 4.56 and 0.59 g/100g lignin, respectively, accounting for 19.00% and 2.47% of total GC/MS detectable volatiles yield. Because the primary products were highly reactive and vulnerable to a series of secondary reactions during pyrolysis, H-type compounds could be derived from 2-methoxy-4-vinylphenol as secondary reaction products during pyrolysis[38]. However, S-type compounds cannot be obtained from pyrolysis of H or G-units[43, 215-217]. In fact, demethoxylation of S-type compounds can only occurred to a very minor extent (0.6%) at pyrolysis temperature of 650 °C[215]. Therefore, the production of S type compounds can only be related to the S-unit of lignin and the low yields of S type compounds can be self-explained by low S-unit content in the staring lignin.

In addition to phenolic monomers, pyrolysis of lignin also generated a small amount of light hydrocarbons (2.09 g/100g lignin), short-chain carbohydrates/or carboxylic acids (1.44 g/100g lignin) and polycyclic aromatic hydrocarbons (PAHs) (1.54 g/100g lignin) at heating rate of 2 °C/min, as shown in **Table 3.S1**. The yield of light hydrocarbons accounts for 8.75% of the total GC/MS detectable volatiles yield. The light hydrocarbons were probably generated through a combination of dehydration, dihydroxylation and dealkylation of phenols [218]. About 43.75% of the total GC/MS detectable carboxylic acids were generated in the 100–200 °C region, of which 95.24% was fatty acids, including hexadecanoic acid, oleic acid and octadecanoic acid. The formation of the light carboxylic acids was attribute to the recombination and cyclization of the initial degraded C2, C3 and C4 fragments [213]. As the pyrolytic temperature increases, the yield of fatty acids declined while the other short-chain carboxylic acids and hydrocarbons (such as acetic acid, benzene, toluene, and xylene) increased. The intensity of reaction enhances with increasing temperature, at high temperature, the propagation of reaction does not favor the formation of those long chain fatty acid. The significantly increasing C2, C3, C4 and C5 units with temperature also supported the hypothesis that the long chain fatty acids derived from the recombination and condensation of low molecular compounds [177, 213]. In addition, at heating rate of 2 °C/, the yield of PAHs accounts for 6.45% of the total GC/MS detectable volatiles yield. It was believed that the formation and augmentation of PAHs from the combustion of gasoline was involved the recombination reaction of multiple light aliphatic hydrocarbons, such as acetylene and ethylene [219]. However, pyrolysis does not generate such a large amount of short hydrocarbons to fuel the augmentation of PAHs. Zhou et al. proposed that the PAHs were formed from the condensation of single ring aromatic hydrocarbons, such as benzene, toluene, xylene, which derived from demethoxylized guaiacol or syringol [220]. In the present study, however, we found that the occurrent of PAHs was started at very low temperature (100-200 ℃) and there was almost no aromatic hydrocarbon yield at that temperature region. Plus, it was observed that there were plenty of functional groups substituted on the benzene rings of PAHs rather than simple condensation of several neat benzene rings. Therefore, the majority of PAHs were more likely formed from repolymerization of phenolic monomers [221]. The yield of PAHs was 0.97 g/100g lignin between 200-300 ℃, which was significantly higher than that between 300-600 ℃ of 0.54 g/100g lignin. The decreasing yield of PAHs can be attributed to the fact that depolymerization outcompeted the repolymerization at high temperature [222].

At heating rate of 2 ℃/min, around 47.46 g/100g lignin of solid residue remained after pyrolysis. In terms of formation mechanisms, the solid product of lignin pyrolysis can be classified into two distinct categories: 1) the residue of lignin pyrolytic depolymerization is the most primary solid component, referred as char in the present study; 2) repolymerization of PAHs and phenolic radicals propagates the formation of repolymerized char, also referred as coke [43]. For fast pyrolysis which mainly focused on volatiles (bio-oils, low molecular molecules), rather than solid residues, the distinctions between coke and char were usually ignored in most publications and all solid residues, both coke and char, were indiscriminately called “char”. However, it is necessary to take this mechanistic difference into account in the discussion of slow pyrolysis since the primary application of the solid products would be functionalized carbon materials.

The effect of heating rate on lignin slow pyrolysis

Solid residues yield was known to increase with the decrease of heating rate at expense of gaseous volatile products for lignin fast pyrolysis [189, 223], which was in good agreement with results of present study. When comparing different temperature regions across various heating rates, it was noticed that 2-methoxy-4-vinylphenol constituted the largest amount among all GC/MS detectable volatiles at both low (100-300 °C) and high (300-600 °C) temperature regions. The ratios of the 2-methoxy-4-vinylphenol yield to the yield of all other G type compounds were 0.54, 0.72 and 1.52, respectively, at 40, 20 and 2 °C/min at low temperature region (100-300 °C). The increasing ratio following decreasing heating rates suggests that more 2-methoxy-4-vinylphenol was converted to other G-type compounds through secondary reactions. While at the high temperature region (300-600 °C), the ratios were 0.85, 0.79 and 0.85 for 40, 20 and 2 °C/min heating rate, respectively. Results indicate that rate of the secondary reactions tends to be consistent across all heating rates at high temperatures.

Lignin pyrolysis proceeds via free radical reactions, which is temperature dependent [224]. The concentration of free radicals at low temperature region was lower than that of high temperature region [224]. But, at the same (low) temperature, compared to lower heating rate (2 °C/min), the concentration of free radicals would be much higher at higher heating rate (20 or 40 °C/min) in the pyrolyzer reactor because in the same unit of time (the time for free radicals transferring to MS from pyrolyzer with carrier gas) more radicals were generated at high rather than low heating rate (2 °C/min). But, at high temperature region, the concentration of free radicals would be increased significantly so that the difference caused by various heating rates could be neglected, which can be partially proved by the very similar conversion rate of 2-methoxy-4-vinylphenol to other G-type compounds.

The enhanced heating rate lead to higher reaction severity, which can cause fast release of gases and volatiles due to continuous blasts during pyrolysis. In comparison, at low heating rate of slow pyrolysis, the free radicals have better chance to repolymerize with themselves to form PAHs and with char to form coke, which lead to increasing yield of the solid residues. And the decreasing yields of GC/MS detectable PAHs with the decrease of heating rate can be explained by the increasing of coke due to the repolymerization of GC/MS detectable PAHs.

Characterization of lignin-derived solid residue

Morphology of the solids

SEM images of solid residues collected from pyrolysis of kraft lignin at different temperatures and 2 °C/min heating rate are shown in **Figure 3.2**. Images of the solid residues generated at low pyrolysis temperatures of 200 °C (**Figure 3.2a and 2b**) and 300 °C (**Figure 3.2c and 2d**), showed rough surfaces, clumps and sign of matrices and tunnels, indicating the lignin particles had been melted and fused into large sphere shape particles, which was also reported in other literatures [44, 189]. When pyrolysis temperature increased to 500 °C, as shown in **Figure 3.2e-h**, the rough surface of the solid residue became smoother (**Figure 3.2e and 2f**), and tunnels and pores of different sizes were observed on the solid residue, as can be seen in **Figure 3.2g** and 2h. The tunnels and pores could be signs of volatiles generation at high pyrolysis temperature of 500 ℃. Interestingly, at pyrolysis temperature of 700 ℃, a thin layer of dust-like fine particles was observed on the surface of solid residue (**Figure 3.2j**), probably due to coke formation from repolymerization of the phenolic free radicals and PAHs [225, 226]. While debris and cracks showed a clear sign of crystallization and brittle properties (visually examined during grinding) can be seen on the surface of the solid residues collected at 800 ℃ (**Figure 3.2l**). In addition, the average particle size of the solid residue was decreased as pyrolysis temperature increases from 500 to 800 ℃, likely due to particles were much easier to be broken down when grinding due to the increased modulus of elasticity (increased brittleness) with temperature [227]. In brief, the SEM images were consistent with the previous discussion on mechanics and demonstrate solid residue forming processes from lignin with temperature increase.

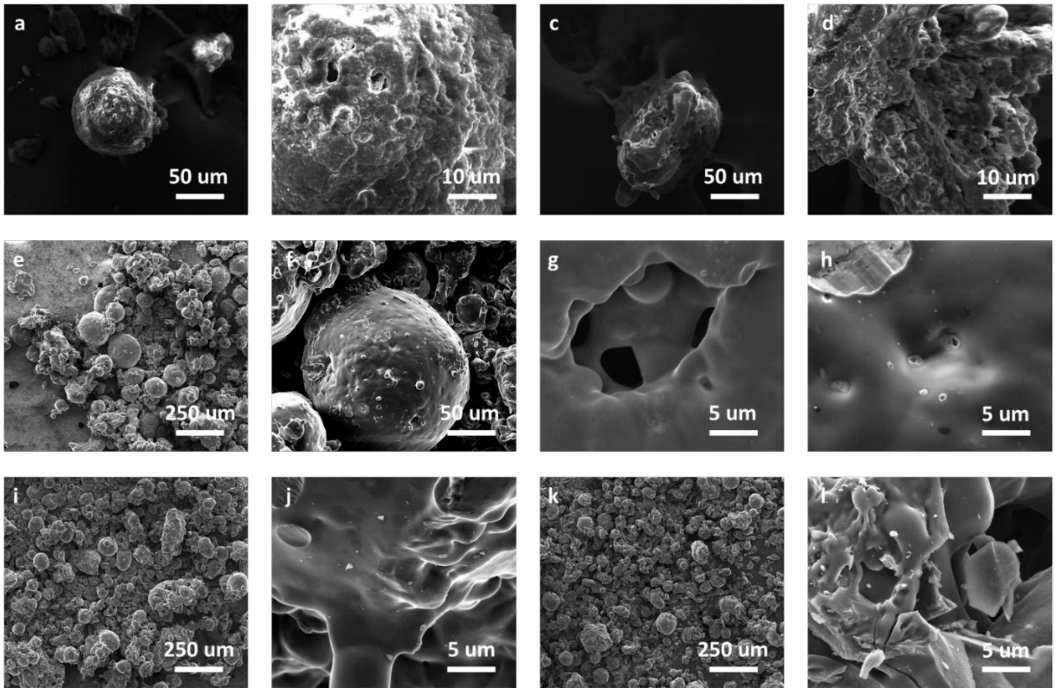

Figure 3.2 SEM images obtained from solid residues of pyrolysis of kraft lignin under heating rate of 2 ℃/min at multiple temperature regions: a) and b) 200 ℃; c) and d) 300 ℃; e) to h) 500 ℃; i) and j) 700 ℃; k) and l) 800 ℃ at different magnifications.

Compositional and physical properties of the solid residues

The properties of lignin derived solid residues collected at 300, 600 and 800 °C are shown in **Table 3.2**. As the temperature increases, the C content increases while H, N and O contents decrease. The H/C ratio indicates the aromaticity and stability of the solid residues; while O/C ratio clearly indicates the polarity and the abundance of oxygen containing functional groups in the solids [228]. The decreasing in H/C and O/C atomic ratios clearly indicates that the relative degree of aromaticity and polarity decreases as pyrolysis temperature increases. Physical properties, including specific surface area and conductivity, were also characterized. The surface area for solid residue collected from pyrolysis at 300 °C was too low to quantify, indicating the carbonization at this temperature just started and no pore structure had formed or the pores in the raw lignin collapse at low temperature due to melting/transitioning to glass state [189]. As pyrolysis temperature increases, specific surface areas of the lignin-derived solid residues increased, reaching 174 and 576 m^3/g for solids collected at 600 and 800 °C, respectively.

Table 3.2 Composition, physical properties and higher heating value (HHV) of solid residues from slow pyrolysis of kraft lignin at multiple temperature regions

Residue	C	H	O	N	Others	Atomic H/C	Atomic O/C	Surface Area m^2g^{-1}
300 °C	66.9±1.4	5.3±0.0	26.5±0.1	0.2±0.0	1.1±1.5	0.94±0.0	0.30±0.1	-
600 °C	85.7±1.8	3.0±0.0	7.1±0.1	0.3±0.0	3.9±1.9	0.42±0.0	0.06±0.0	174
800 °C	90.0±1.9	1.7±0.0	4.1±0.1	0.4±0.0	3.8±2.0	0.23±0.0	0.03±0.0	576

Chemical characterization of solid residues

FTIR analysis offers a better understanding of the impact of pyrolysis temperature on the chemical structure of solid residues. **Figure 3.3a** shows FTIR spectra of KL, seven solid residues collected via pyrolysis from 200 to 800 °C with a 100 °C interval and solid residue collected from pyrolysis at 800 °C followed by a two-hour hold. No significant differences can be spot between the spectra of KL and solid residue collected at 200 °C, indicating relatively stable chemical structure under low temperature. However, declining IR signals were observed, suggesting decreasing functional groups in the solids (increasing carbonization extent) with pyrolysis temperature increasing from 200 to 600 °C. The broad IR band around 3100~3600 cm^{-1}(attributed to hydrogen bonded -OH) and peaks around 2843~2936 cm^{-1}(attributed to -CH$_n$ stretching) were reduced, which was evidence of lignin dehydration and decomposition of lignin side chains. The reducing peaks at ~1701 cm^{-1} (C=O) and 1030 cm^{-1} and 1081 cm^{-1} (both attributed to C-O bonds) likely owing to cracking and reformation of carboxyl (-COOH), carbonyl (-C=O) and ether-based groups (R-O-R). Peaks at 1425 cm^{-1} (attributed to methoxyl), and 1265 cm^{-1} and 1364 cm^{-1} (attributed to aromatic-bonded oxygen) were gradually decreased, confirming the demethoxylation of G type substrates from pyrolysis occurring at lower temp (200-400 °C) [202]. When pyrolysis temperature increased higher than 700 °C, the IR signals of solids became nearly unapparent due to the completion of lignin decomposition.

Figure 3.3b illustrates well defined Raman signals were obtained for the sample residues obtained above 400 °C. These Raman signals were deconvoluted into four pseudo-Voigt shaped peaks at ~1170 cm^{-1}(D1), 1345 cm^{-1}(D), 1500 cm^{-1}(D2) and 1600 cm^{-1}(G). The band around 1170 cm^{-1} is related to interstitial defects, oxygen superficial groups and ions impurities [229]. D band at 1345 cm^{-1} is related to the disordered carbon [230]. Any defect that breaks the symmetry of the graphite increases the intensity of D-band. G-band at 1600 cm^{-1} is associated with the E$_{2g}$ vibration mode of graphitic lattice (stretching vibration between any pair of *sp2* carbon atoms) [231]. Overall, D, D2 and G bands related to *sp2* bonded turbostratic nanocrystalline carbon [232]. Based on **Table 3.3**, it was noted that the increasing temperature increases the I_D/I_G ratio or A_D/A_D ratio. For disordered carbon materials these ratios can be related to the lateral size of the graphene domain (L_a). Calculated La values are shown in **Table 3.3**. Furthermore, these values are plotted in **Figure 3.3c**. It is evident that at 500 °C, L_a has the highest value. When the temperature increases from 500 °C to 800 °C, L_a decreases gradually. This trend is consistent with the SEM results which shows the average particle size decreases from 500 °C to 800 °C.

Table 3.3 Structural parameters calculated from Raman measurements

Sample	**I_D**	**I_G**	**A_D**	**A_G**	**I_D/I_G**	**A_D/A_G**	**$L_{a,I}$/nm**	**$L_{a,A}$/nm**
KL-400	297	372	68177	48140	0.798	1.416	6.207	3.499
KL-500	275	397	60117	47097	0.692	1.276	7.161	3.882
KL-600	233	332	44349	29364	0.701	1.510	7.066	3.281
KL-700	66	71	14123	6605	0.934	2.138	5.302	2.318
KL-800	115	105	21196	9288	1.094	2.281	4.529	2.171
KL-800-Hold	110	100	19264	8731	1.103	2.206	4.490	2.246

*KL-400 to 800 represent solid residues obtained from pyrolysis of kraft lignin under heating rate of 2 ℃ /min at multiple temperature from 400 to 800 ℃; KL-800-Hold represents solid residues obtained from pyrolysis of kraft lignin under heating rate of 2 ℃/min at 800 ℃ followed by holding at 800 ℃ for 2 hours.

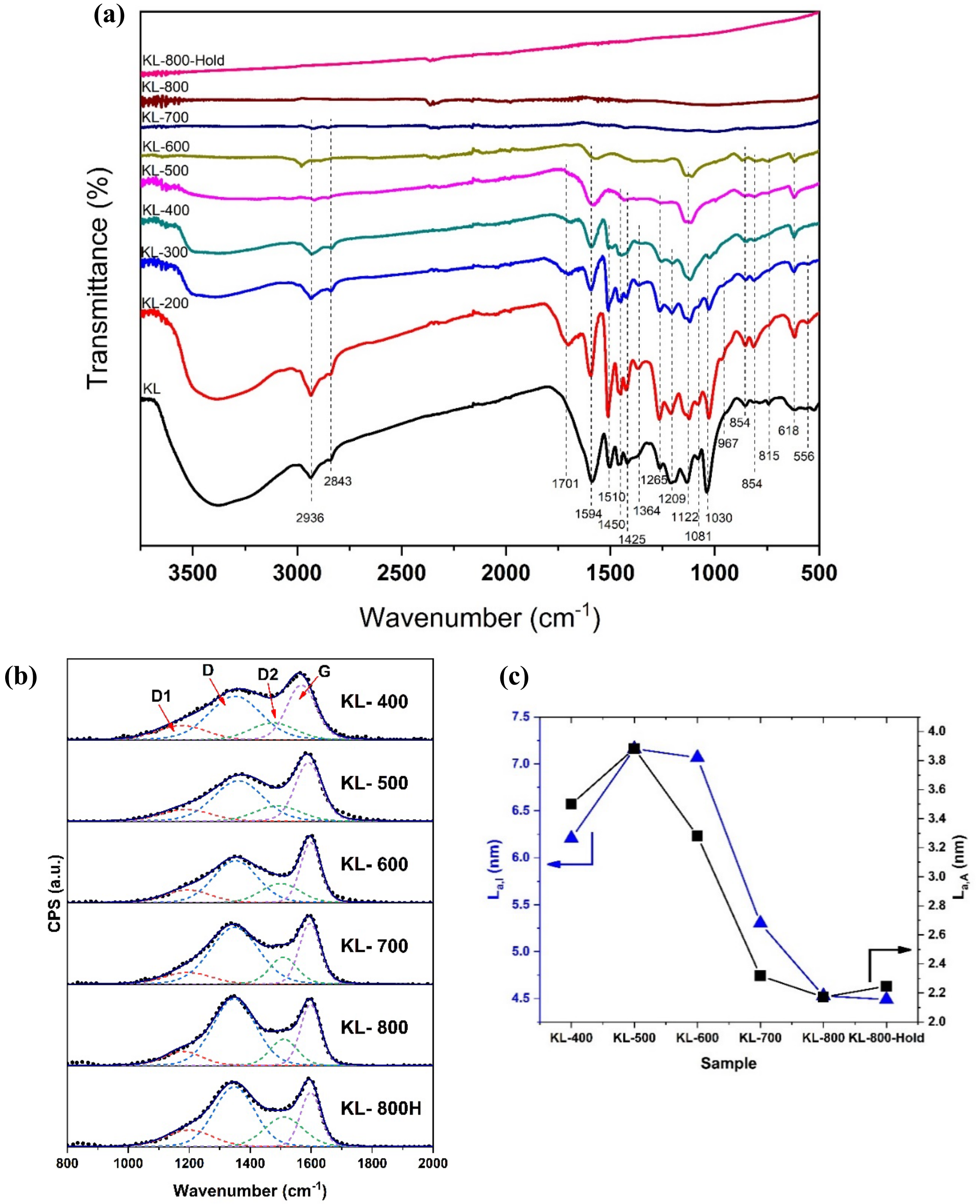

Figure 3.3 a) FTIR, b) Raman spectrums and c) $L_{a,1}$ and $L_{a,A}$ of kraft lignin slow pyrolysis at multiple temperature regions. $L_{a,1}$ is lateral size of a domain based on peak height (nm); $L_{a,A}$ is lateral size of a domain based on peak area (nm).

XPS analysis examined the surface chemistry transformation of the pyrolytic biochar with temperature increase. **Figure 3.4** shows the XPS survey spectra and high resolution C1s spectra of solids obtained from KL pyrolyzed at different temperatures. **Table 3.4** summarized the elemental composition and chemical states in each sample based on the XPS analysis. Adhering to previous discussions, the dropping C-O content indicated cracking and reformation of ether linkages, while the growing C-C(sp^2) carbon suggested an increasing aromaticity and carbonized material. It was noted that the oxygen content in the solids gradually decreases, while carbon content increases as the pyrolysis temperature increases from 100 to 600 °C. The result was consistent with the elemental analysis in **Table 3.2**, which suggested an increasing extent of carbonization as pyrolysis reactions proceed. However, interestingly, as temperature keep increasing from 600 to 800 °C, a significant surge of oxygen content from 8.69% to 19.08%, which was not agree with the elemental analysis result. Since the XPS analysis determined surface functionalities of solid residues, the increasing O1s exhibited more oxygen-containing functional groups on the solid residue surface. Those functionalities probable obtained from the aggregation of coke due to repolymerization when pyrolysis became more moderate.

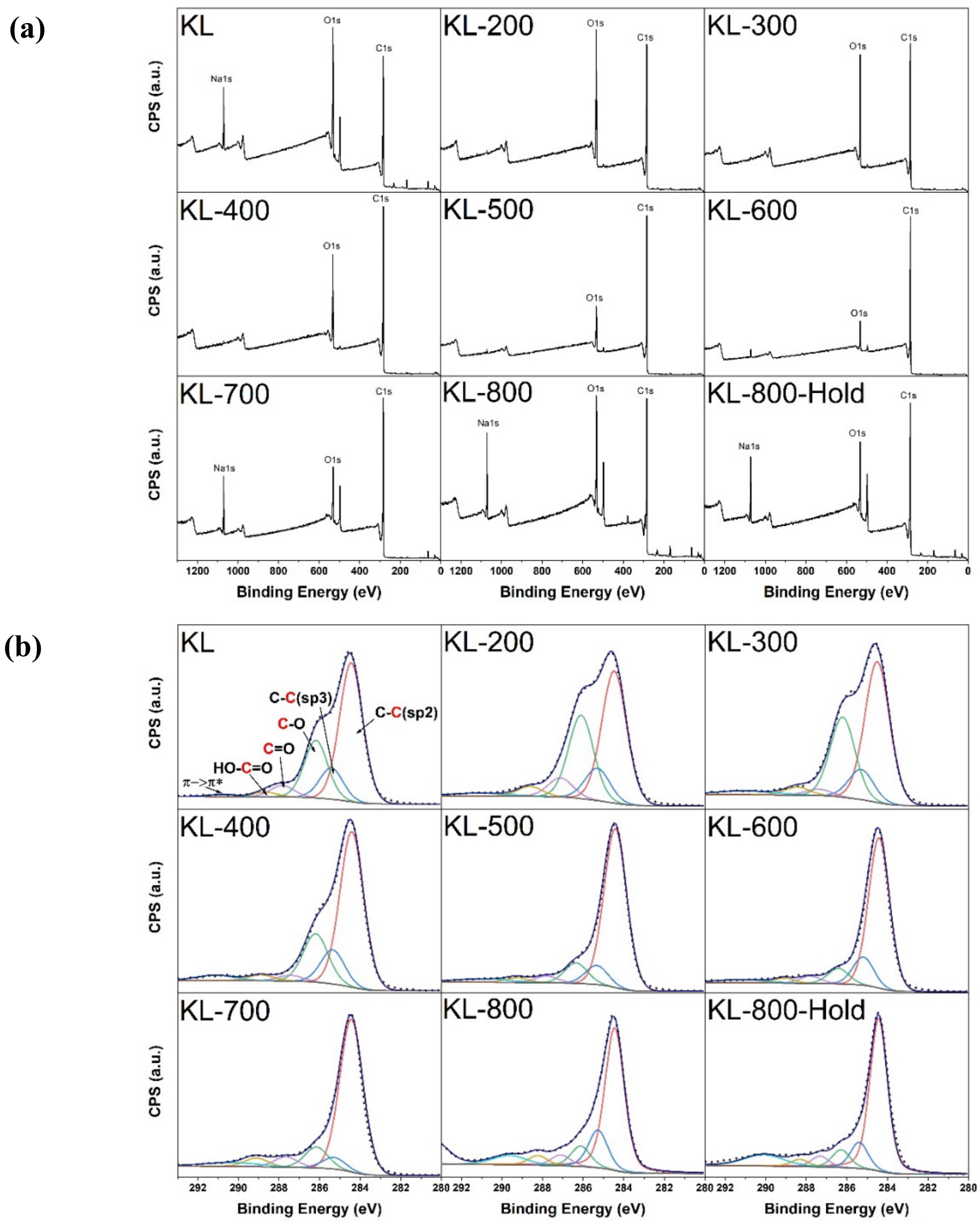

Figure 3.4 a) XPS spectrums of kraft lignin slow pyrolytic solid residue at multiple temperature regions; b) C 1s peaks of lignin slow pyrolytic solid residue at multiple temperature regions.

Table 3.4 The summary of elemental composition and chemical states in each sample based on XPS

Sample	Carbon[a] (C1s)	C-C(sp^2) [b]	C-C(sp^3) [b]	C-O[b]	C=O[b]	COOH[b]	Oxygen[a] (O1s)
KL	54.70	56	13	24	4	2	23.61
KL-200	66.41	47	12	29	7	3	21.14
KL-300	71.03	51	11	29	3	3	19.58
KL-400	74.33	59	13	20	2	2	15.76
KL-500	76.91	73	9	9	3	2	11.29
KL-600	79.69	70	13	7	3	3	8.69
KL-700	72.92	71	6	10	5	4	12.75
KL-800	63.57	60	16	8	5	4	19.08
KL-800-Hold	67.58	63	11	8	4	3	15.83

[a] atomic percentages, [b] Percentage based on C1s peak deconvolution, *KL-200 to 800 represent solid residues obtained from pyrolysis of kraft lignin under heating rate of 2 ℃/min at multiple temperature from 200 to 800 ℃; KL-800-Hold represents solid residues obtained from pyrolysis of kraft lignin under heating rate of 2 ℃/min at 800 ℃ followed by holding at 800 ℃ for 2 hours.

Hexagonal graphite (h-graphite) is the thermodynamically stable form of graphite with an ABAB stacking sequence of graphene layers. Turbostratic carbon (t-carbon) is generally considered as a variant of haphazardly crumpled h-graphite. XRD is usually applied to determine the structures of h-graphite and t-carbon [233]. XRD spectra of lignin-derived solid residues are shown in **Figure 3.5**. All three samples exhibited two broad peaks at approximately 20 and 44 degree, corresponding to the (002) and (100) planes. With the increase of pyrolysis temperature, the peak at the (002) plane declines while the (100) plane increases. The hump around 20 degree indicated an amorphous and non-graphitized property of the residue collected from pyrolysis at 300 °C, which can be explained by both incomplete oxidation and the amorphous coke on the surface layer of lignin at low temperature. The diminishing peak at (002) plane indicated larger crystallite size, namely the formation of crystalline structure as temperature increases from 300 to 800 °C [233]. The gradually increasing peak at 44 degree with the increase of pyrolysis temperature represents the increasing extent of disorder. The XRD results showed that during slow pyrolysis, the amorphous lignin were converted to biochar with a turbostratic graphite structure [234].

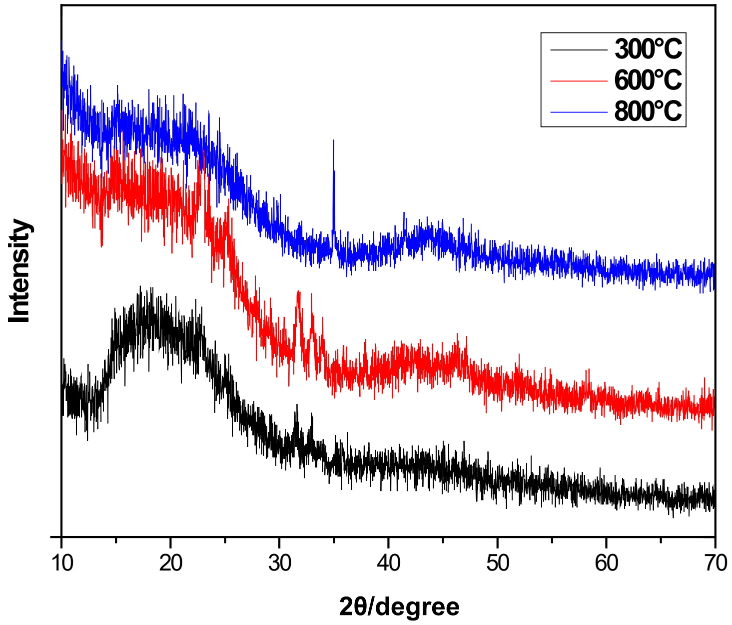

Figure 3.5 XRD spectrums of kraft lignin slow pyrolytic solid residue at multiple temperature regions.

Connecting pyrolysis chemistry with properties of the resulting carbon material

Physical and chemical properties of the resulting carbon material from lignin slow pyrolysis correlate to pyrolysis temperature and heating rate. Properties such as porosity, chemical composition and surface functional groups are critical factors for the function and performance of carbon materials. As amorphous lignin is converted to biochar with a crumpled turbostratic graphite structure, specific surface areas of the lignin-derived solid residues increase with pyrolysis temperature. Overall, the relative degree of aromaticity and polarity decreases as pyrolysis temperature increases. But, due to coke formation from repolymerization of the phenolic free radicals and PAHs, the oxygen-containing functional groups on the surface of solids increase significantly when pyrolysis temperature is higher than 600 °C. Despite the fact that limited specific surface area was obtained at relatively low pyrolysis temperature (400-500 °C), macropores formed at low temperature facilitate the access of reactants (such as SO_3H) to the active site [208]. For applications as a support of solid acid catalysts, low pyrolysis temperature is preferred since crosslinking of crumpled t-carbon at 600 °C or higher could hinder the access of reactants to active sites [235]. For applications requiring high porosity (mesopores and micropores) and specific surface area, such as supercapacitor electrode and pollutant absorbent etc., however, high pyrolysis temperature of 600-1200 °C is often preferred [44, 236]. Heating rate appears to be another important factor affecting the carbon material properties through direct impact on pyrolysis chemistry. High heating rate causes great reaction severity, in turn leading to rapid release of gases and volatiles. At low heating rate, the free radicals have better chance to self-polymerize to form PAHs and with char to form coke. The change in reaction chemistry eventually lead to change in yield and properties of the resulting carbon materials.

Conclusions

The product distribution from kraft lignin slow pyrolysis was investigated using a micropyrolyzer coupled GC-MS at various heating rates. A total of 40 GC-detectable volatiles from lignin slow pyrolysis were identified and quantified, including hydrocarbons, carbohydrates/carboxylic acids, phenolic compounds and PAHs. Vinylphenols are the primary products corresponding to cleavage of the β-*O*-4 linkages while the primary products underwent a series of secondary reactions and produce a variety of H, G and S type compounds. Solid product of lignin pyrolysis can be classified into two distinct categories, char and coke. Char derives from lignin thermochemical decomposition; while coke forms through repolymerization of free radicals and PAHs with char. With heating rate increase, the volatile yield increased while solid residues yield decreased. With pyrolysis temperature increase, specific surface areas of the lignin-derived solid residues increase. Primary ether linkages of lignin units, such as β-*O*-4, α-*O*-4 and 4-*O*-5 and side chains, such as methyl, methoxy, carboxyl and carbonyl groups decrease, which contribute to the decrease of relative degree of aromaticity and polarity as pyrolysis temperature increases. Although elemental C increases and O decreases with respect to temperature, the oxygen-containing functional groups on the surface of solids increase significantly when pyrolysis temperatures are higher than 600 °C due to coke formation from repolymerization of the phenolic free radicals and PAHs.

Acknowledgements

This work is supported by the USDA National Institute of Food and Agriculture under project accession no. 1015068 and the National Science Foundation under

Cooperative Agreements 1355438.

Electronic Supplemental Information

Understanding slow pyrolysis of lignin by linking the pyrolysis chemistry and material properties

Wenqi Li[1], Namal Wanninayake[2], Xin Gao[3], Doo Young Kim[2], Jian Shi[1, *]

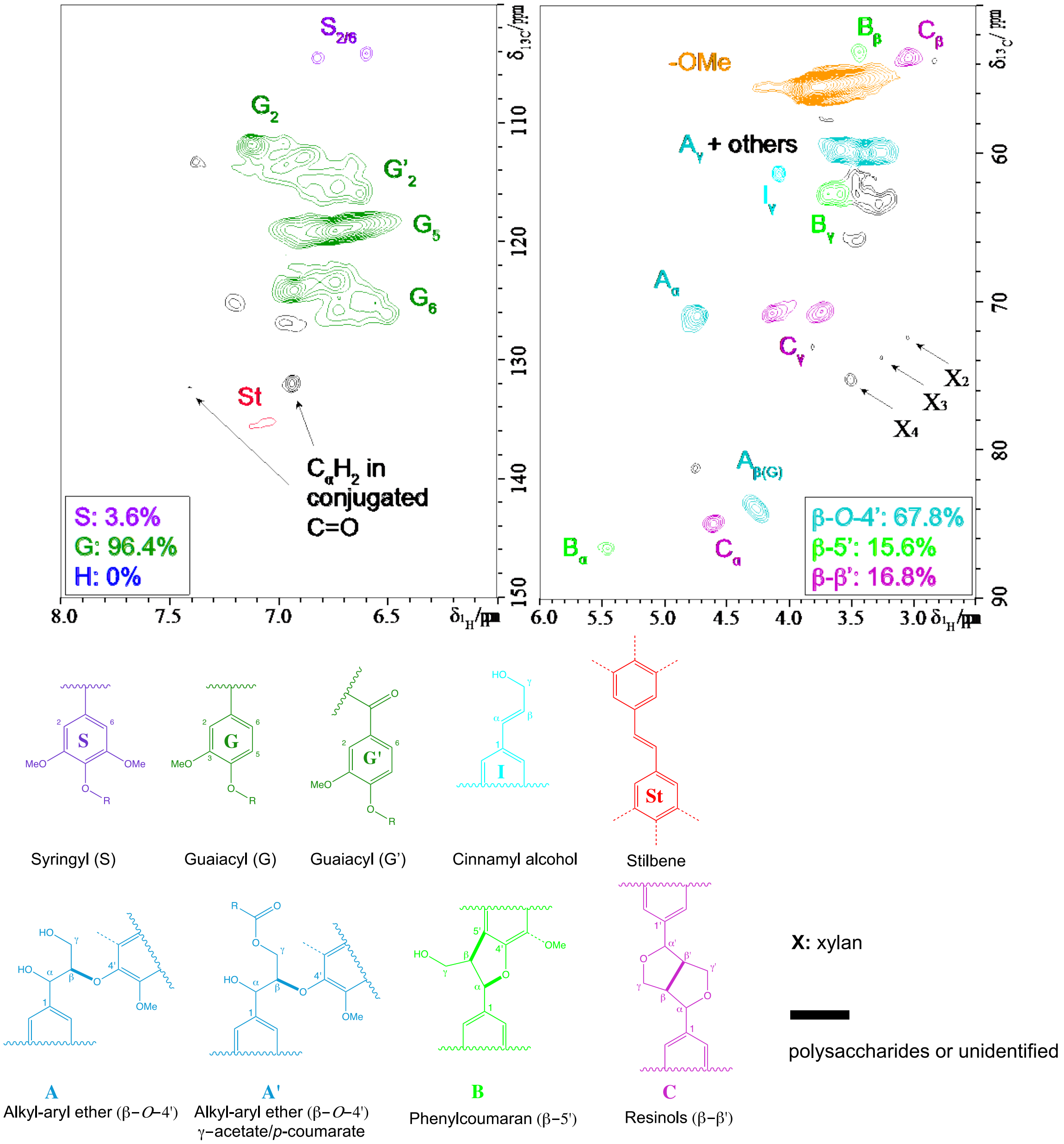

Figure 3.S1 ^{13}C-^{1}H (HSQC) spectra of aromatic (top) and aliphatic (bottom) regions of kraft lignin.

Table 3.S1 Product distribution of kraft lignin slow pyrolysis at multiple temperature regions

Compound name	2 °C / min			20 °C / min			40 °C / min		
	100-200 °C	200-300 °C	300-600 °C	100-200 °C	200-300 °C	300-600 °C	100-200 °C	200-300 °C	300-600 °C
Hydrocarbons	0.05 ± 0.06	0.48 ± 0.04	1.56 ± 0.05	0.06 ± 0.02	0.24 ± 0.04	1.50 ± 0.25	0.03 ± 0.01	0.17 ± 0.02	1.60 ± 0.15
Carbohydrates	0.63 ± 0.46	0.23 ± 0.01	0.57 ± 0.04	0.30 ± 0.28	0.95 ± 0.35	0.52 ± 0.22	0.25 ± 0.25	0.91 ± 0.49	0.45 ± 0.24
H-type substances	0.14 ± 0.02	0.22 ± 0.01	4.19 ± 0.11	0.12 ± 0.01	0.23 ± 0.06	4.10 ± 0.26	0.12 ± 0.01	0.18 ± 0.02	4.08 ± 0.28
G-type substances	0.67 ± 0.09	3.36 ± 0.13	8.02 ± 0.17	0.36 ± 0.02	1.67 ± 0.19	10.63 ± 0.38	0.28 ± 0.01	1.18 ± 0.08	11.35 ± 0.26
S-type substances	0.09 ± 0.02	0.14 ± 0.01	0.36 ± 0.02	0.06 ± 0.00	0.09 ± 0.02	0.54 ± 0.04	0.05 ± 0.00	0.07 ± 0.01	0.59 ± 0.01
PAHs	0.03 ± 0.02	0.97 ± 0.05	0.54 ± 0.02	0.00 ± 0.00	0.38 ± 0.17	1.39 ± 0.17	0.00 ± 0.00	0.29 ± 0.09	1.53 ± 0.12
Others	0.12 ± 0.03	0.40 ± 0.06	1.13 ± 0.15	0.06 ± 0.00	0.15 ± 0.03	1.37 ± 0.08	0.04 ± 0.00	0.12 ± 0.01	1.47 ± 0.06
Total volatiles yield	1.60 ± 0.68	5.38 ± 0.25	15.25 ± 0.41	0.90 ± 0.33	3.56 ± 0.84	18.66 ± 1.33	0.72 ± 0.28	2.80 ± 0.70	19.61 ± 1.07

CHAPTER 4. EFFECT OF THE STRUCTURE AND SOURCE OF LIGNIN PRECURSORS ON ACTIVATED CARBON FOR ENERGY STORAGE APPLICATION

[*] The chapter in whole has been published in *RSC Advances*.

Abstract

Valorization of lignin to high-value chemicals and products in company with biofuel production could greatly improve the economic viability of a biorefinery. With a growing demand for electrical energy storage materials, lignin-derived activated carbon (AC) materials have received increasing attention in recent years. The non-uniformity in lignin structure, composition and reactivity of linkages of diverse lignin sources could contribute to different thermochemical conversion pathway of lignin and lead to different pore structures and sizes of AC materials and thus influence the electrochemical behavior for energy storage applications, such as supercapacitors; while there is an apparent gap in our understanding of the impact of the lignin precursor on the electrochemical properties of the derived ACs. In the present study, lignin-derived ACs were prepared under identical conditions from three different lignin sources: poplar, pine, and commercial kraft lignin. Electrochemical properties and capacitance behavior of the derived ACs were examined. Results showed distinctive distributions of numerous micro-, meso- and macro-porous channels in lignin-derived ACs. The poplar lignin-derived ACs exhibited a larger BET surface area and total meso pores volume than softwood lignin-derived AC, which contribute to a larger electrochemical capacitance over a range of scan rates. X-ray photoelectron spectroscopic analysis (XPS) results revealed the presence of oxygen-containing functional groups in all lignin-derived ACs, which participated in redox reaction and thus contributed to an additional pseudo-capacitance. A possible process mechanism was also proposed to explain the effects of lignin structure and composition on lignin-derived AC pore structure during thermochemical conversion. This study provides insight into how the lignin composition and structure affect the derived ACs for energy storage

applications.

Keywords: Lignin, activated carbon, supercapacitor, biorefinery

Introduction

For the past two centuries, the extensive use of fossil fuels has brought humans to an age of unprecedented prosperity and rapid development. However, it has been a consensus that the increasing frequency of extreme weather events, environmental deterioration, climate change, etc., caused by greenhouse gas emissions, is the greatest threat humans have ever faced [237]. How we respond to these challenges will remarkably affect both current and future generations and all other creatures on earth. Biofuels provide potential and promising alternatives to traditional fossil fuels and mitigate global warming trend [188], which can be broadly categorized as first and second-generation biofuels. The first-generation biofuels are produced from starchy crops, such as corn. The second-generation biofuels utilize lignocellulose biomass, such as agriculture residue. Lignocellulosic biomass is a composite mixture of cellulose, hemicellulose and lignin, in which cellulose and a portion of the hemicellulose can be used to produce biofuels, while lignin is underutilized under current biorefinery configurations.

Lignin is the second most abundant aromatic polymer on earth [238]. As projected by the 2009 Renewable Fuel Standard (RFS2) on the basis of the Energy Independence and Security Act of 2007, the US alone will generate approximately 60 million dry tons of lignin annually as a byproduct from cellulosic biorefineries by the year 2022 [16]. This will add to the existing ~100 million tons of lignin from the paper and pulping industry [239]. Despite its great potential as a feedstock for a variety of high-value chemicals and materials, lignin valorization is challenging, due to the complex structure and compositional heterogeneity of lignin [16]. Today, lignin is usually burnt for heat and power, which inevitably generates persistent particle and organic pollutants and causes environmental issues [240]. Therefore, other options are needed to unlock the full potential of lignin [16]. Utilization of lignin or lignin-derived materials as an electrochemical electrode is well-suited to meet demands of the fast-growing energy storage market, such as batteries and supercapacitors [241].

A supercapacitor, also known as electrical double layer capacitor (EDLC), is a power energy storage device. Compared to batteries, supercapacitors have high power density and long lifespan, which are suitable for short-term energy storage and burst power delivery. They are capable of bridging the gap between traditional dielectric capacitors and batteries or fuel cells [242]. Porous carbon materials, which have high surface areas for charge storage, are the most popular electrode materials for supercapacitors [243]. Lignin has been considered as a preferred precursor for activated carbon materials because of its high carbon content, highly branched and cross-linked structure, and low feedstock cost. Despite many publications on lignin-derived activated carbon materials for supercapacitor applications, the results reported by different groups vary significantly, as shown in **Table 4.1**. In addition to inconsistent processing conditions, the heterogeneity in structure and composition of lignin precursors will contribute to the discrepancy in the supercapacitance performances.

Properties of lignin, including composition, structure and reactivity, vary significantly depending on the source of biomass feedstocks. Lignin is composed of three major monomer units, namely guaiacyl (G), syringyl (S), and p-hydroxyphenyl (H) [244].

Different types of biomass would have different specific ratios of G/S/H. For instance, softwood is composed of nearly 100% G lignin, while hardwood contains approximately equal percentages of G and S lignins [12]. The high ratio of S-units impedes the formation of β-5’and/or 5-5 linkages among lignin monomers (i.e., fewer branches) due to structural hindrance. As a result, hardwood lignin has more linear polymer chains than softwood lignin [245]. The softwood lignins with relatively high numbers of C-C linkages compared to ether linkages are often referred to as condensed lignins. Condensed lignins are typically more rigid and less prone to degradation, since the bond dissociation energy [246] required to break C-C linkages such as β-5’ is higher than that to break ether linkages such as β-*O*-4 [247]. Furthermore, the chemical reactivities of lignin linkages are different. It was found that the cleavage of β-*O*-4 linkage within H and S lignin was easier than G lignin; while the reactivities (as calculated by electrophilicity) of the linkages between H and S unit are higher than those of G lignin [248].

In addition to the lignin sources, biomass pretreatment, during which lignin was fractionated from biomass feedstocks, influences the properties of the extracted lignin. A number of pretreatment methods have been developed, such as acids, alkali, organic solvents, and ionic liquids, all proven to overcome or reduce the natural recalcitrance of lignocellulosic biomass thus improving sugar yield from enzymatic hydrolysis. Due to the differences in pretreatment chemistry and processing condition, various pretreatment approaches remarkably affect the structure and composition properties of the extracted lignin. Acid pretreatment method will generally eliminate hemicellulose, while leaving cellulose fraction unaffected. Although little lignin is dissolved, the rearrangement of the lignin structure has been suggested with dilute acid pretreatment [15]. Alkaline-based pretreatments, which include ammonia and lime pretreatment, can effectively remove lignin in biomass by hydrolyzing the ether bonds [249]. Compared to NaOH, the lignin isolated from ammonia pretreatment has led to a lower oxygen and higher aromatic content [250]. The organosolv pretreatment removes and modifies lignin via organic solvents, such as methanol, ethanol and acetone, with either acid or base catalysts. The organosolv pretreatment resulted in a significant deconstruction of lignin by the cleavage of inter-unit linkages and condensation of S and G units in comparison with dilute acid and ammonia pretreatment [17]. During organosolv pretreatment, *Liriodendron tulipifera* lignins were isolated, migrated and redistributed and the structural reformed droplets were found on the surface of pretreated biomass [251].

Based on the above discussion, there is a gap in our understanding of the determining factors of lignin source, structure and composition on the electrochemical properties of the derived activated carbons. The non-uniformity in lignin structure, composition and reactivity of linkages of diverse lignin sources could lead to different activated carbon materials and thus influence the supercapacitor behavior. In the present study, lignin-derived activated carbon (AC) materials were prepared under identical conditions from three different lignin sources: poplar, pine, and commercial kraft lignin. Electrochemical properties and capacitance behavior of the derived ACs were examined for supercapacitor application to better understand the impact of lignin source. A possible process mechanism was also proposed to explain the effects of lignin structure and composition on lignin-derived AC pore structure during thermochemical conversion.

Table 4.1 Supercapacitor performance of various lignin-derived carbons reported in the representative literatures

Feedstock	Target materials	Carbonization	Activation	SSA (m^2/g)	Electrolyte	Capacitance (F/g)	Reference
Kraft lignin	AC	Pyrolysis (1000 °C, 15 min)	KOH (1000 °C, 35 min)	1148	6 M KOH	91.7 @ 2 mV/s	Saha et al., 2014[71]
Hardwood lignin	AC	Pyrolysis	KOH (700 °C, 2h)	907	1 M H_2SO_4	165@ 50 mV/s	Zhang et al., 2015[77]
Corn stover lignin	AC	Hydrothermal (180 °C, 18h)	KOH (800 °C, 3h)	1660	6 M KOH	420 @ 0.1 A/g	Guo et al., 2017[79]
Alkali lignin	ACF		KOH (850 °C, 0.5h)		6 M KOH	344 @ 10 mV/s	Hu et al., 2014[89]
Poplar lignin	AC	Hydrothermal (200 °C, 24h)	KOH (800 °C, 1h)	2218	6 M KOH	312 @ 1 A/g	Zhang et al., 2016[91]
Acid washed lignin	AC	Pyrolysis (900 °C, 15 min)	Template	803	6 M KOH	152.5 @ 1 mV/s	Li et al., 2016[84]
Black liquor lignin	AC	Pyrolysis (900 °C, 2h)	KOH (900 °C, 2h)	1406	1.5 M NEt_4BF_4/ACN	87 @ 5 mV/s	Adriana et al., 2014[80]
Alkali lignin	AC	Pyrolysis (500 °C, 1h)	KOH (800 °C, 1h)	3775	6 M KOH	286.7 @ 0.2 A/g	Zhang et al., 2015[81]
Alkali lignin	ECNF mats	Pyrolysis (1200, 1h)		583	6 M KOH	64 @ 0.4 A/g	Lai et al., 2014[88]
Kraft lignin, ethanol extracted lignin, alkali lignin	AC			1092, 519, 126	1 M H_2SO_4	91, 35, 53 @ 0.5 A/g	Jeon et al., 2015 [82]
Softwood kraft lignin	AC		KOH (800 °C, 1h)	1800	EMIBF4	200 @ 10 A/g	Klose et al., 2017 [83]

Experimental Section

Materials

All biomass feedstocks, including hybrid poplar and lodge pole pine, were obtained from the Idaho National Laboratory. The raw biomass was grounded by a Thomas Model 4 Wiley® Mill (Thomas Scientific, NJ, USA) to 1 mm particles. Then the grounded biomass was sieved via a Ro-Tap® testing sieve shaker (Model B, W. S. Tyler Industrial Group, Mentor, OH, USA) to acquire a particle size range of 0.25 to 0.425 mm for lignin isolation. Kraft lignin and KOH were purchased from Sigma-Aldrich (St. Louis, MO, USA); while NaOH and HCl were purchased from Fisher Scientific (City, State, USA). Hemicellulase enzyme mixture Cellic HTec2 was provided by Novozymes North America (Franklinton, NC, USA).

Lignin isolation

Biomass samples were pretreated in NaOH at 140 °C for 60 min in a 500 ml Parr reactor. Specifically, 40 g of biomass was mixed with 360 ml of 2 wt. % NaOH to obtain a 10 wt.% biomass loading. A 300 mesh nylon filter was used to separate the solid and liquid phases in the pretreated biomass slurry. The solid fraction was kept and stored at 4 °C for composition analysis. Lignin was precipitated from the liquid fraction by adjusting the pH value to 1.5 – 2.0 with 1M HCl. The recovered lignin was washed 4 times with hot water to reach neutral pH. To remove carbohydrate impurities from isolated lignin, a dose of hemicellulose enzymes (Cellic HTec2 loading of 0.34 mg protein / g starting biomass) was added to the recovered lignin and incubated at 50 °C in a pH 4.8, 0.05 M citrate buffer solution for 72 hours on an orbital shaker (Forma 435, Thermo Fisher Scientific Inc., Waltham, MA, USA). The purified lignin was washed 4 times with 35 ml of hot DI water and then freeze-dried (Freezone Model 77530, Labconco, Kansas City, MO, USA) and collected for carbonization.

Preparation of mesoporous activated carbons

Lignin derived activated carbon was prepared in an alumina crucible for carbonization in a tube furnace (GSL-1500X-OTF, MTI Corporation, Richmond, CA, USA). The lignin sample was heated under an argon environment from room temperature to 700 °C ramping at 2 °C / min and held for 1 hour at 700 °C before cooling down to room temperature. Then the collected biochar was activated in a KOH agent. Typically, biochar was dispersed in the KOH solution with a biochar to KOH mass ratio of 1:3 to form a slurry. The slurry was placed on a hot plate at 80 °C and was stirred by a magnetic stirrer during drying. The dried biochar KOH composite was transferred to a crucible and put into a tube furnace for activation. The furnace temperature was set to 700 °C and held for 1 hour. After activation, the activated carbon was neutralized with 0.1 M HCl and then washed with deionized water until its pH becomes 7.0. Finally, the activated carbon was collected and dried in a convection oven (Heratherm, Fisher Scientific Inc., Waltham, MA, USA) at 80 °C.

Lignin characterization

Fourier Transfer Infrared Spectrometry (FTIR):

FTIR characterization was carried out with a Thermo Nicolet Nexus 870 ESP ATR-FTIR spectrometer (Thermo Fisher Scientific Inc., Waltham, MA, US). For the measurement, lignin samples (around 5 mg) were pressed to 12 psi using a spring loading jack onto the ATR crystal. FTIR spectra were acquired in the range between 400 and 4000 cm^{-1} with a spectral resolution of 1.928 cm^{-1}. The raw FTIR spectra were baseline corrected and normalized using the Omnic 6.1a software and compared in the range of 700-2000 cm^{-1}.

Gel Permeation Chromatography (GPC):

For molecular weight measurement, lignin samples were treated by the acetylation method [252]. Typically, 10 mg of isolated lignin was dissolved in 2.5 ml 92:8 (v/v) anhydrous acetic acid and acetyl bromide mixture and stirred at 50 °C for 2 h. The acetic acid and excess acetyl bromide solvent were dried in N_2. The acetylated lignin was immediately dissolved in tetrahydrofuran (THF). The molecular weight distribution of the lignin samples was determined by an HPLC system (Ultimate 3000, Dionex Corporation, Sunnyvale, CA, USA) equipped with an ultraviolet detector and an Agilent Mixed-D PLgel 5 μm 300 × 7.5 mm column (Agilent Technologies, Santa Clara, CA, USA) using THF as mobile phase at a flow rate of 0.5 ml/min. The materials eluting from the column was monitored by recording absorbance at 290 nm. The chromatography was calibrated using low molecular weight polystyrene standards (Product No. 48937, Sigma-Aldrich).

Lignin composition analysis:

The percentage of structural carbohydrates (glucan and xylan) and lignin, including both acid-soluble lignin and acid insoluble lignin, was determined in duplicates according to a NREL laboratory analytical procedure [179]. After two-stage acid hydrolysis, monomeric sugars were measured by HPLC (Ultimate 3000, Dionex Corporation, Sunnyvale, CA, USA) via a refractive index detector and an Aminex HPX-87H column and guard column assembly. A 5mM H_2SO_4 was served as the mobile phase at a flow rate of 0.4 ml/min with a column temperature set at 50 °C. The quantity of acid soluble lignin was determined by the absorbance at 205 nm.

NMR spectroscopic analysis:

Nuclear magnetic resonance (NMR) spectra of lignin samples were acquired in a Bruker Avance III HD 500-MHz spectrometer and spectral processing was carried out using a Bruker Topspin 3.5 (Mac) software. Isolated lignins (~10 mg) were dissolved in 110 mg DMSO-d_6 in a micro-NMR tube independently. Heteronuclear single quantum coherence (HSQC) experiments were carried out with a Bruker pulse sequence (hsqcetgpspsi2.2) on a N_2 cryoprobe (BBO 1H & 19F-5mm) with the following acquisition parameters: spectra width 12 ppm in F2 (^{1}H) dimension with 1024 data points (acquisition time 85.2 ms), 166 ppm in F1 (^{13}C) dimension with 256 increments (acquisition time 6.1 ms), a 1.0-s delay, a $^1J_{C–H}$ of 145 Hz, and 128 scans. The central DMSO-d_6 solvent peak (δ_C/δ_H at 39.5/2.49) was used for chemical shifts calibration. Assignment and the relative abundance of lignin compositional subunits and interunit linkages were estimated using volume integration of contours in HSQC spectra according to published literature [183, 185]. For volume integration of monolignol compositions of syringyl (S), guaiacyl (G), and *p*-hydroxyphenyl (H), the cross peaks of $S_{2/6}$, G_2, and $H_{2/6}$ contours were used with G_2 integrals doubled. In poplar lignin, *p*-hydroxybenzoate [253] with the cross peaks of $PB_{2/6}$ was used for integration and quantitation. The C_α signals were used for volume integration for inter-unit linkages estimation. The abundances of aromatics and side-chain linkages were presented as percentage of total aromatic SGH units.

Physical and chemical properties characterization

Brunauer-Emmett-Teller (BET):

BET surface area was determined using a Micromeritics TRISTAR 3000 gas adsorption analyzer (Micromeritics Instruments, Norcross, GA, USA). In each test, approximately 100 mg of sample was used. The adsorption gas was nitrogen and the analysis was performed at the boiling temperature of liquid nitrogen. Samples were degassed under vacuum at 160°C overnight before conducting the BET measurements to obtain the specific surface areas. The Horvaih-Kawazoe (HK) method was used to analyze the pore size distribution of micropores, and the Barrett-Joyner-Halenda (BJH) method was used to analyze the pore size distribution of mesopores.

Microscopic and spectrometric analysis:

Scanning electron microscopy (SEM) images of lignin, biochar, and activated carbon materials were taken in a FEI Quanta SEM system (Thermo Fisher Scientific Inc., Waltham, MA, US). X-ray diffraction (XRD) spectra of activated carbon materials were obtained using a Bruker-AXS D8 Diffractometer (Bruker Corporation, Billerica, MA, US) with Cu Kα radiation (Kα = 0.15405 nm), scanning rate of 1.0° / min, and voltage of 40 kV and current of 200 mA. X-ray photoelectron spectroscopy (K-Alpha XPS, Thermo Fisher Scientific Inc., Waltham, MA, US) was used to determine the surface functional groups of lignin derived carbon materials.

Electrochemical properties characterization

Electrochemical characterization of all lignin-derived carbon materials carried out using a three-electrode system. A platinum wire was used as the counter electrode, a commercial Ag/AgCl electrode as the reference electrode, and the lignin-derived carbon as the working electrode. The electrolyte was 1 M H_2SO_4 in an aqueous solution. Cyclic voltammetry (CV), galvanostatic charge-discharge (GCD), and electrochemical impedance spectroscopy (EIS) were recorded with a potentiostat (CHI 760, CH Instruments, Austin, TX, US).

Results and Discussion

Lignin isolation and characterization

Alkaline treatment using dilute NaOH or lime is a common biomass delignification method [254]. During an alkaline treatment process, the ester bonds between lignin and xylan are typically cleaved along with the breakdown of the β-O-4 lignin interunit linkages, leading to dissollution of lignin fragments in the liquid phase and generation of a cellulose and hemicullose enriched solid suitable for biofuel production [152]. The dissolved lignin can then be precipitated from the alkaline solution by adjusting the pH to acidic. Since hemicellulose will bind and precipitate with lignin, the main impurities of the isolated lignin are the 5-carbon sugars. To remove xylan, the pretreated lignin samples were subject to enzymatic hydrolysis [180]. The purities of pine, poplar, and Kraft lignin samples were determined using the two-step acid hydrolysis procedure [179]. As shown in **Table 4.2**, most of xylan was eliminated and high purity lignin (94-98%) was acquired after enzymatic saccharification. The ash content is the measure of the mineral content and other inorganic matter in biomasses [255], and the isolated lignin also contains a small amounts of ash, depending on the biomass feedstock, pretreatment, and isolation method used [120]. As compared to Kraft lignin, isolated lignin samples exhibited the lower content of ash. The low ash content of the isolated lignins, shown in **Table 4.2**, may be attributed to the acid adjustment, enzymatic hydrolysis and multiple hot water washing, which removed most of ash within lignin.

Table 4.2 Composition and GPC analysis of Kraft lignin and lignins extracted from poplar and pine.

Lignin sources	Glucan	Xylan	Purity (%)	Ash (%)	Mw (Da)	Mn (Da)	PDI
Kraft lignin	0.11 ± 0.01	0.96 ± 0.03	95.99 ± 0.03	2.95 ± 0.01	5736.11	3056.34	1.88
Pine lignin	0.76 ± 0.05	1.18 ± 0.02	97.56 ± 0.08	0.50 ± 0.05	2847.73	1671.53	1.70
Poplar lignin	1.08 ± 0.01	4.95 ± 0.08	93.78 ± 0.13	0.19 ± 0.05	2799.78	1656.28	1.69

The weight average molecular weight [175], number average molecular weight (Mn) and polydispersity index (PDI) of pine, poplar, and Kraft lignin are shown in **Table 4.2**. The Mw of pine and poplar were 2847.73 and 2799.78 Dalton, respectively, which are much lower than the Mw of Kraft lignin. The lower molecular weight might result from the depolymerization of native plant lignin during alkaline pretreatment [91]. The PDI value was acquired from the ratio of Mw/Mn, which represents the heterogeneity of the size distribution of the isolated lignin samples. The PDI values were below 2 for both poplar and pine derived lignin samples, which is slightly lower than that of Kraft lignin, indicating increased uniformity of molecular weight distribution.

FT-IR spectra of the three lignin are shown in **Figure S1**. All lignin samples exhibited a broad absorption band at 3400 cm^{-1}, which corresponds to the O-H stretching vibrations in phenolic and aliphatic O-H groups [170]. The bands between 2920 and 2840 cm^{-1} represent C-H vibrations of CH_2 and CH_3 groups [256]. All lignin samples have a peak at 1740 cm^{-1}, representing a stretching of carbonyl groups (C=O) in carboxylic acid or ester group [257]. The bands at 1600 cm^{-1} and 1510 cm^{-1} are attributed to aromatic ring stretch vibrations (C=C) [173]. The broad bands ranged from 1470 to 1330 cm^{-1} are assigned to C-H aromatic ring vibrations and the deformation vibration of O-H in CH_2 and CH_3 groups [173]. The bands at 1220, 1110 cm^{-1} are believed to associated with guaiacyl (G) and syringyl (S) units of lignin respectively [173, 174]. Compared to poplar lignin, pine lignin has an intense peak at the band of 1220 cm^{-1}, indicating C-C, C-O, and C=O stretching (G), at expense of a moderate peak at the band of 1110 cm^{-1}, corresponding to aromatic C-H in plane deformation (S), which agrees with an earlier report [12].

To examine the lignin chemistry and chemical structure change of lignins through alkaline pretreatment, 2D ^{13}C-^{1}H HSQC NMR was applied to characterize the pine and poplar extracted lignins. The spectra of the aromatic region between 6.0-8.0/100-150 ppm of the lignins, revealing the lignin structural subunits, were shown in **Figure 4.S2**. 2D NMR spectra of aromatic regions revealed that both extracted lignins are SGH type lignin. On a basis of total SGH amount, pine lignin was absolutely dominated by G unit, while poplar was composed of S and G unit. The aliphatic region between 2.5-6.0/50-90 ppm of the lignins, revealing the lignin inter-units and side chains, can be seen in the **Figure 4.S3**. Both pine and poplar lignins were found to be dominated by β-*O*-4' accompanying with a small amount of β-5' and β-β' linkages. The HSQC NMR data acquired from extracted lignin were in agreement with their untreated native structure [12], indicating the original structural subunits and side chains of the extracted lignins were not significantly transformed during alkaline pretreatment. Furthermore, the poplar lignin contained more oxygen-containing functionalities than pine due to significantly higher S-unit, which contributed to more pore structures after carbonization, and thus result in a higher capacitance.

Lignin carbonization and biochar activation

The weight loss of lignin samples after carbonization is attributed to the loss of moisture, CO, CO_2, methane, and phenolic volatiles depolymerized during pyrolysis [167]. The reaction between carbon and KOH and a series of intermediate products contribute to the weight loss during the activation process[34]. The mass yield during carbonization and activation is summarized in **Table 4.S1** [258]. For the 100 g of lignin sample, pine and poplar lignin yielded 41.3 g and 29.4 g of biochar, respectively, although their yields of activated carbon yield are similar, 22.2 g for pine lignin and 23.2 g for poplar. It is possible that pine lignin requires a more severe condition to reach full carbonization than poplar lignin as the result of different inter-lignin linkages for pine and poplar. Softwood lignin is predominately made of G lignin, while hardwood lignin contains an equal amount of both G and S lignin. The less amount of methoxy group in softwood lignin favors a highly branched and condensed structure [259], and thus has more C-C bond and less ether bond than hardwood lignin. Since C-C bond has stronger bond dissociation energy than ether bond, softwood lignin requires more energy to be carbonized. On the other hand, more methoxy groups mean higher oxygen content in lignin. Oxygen will be eliminated during carbonization and leave many active sites ready to be activated.

The pine lignin contains over two times as many G-lignin unit as the poplar lignin [12]. Since the reactivity of the linkage between H and S unit is stronger than G lignin, the reaction rate for poplar lignin is much higher than pine lignin [248]. The biochar may significantly affect subsequent activation due to fewer active sites generated during carbonization which can affect pore structure and specific surface area (SSA) that are of an importance for supercapacitor performance.

Since more branched hardwood lignin resulted from high S/G ratio it is easier to generate a less dense network in comparison with softwood, which favors the formation of the 3-dimensional structure after carbonization and activation[17].

Morphology, pore structure of carbon materials

Figure 4.1 shows the SEM images of the pine, poplar and Kraft lignins, the carbonized biochar and the KOH activated carbon from those lignin samples. As can be seen in **Figure 4.1a-c**, the raw lignin samples are 20-40 μm particles with high surface roughness. During pyrolysis, lignin starts to melt at approximately 200 ºC [260]; from that moment, melting and crosslinking between lignin particles occur simultaneously, forming a 3-dimentional biochar structure after carbonization, as shown in **Figure 4.1d-f**. KOH chemical activation of these biochars resulted in the lignin-derived activated carbon (AC) samples. These AC samples exhibited a 3D structure with a large number of pores in different sizes, as shown in **Figure 4.1g-i**. The pores connected through channels have important roles in promoting electrode surface areas available for the adsorption of ions and electrolytes and thus enhancing electrochemical capacitance in the supercapacitors.

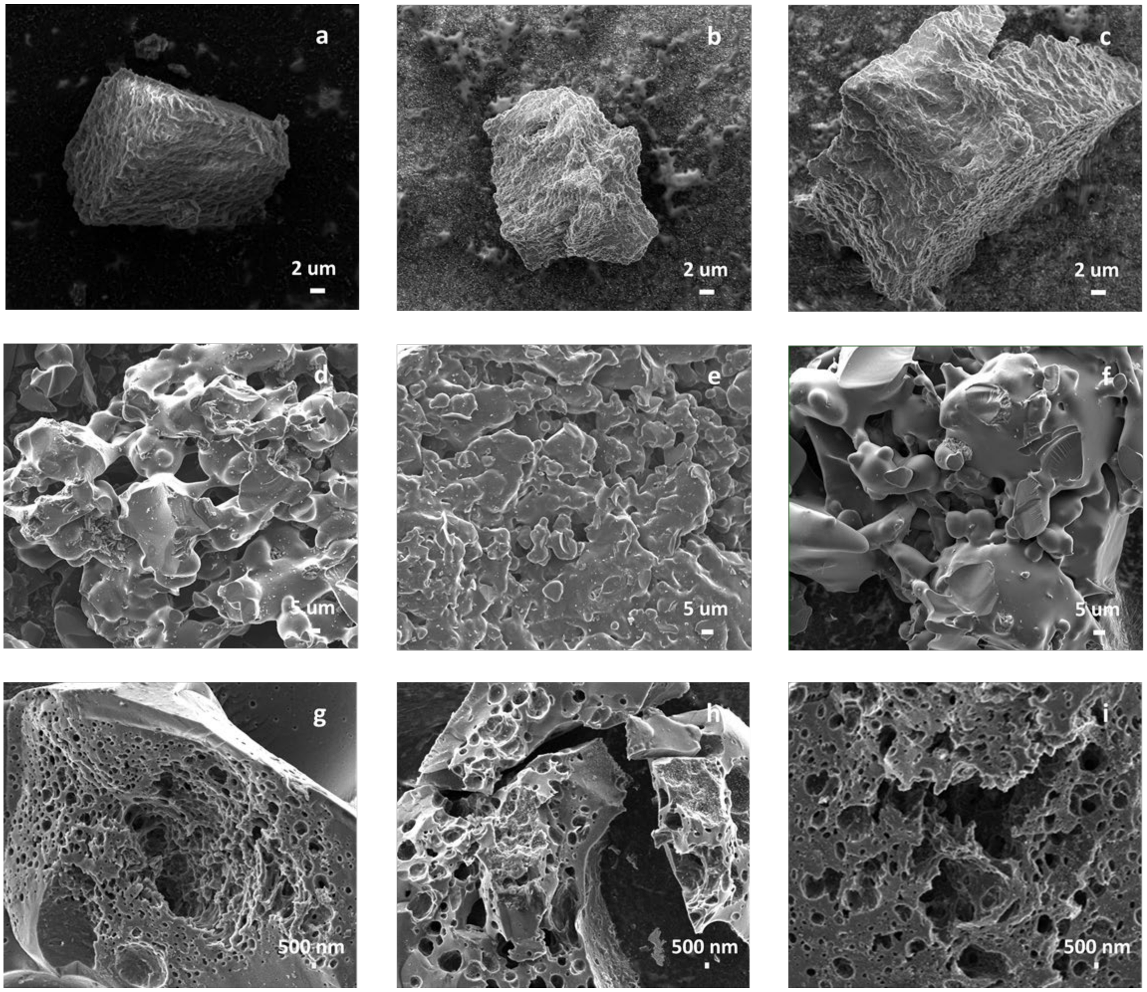

Figure 4.1 SEM images of lignin, biochar and activated carbon samples: a) Kraft lignin, b) Pine lignin, c) Poplar lignin, d) Kraft lignin-derived biochar, e) Pine lignin-derived biochar, f) Poplar lignin-derived biochar, g) Kraft lignin-derived activated carbon (AC), h) Pine lignin-derived AC, i) Poplar lignin-derived AC.

XRD spectra of lignin-derived ACs are shown in **Figure 4.S4**. All three lignin-derived ACs exhibited similar features with two broad peaks at approximately 20 and 40 degree, which correspond to (002) and (100) crystalline planes of graphite. The XRD results show that the derived ACs have a turbostratic structure (between graphite and amorphous carbon) [234].

To examine the pore structure of lignin-derived ACs, the BET specific surface areas and pore size distributions were determined by N_2 adsorption and desorption analyses. The adsorption isotherm plots are shown in **Figure 4.2a**. All ACs revealed the mixed character of types I and IV. Such a behavior reflects the coexistence of micropores, mesopores, and macropores [77, 81]. However, the pine lignin-derived AC represented a very low N_2 adsorption volume and a flat adsorption curve, indicating the low content of porosity.

Table 4.3 Pore parameters of pine, poplar and Kraft lignin-derived activated carbons

Lignin	S_{BET} (m^2/g)	V_{micro} (cm^3/g)	V_{meso} (cm^3/g)	V_{total} (cm^3/g)	V_{meso}/V_{micro} (%)
Kraft	981.38	0.38	0.07	0.45	19.7
Pine	314.95	0.12	0.02	0.14	20.6
Poplar	621.25	0.18	0.08	0.27	46.0

BET specific surface area (SSA) and the volume of micropores and mesopores of the lignin-derived ACs were shown in **Table 4.3**. Compared with the low SSA of 314.95 m^2/g for pine derived lignin-derived AC, poplar and Kraft lignin derived lignin-derived ACs had much higher SSA of 621.25 and 981.38 m^2/g, respectively. The high SSA of Kraft lignin-derived AC mainly benefited from its significantly large micropores volume of 0.38 cm^3/g. In contrast, poplar lignin-derived AC had relatively lower micropores volume as compared with its mesopore volume, likely attributing to the structurally fragmented lignin when going through alkali extraction and reprecipitation. In addition to lower SSA_{BET}, mesopore volume of pine lignin-derived AC was also significantly lower than that of the poplar and Kraft lignin-derived ACs. Although the total pore volume of poplar lignin-derived AC was lower than Kraft lignin-derived AC, it exhibited a larger mesopore volume and in turn a very high mesopore ratio of 46%. The pore size distribution, which was calculated by BHJ method, is shown in **Figure 4.2b**. The results of SSA and pore size distribution further illustrate that the source lignin structure, composition, and linkage reactivity greatly influence the porosity and structure of lignin-derived ACs.

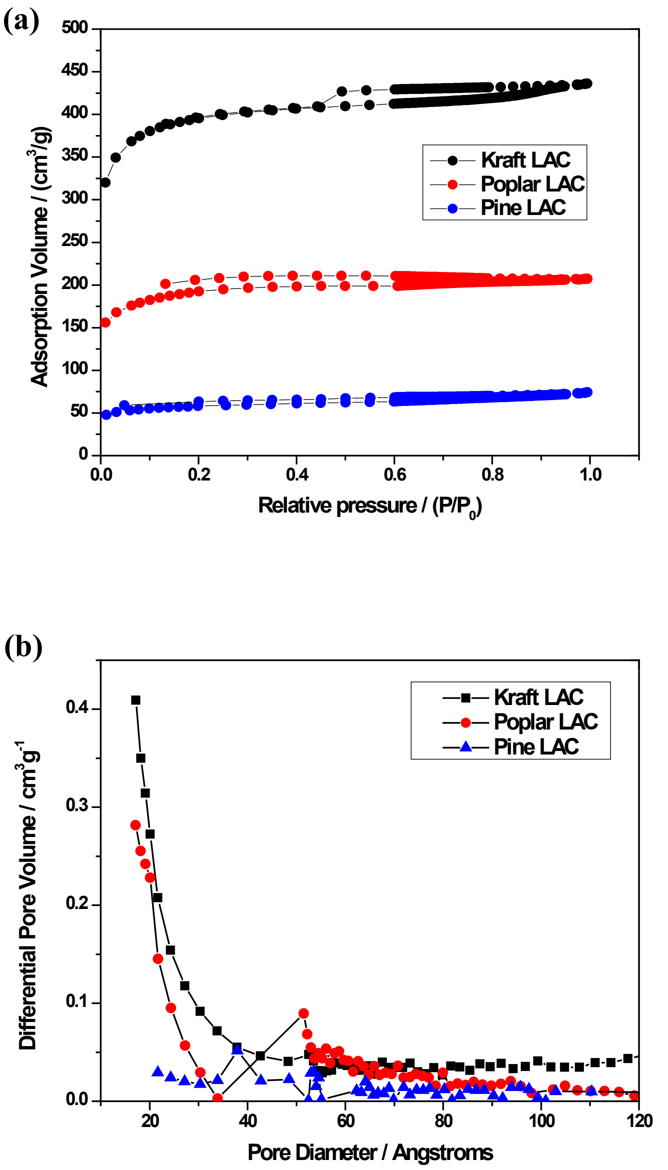

Figure 4.2 a) N_2 adsorption-desorption isotherms and b) calculated pore size distribution of pine, poplar and Kraft lignin derived activated carbons (LAC).

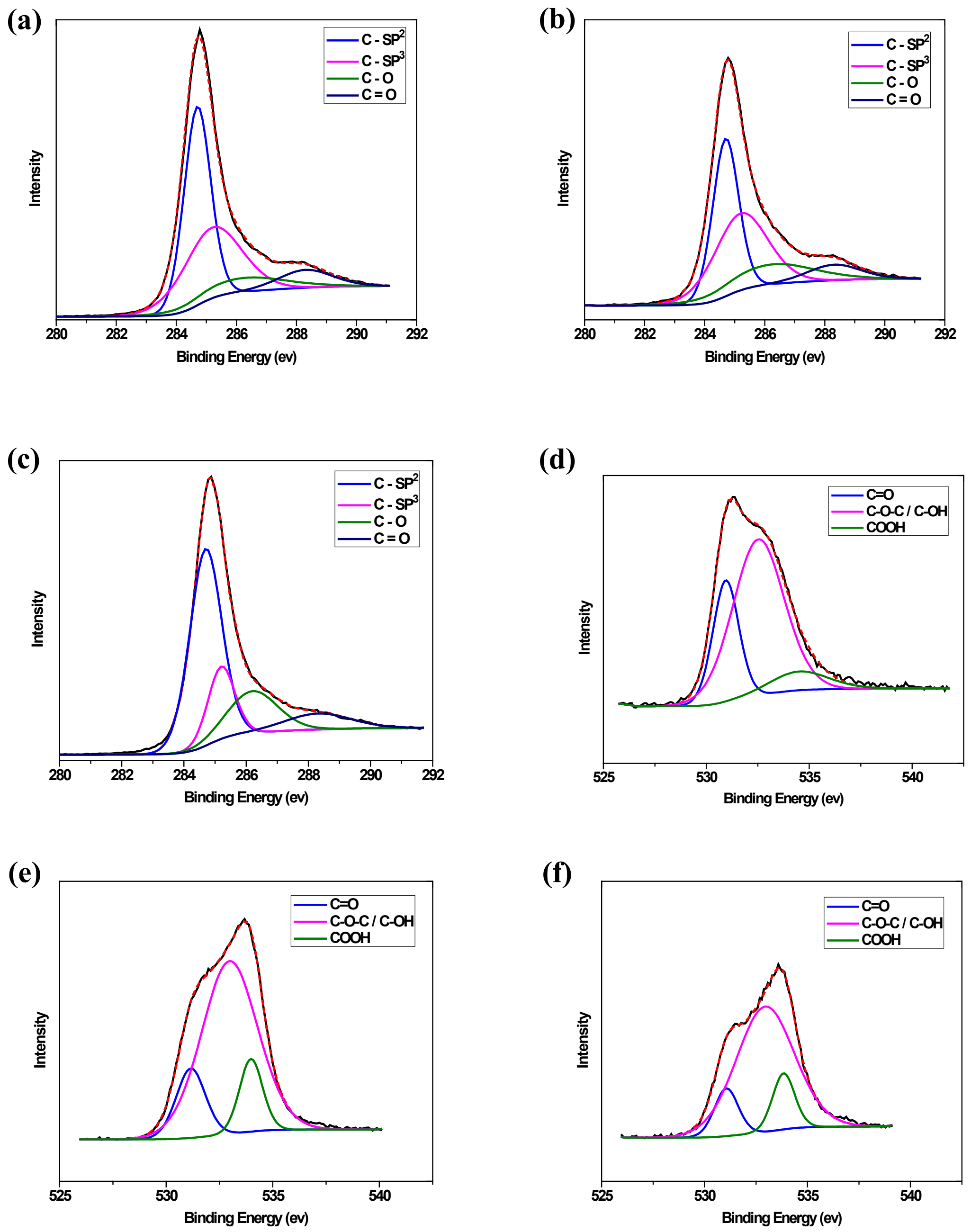

Figure 4.3 Fitted results of XPS spectra: a) C1s of Kraft; b) C1s of poplar; c) C1s of pine; d) O1s of Kraft; e) O1s of poplar; f) O1s of pine lignin-derived ACs.

Surface chemistry property of carbon materials

X-ray photoelectron spectroscopy (XPS) was applied to analyze the surface chemistry of the lignin-derived ACs. The high resolution XPS C1s and O1s spectra of the lignin-derived ACs are shown in **Figure 4.3**. The deconvolution of the original C1s peaks revealed four individual component peaks at 284.7, 285.2, 286.2 and 288.3 eV including C-sp2, C-sp3, C-O and C=O, respectively. The O1s XPS spectrum exhibits three individual peaks representing quinone or keto groups (531.1 eV), ether or phenol groups (532.9 eV), carboxylic groups (534.0 eV) [77, 79, 261]. The content of each functional group in the AC samples are summarized in **Table 4.4**. Compared to pine lignin-derived AC of 7.6 atom % surface oxygen content, both Kraft and poplar lignin-derived ACs had higher surface oxygen content as indicated by the atomic percentage of 10.7% and 11.5%, respectively. The higher surface oxygen contents of Kraft and poplar lignin-derived ACs are likely caused by the greater extent of activation occurring during carbonization and KOH activation processes than pine lignin-derived AC [77]. Oxygen–containing functional groups can improve hydrophilicity and provide an additional pseudocapacitive current through reversible faradaic reactions [79].

Table 4.4 Oxygen-containing functional group comparison between pine, poplar and Kraft lignin-derived activated carbons

Lignin	**C=O**	**-O-**	**COOH**
Kraft (10.7 at %)	2.76	6.98	0.96
Pine (7.6 at %)	0.90	5.73	0.98
Poplar (11.5 at %)	1.74	8.31	1.45

Electrochemical characterization

The electrochemical behaviors of the lignin-derived ACs were examined in a single-compartment electrochemical cell in the potential window from -0.6 to 0.6V in 1 M H_2SO_4. The cyclic voltammetry (CV) curves are shown in **Figure 4.4a-c**. The quasi-rectangular shape CV curves, representing a double layer capacitor character, were observed for all the lignin-derived ACs. In addition, peaks at 0.2 to 0.4 V indicated pseudo-capacitance, which was caused by redox reactions of surface oxygen containing functional groups as depicted by the XPS results (**Table 4.4**) [77]. The specific capacitances of the lignin-derived ACs were determined at different sweep rates from CV curves as shown in **Figure 4.4d**. Compared with pine, poplar lignin-derived AC showed a better current response at each scan rate, which is attributed to the significantly larger SSA and mesopore volume. With high micropore volume and SSA, Kraft lignin-derived AC showed a better capacitive performance than poplar lignin-derived AC though the latter had a larger mesopore volume than Kraft lignin-derived AC.

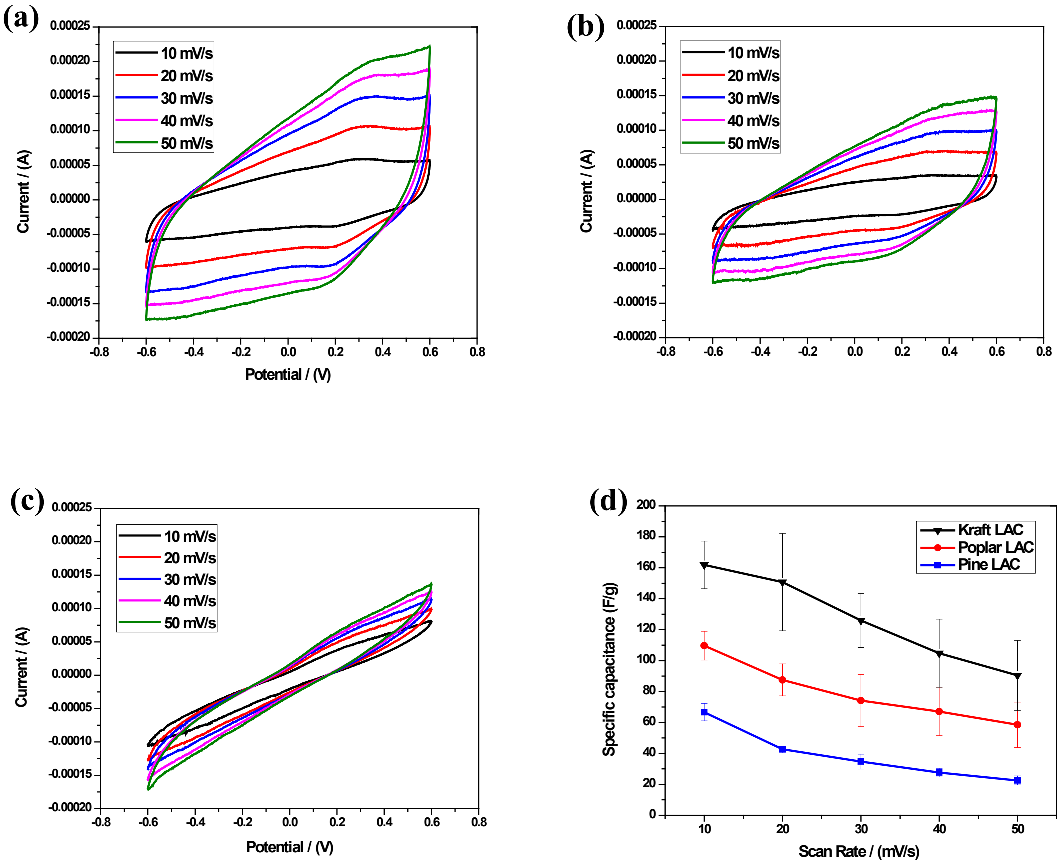

Figure 4.4 Cyclic voltammetry (CV) curves of a) Kraft lignin-derived activated carbon (AC), b) poplar lignin-derived AC, c) pine lignin-derived AC at scan rates ranging from 10 to 50 mV/s, and d) Capacitive performance of lignin-derived ACs in 1 M H_2SO_4 at scan rates ranging from 10 to 50 mV/s.

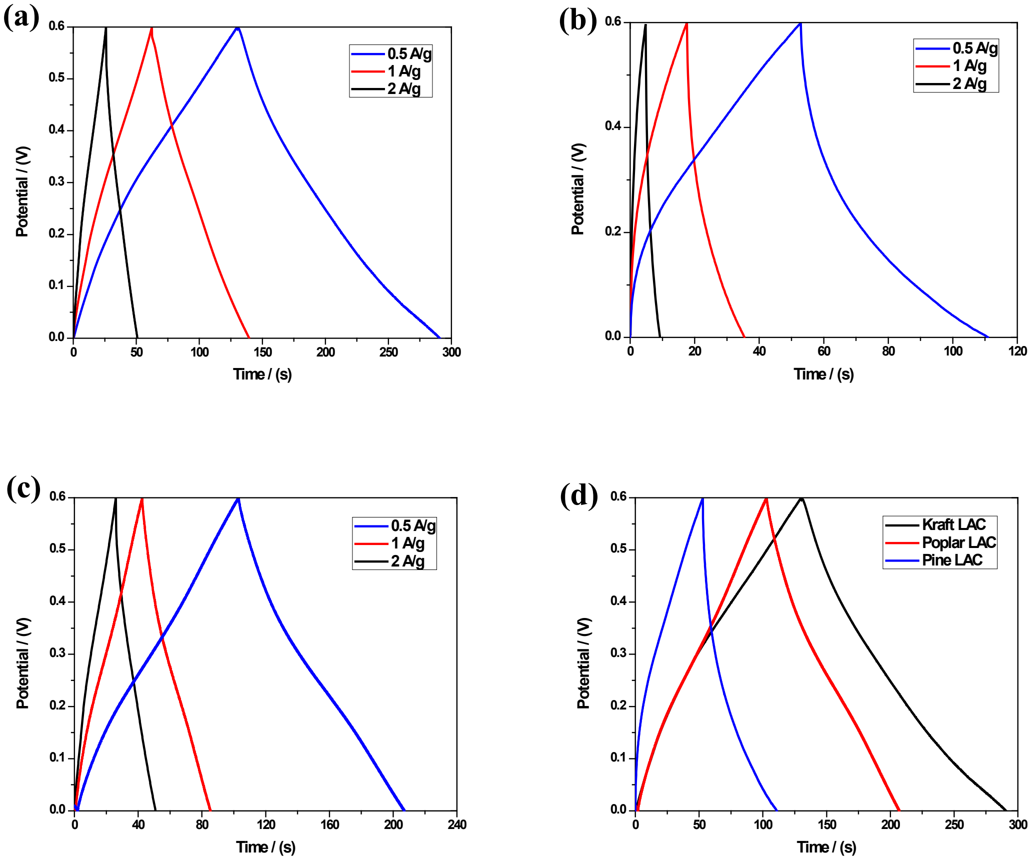

Figure 4.5 Galvanostatic charge-discharge (GCD) curves of a) Kraft lignin-derived activated carbon (AC), b) poplar lignin-derived AC, c) pine lignin-derived AC at current density ranging from 0.5 to 2 A/g, and d) Comparative GCD curves of pine, poplar and Kraft lignin-derived ACs at a current density of 0.5 A/g.

Compared to the literature data shown in **Table 4.1**, both SSA and supercapacitor capacitance presented herein are on the same order of magnitude. The difference may come from dissimilar lignin feedstocks and process conditions. It is worth noting that the main goal of this study is to understand the impact of lignin sources on lignin-derived AC pore structure and thus supercapacitor capacitance from a perspective of lignin composition and structure rather than synthesis a new material with super high performance. Therefore, the process conditions of both carbonization and activation are not optimized [81] and no other additives, such as carbon black, and binder were blended during lignin-derived ACs synthesis so as to enhance conductivity, as reported elsewhere [71, 77, 79].

To further investigate the electrochemical properties of lignin-derived ACs, galvanostatic charge-discharge (GCD) curves were recorded. **Figure 4.5** gives the GCD character of the lignin-derived ACs at current densities range from 0.5 to 2 A/g and all of the GCD curves exhibits a typical triangular shape. As expected, Kraft lignin-derived AC showed the longest charging and discharging time at each current density, while pine lignin-derived AC represented the shortest one, which demonstrate the same capacitive performance trend as the specific capacitance evaluated from CV curves, seen in **Figure 4.5a-c**. At current density of 0.5 A/g, the specific capacitance of pine lignin-derived AC is 48.3 F/g, while poplar and Kraft lignin-derived ACs can achieve 86.7 and 133.3 F/g respectively, as shown in **Figure 4.5d**.

Possible mechanisms of the formation pathway of lignin-derived ACs

Reaction mechanism of lignin pyrolysis was only partly understood due to the complex product composition and possible multiple reaction phases involving complicit prime and secondary reactions [34, 38]. Based on the results from the present study and other literature, a possible pathway for generating the lignin-derived ACs was proposed, which may help understand the different lignin-derived AC’s pore structure between hardwood and softwood lignin, as shown in Scheme 1. During pyrolysis, the depolymerization of lignin starts with the cleavage of ether bonds, such as β-O-4 linkages at low temperature and produce primarily guaiacol – type and syringol – type and a variety of other monomers [42, 43]. It is believed that the prime reaction of lignin pyrolysis involves free radical reactions and the monomer products are presented as free radicals

[38]. Since free radical reaction is a chain reaction, it would not terminate as long as the free radicals are present. Hence, the originally volatilized guaiacol and syringol – typed free radicals formed from ether linkages cleavage would subsequently go through repolymerization and condensation into oligomers and finally form solid fractions, namely char and coke. A portion of the monomers capture hydrogen from other compounds, entering into liquid fraction [38]; while the other portion of monomers further decompose into gases, such as CH_4, CO, CO_2 and H_2 [43]. As the reactions continue, the free radicals chain reaction within char and coke was forced to terminate after devolatilization and depletion of hydrogen, leaving some free radicals to serve as active sites for the activation of lignin-derived ACs. As discussed previously, softwood lignin, such as pine lignin, is dominated by G lignin, while hardwood lignin has an almost equal amount of G and S lignin unit. It is a crucial difference to the free radical reaction of lignin pyrolysis, since hardwood lignin would have significantly more free radicals acquiring from ether linkages cleavage which serve as precursors to propagate the chain reactions and eventually have more change to maintain free-radicals reactive site available for activation. This hypothesis is supported by more efficient devolatilization of hardwood lignin pyrolysis than softwood [42, 43]. Under the presence of a chemical agent, such as KOH, and pyrolysis, the free radicals chain reactions are able to resume and release vapors, such as K, H_2, CO and H_2O, which contribute to the growth of porosity of carbon materials [34].

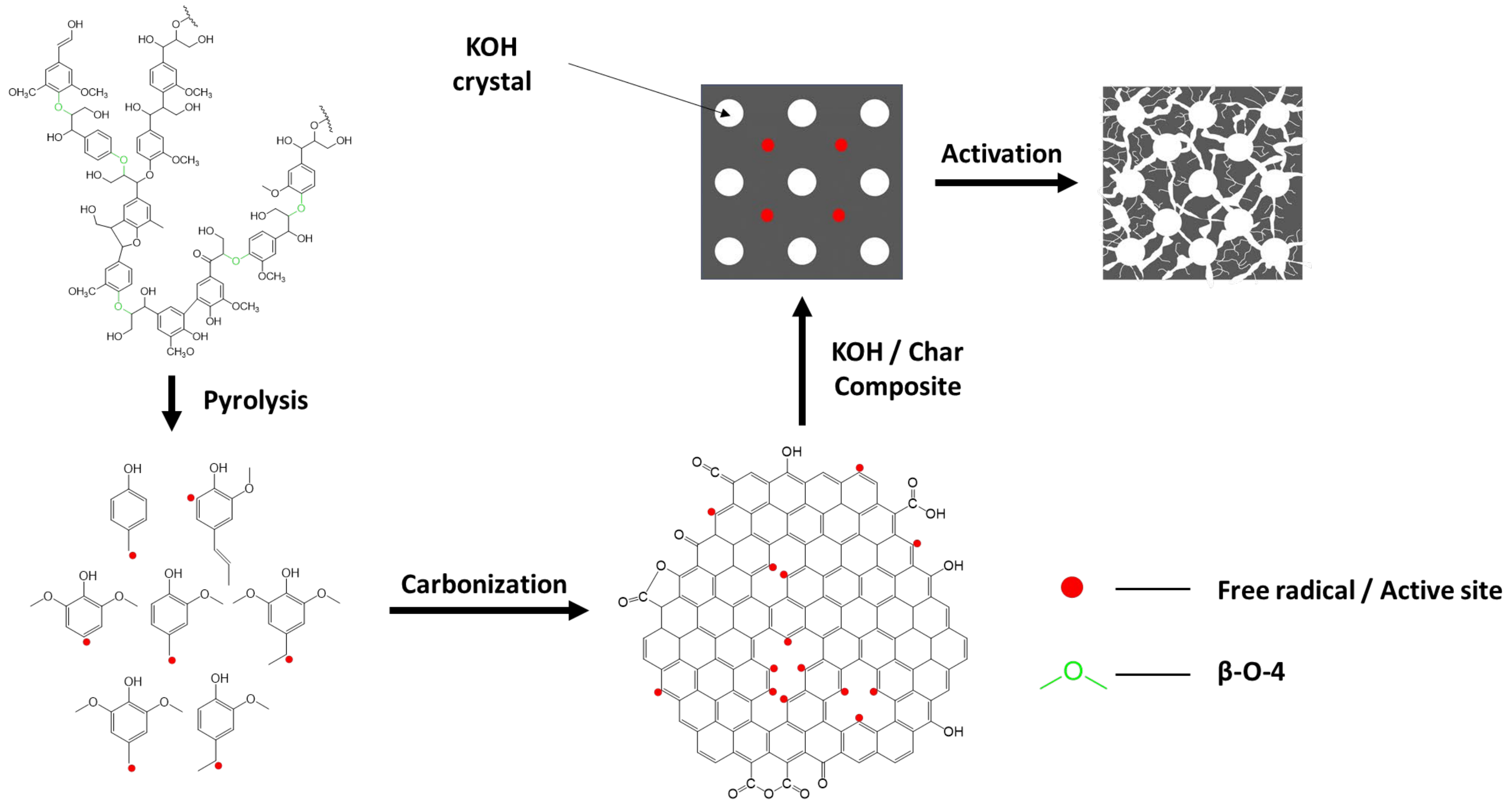

Scheme 4.1 A schematic of possible mechanisms diagram of the formation pathway of lignin-derived AC

Conclusions

In conclusion, lignin-derived activated carbon materials from alkali pretreated hardwood and softwood were synthesized and characterized. Each lignin-derived AC exhibited a three-dimensional pore structure with numerous micro-, meso- and macro-porous channels. Compared to pine (softwood) lignin-derived AC, poplar (hardwood) lignin-derived AC showed a higher level of specific surface area and volume of both mesopores and micropores. When applied as supercapacitor electrodes, the poplar lignin-derived AC had a higher value of specific capacitance at each current scan rate than the softwood lignin-derived AC. X-ray photoelectron spectroscopic (XPS) revealed the presence of oxygen-containing functional groups in all lignin-derived ACs, which contributed additional pseudo-capacitance to the total capacitance. Finally, a possible process mechanism was proposed to help understand the effects of lignin structure and composition on lignin-derived AC pore structure during thermochemical conversion.

Acknowledgements

The authors acknowledge the National Science Foundation under Cooperative Agreement No. 1355438 and the National Institute of Food and Agriculture, U.S. Department of Agriculture, Hatch-Multistate project under accession number 1003563 for supporting this research. The information reported in this paper is part of a project of the Kentucky Agricultural Experiment Station and is published with the approval of the Director. We thank Novozymes for providing enzyme samples and the Idaho National Laboratory for providing plant materials.

Electronic Supplemental Information

Performance of Lignin-Derived Activated Carbons for Supercapacitors: Effect of the Structure and Composition of Lignin Precursors

Wenqi Li[1], Yan Zhang[2], Lalitendu Das[1], Yikai Wang[3], Doo Young Kim[2], Yang-Tse Cheng[3], Jian Shi[1, *]

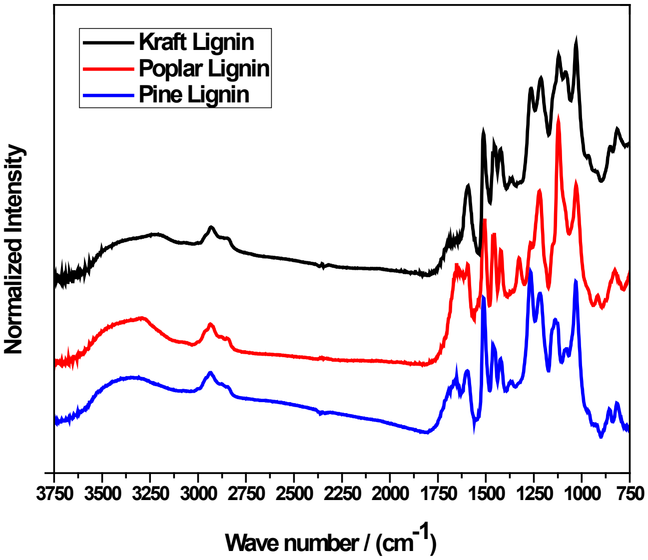

Figure 4.S1 FTIR spectra of pine, poplar and Kraft lignin.

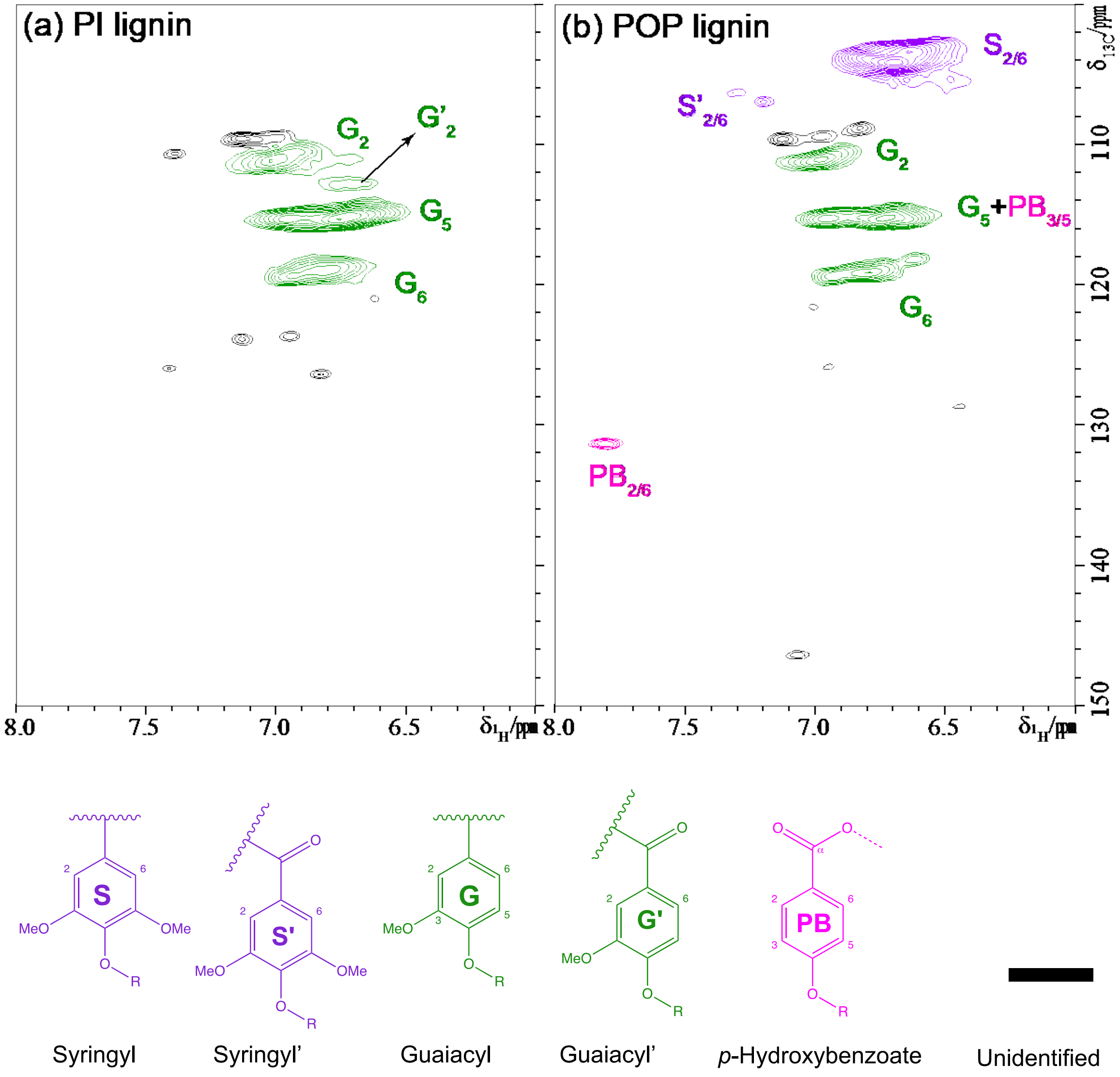

Figure 4.S2 ^{13}C-^{1}H (HSQC) spectra of aromatic regions of alkaline lignin from (a) pine (PI), (b) poplar [262]. The structures of lignin compositional units were coded with colors corresponding to the cross peaks in the spectra.

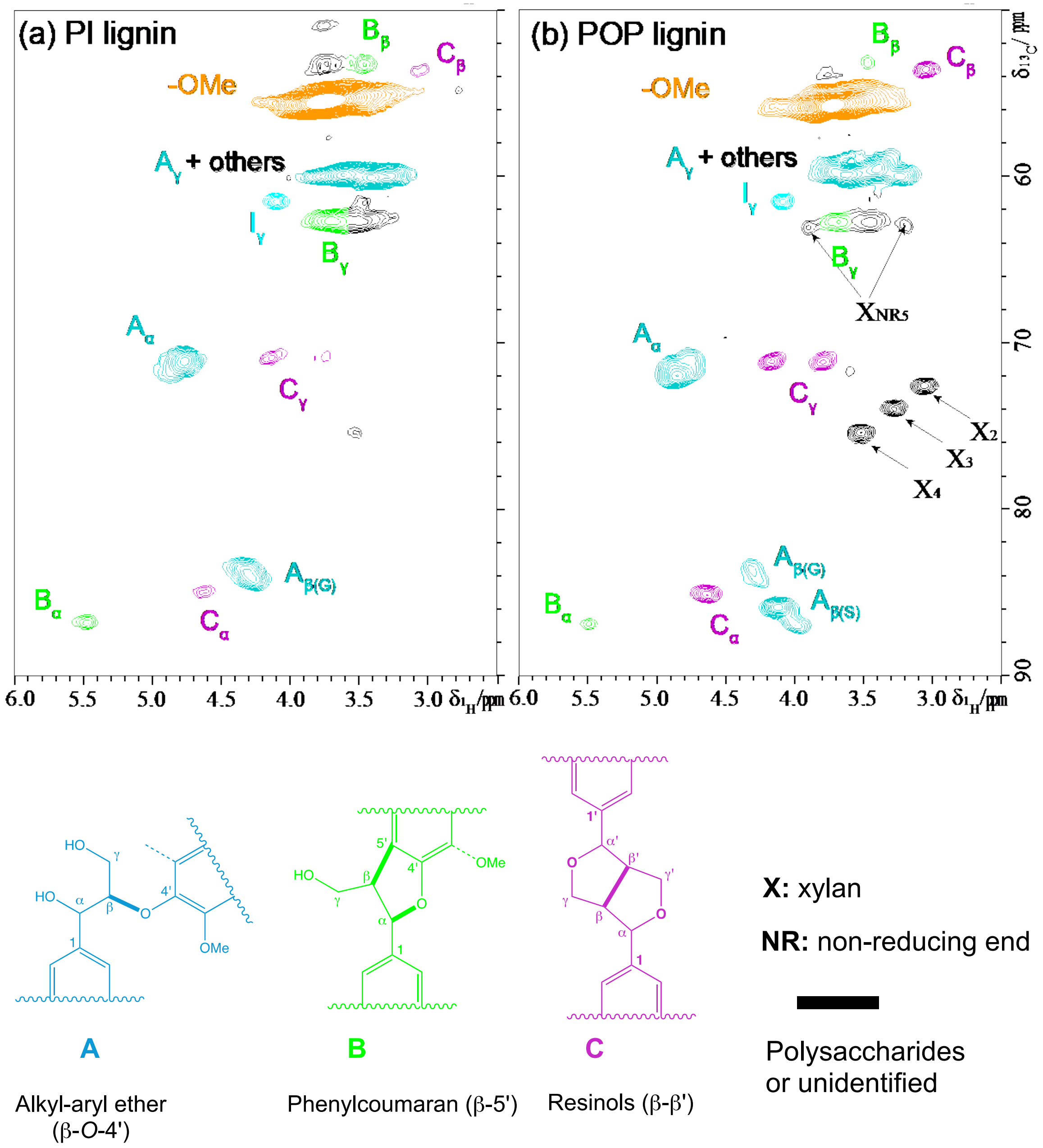

Figure 4.S3. 2D HSQC NMR spectra of alkyl regions of alkaline lignin from (a) pine (PI), (b) poplar [262]. The structures of side-chain linkages were coded with colors corresponding to the cross peaks in the spectra.

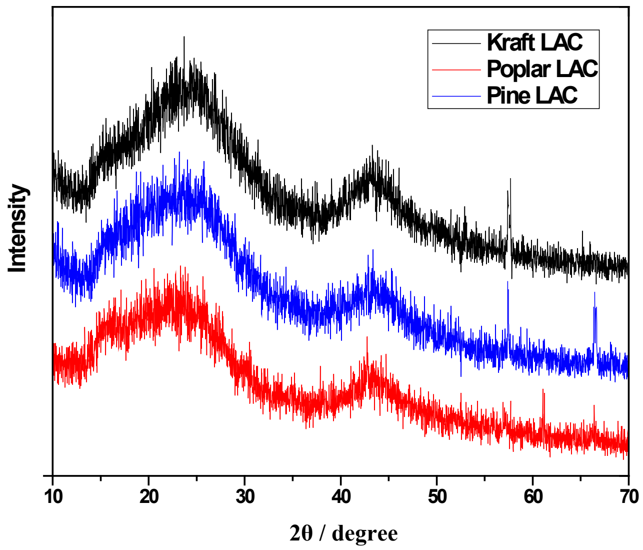

Figure 4.S4 XRD spectra of pine, poplar, and Kraft lignin derived activated carbons.

Table 4.S1 Mass balance for lignin carbonization & activation

Lignin Feedstock	Biochar yield (g/100g lignin)	AC yield (g/100g lignin)
Pine	41.3 ± 3.9	22.2 ± 1.4
Poplar	29.4 ± 0.3	23.2 ± 0.95
Kraft lignin	20.7 ± 2.4	13.4 ± 0.2

CHAPTER 5. ENGINEERING LIGNIN DERIVED CARBON-SILICON NANOCOMPOSITES THROUGH CO-PYROLYSIS AS AN ANODE MATERIAL FOR RECHARGEABLE LITHIUM-ION BATTERIES

ABSTRACT

Converting lignin to high-value chemicals and products along with biofuel production will substantially enhance the economic viability thus contributing to the success of a biorefinery. Silicon has gained increasing attention because of its high specific capacity compared to the commonly used graphite negative electrode in lithium-ion batteries (LIBs). However, the process of lithiation and delithiation inevitably leads to volume expansion of silicon, which causes rapid capacity fading and electrode cracking. In this study, a 3-dimensional, interconnected carbon/silicon composite synthesized from kraft lignin (KL) and silicon nanoparticles (Si NPs) is shown to have a high starting specific capacity of 2932 mAh/g and a retaining capacity of 1760 mAh/g after 100 cycles at 0.72 A/g as negative electrode in a half-cell LIB test. In order to obtain a mechanistic understanding of the effect of lignin properties and processing conditions on the mechanical and electrochemical properties of the lignin-derived electrode materials, the synthesis process of Si/C nanocomposites was investigated using an analytical micropyrolyzer–GC/MS in combination with other analyses. The effect of heating rates, ratio of KL/Si NPs and types of NPs on the volatile products of slow pyrolysis were examined via evolved gas analysis-mass spectrometer (EGA-MS) analysis. The product distributions, including gas, liquid, and solid residue, were tracked during the pyrolysis process under two temperature regions. The morphology, interfacial chemistry, mechanical behavior of the Si/C nanocomposites were further characterized by SEM/in-situ TEM, XRD, Raman, FT-IR, XPS and scratch test. This study establishes a link between synthesis condition, properties of Si/C nanocomposite materials and their electrochemical performance and durability as electrodes in the next generation LIBs.

Keywords: Carbon materials, electrochemical storage, analytical pyrolysis, lignin, morphology

Introduction

Energy is the driving force of economic development and social prosperity and a near-global effort has taken this seriously to fulfill the increasing demands. Accounting for over 80% of today's energy consumption [263], there are increasing concerns about the environmental and societal problems caused by burning fossil fuels, especially the alarming greenhouse gas emissions due to human activities [186]. The biorefinery concept has been put forward, which offers the potential to replace a large fraction of fossil resources in plant-based feedstocks to address demands for energy, chemicals and materials [264]. However, the production costs of lignocellulosic ethanol are not unconditionally as low as that of fossil fuels if not take the hide costs of non-sustainable consumption into consideration, despite various attempts which have been made to improve the viability of lignocellulosic biofuels by increasing enzyme efficiency [265], more efficient pretreatment technologies [4, 266] and gene-modified feedstock.

Lignin is the second most abundant aromatic polymer on earth [238]. As projected by the 2009 Renewable Fuel Standard (RFS2) on the basis of the Energy Independence and Security Act of 2007, approximately 60 million dry tons of lignin annually will be generated as a byproduct from the lignocellulosic biorefineries of the US alone by year 2022 [16]. This will add to the existing ~100 million tons of lignin from paper and pulping industry [239]. Despite its great potential as a feedstock for various high-value chemicals, valorization of lignin is still challenging due to the complex structure and compositional heterogeneity of lignin [16]. Therefore, to unlock the full potential of lignin and enhance lignocellulosic biorefineries' economic viability, other application are being explored [16]. Recently, lignin-derived carbon materials as energy storage materials for electronic devices, such as supercapacitors [241] and batteries have received an increasing interest.

Silicon, because of its high theoretical specific capacity (3600 mAh/g) compared to conventional (and widely-used) graphite (372 mAh/g) [267], has been considered as one of the most promising negative electrode materials for next-generation lithium-ion batteries [268]. However, recent studies have shown that mechanical degradation is responsible for irreversible capacity loss of the Si composite electrodes [118]. Due to irreversible volume change, delamination, and fracture of the Si particles, and loss of mechanical contacts caused by the relentless volume expansion/shrinkage during insertion/extraction of Li ions, the capacity and electronic and ionic conductivity of Si composite electrode degrade quickly [118, 119]. Additionally, development of the solid electrolyte interphase [120] on the freshly damaged Si NPs surface lead to continuous loss of lithium ions and electrolytes, which further contribute to capacity fading of lithium-ion batteries [121]. Therefore, considerable effort has been devoted to improve the electrochemical performance of Si-based lithium-ion batteries through various approaches [122], including structurally engineered Si (e.g. nanostructured Si [123], 3D porous Si particles [124], coating [125] etc.), flexible current collector [126], pre-lithiation [127], electrolyte additives [128], improved binder materials [129-131].

Among these approaches, composite material combining nanostructured Si core with a protecting shell has been considered a promising strategy [132, 133]. Extensive studies have been made to synthesize and examine numerous innovative designs, e.g. carbon-coated Si NPs [134], porous Si nanowires [269] and Si nanotubes [270], graphene and its chemical modified derivative, reduced graphene oxide encapsulated Si NPs [271-274]. Most recently, a lignin-derived C/Si NPs composite prepared via a one-pot, binder-free thermochemical conversion process showed great electrochemical performance as potential application as LIB's negative electrode [136]. Lignin-derived C/Si NPs composite material offers many advantages such as simple synthesis, template and binder free and no toxic solvent required. More importantly, the high-value functional material represents a promising valorization pathway for lignin, which can greatly improve the profitability of a biorefinery using lignocellulosic biomass feedstocks.

In order to ensure electrochemical and mechanical performance of the lignin-derived C/Si NPs composite, a systematic and in-depth understanding of the formation mechanisms of composite material is needed. However, very limited information is available in literature. First, the interaction between the Si NPs and C in the composite is not fully understood. It is important to investigate if there is any chemical bond (and what type) is formed between C and Si NPs and how does it correlate to the rigidity or elasticity of the resulting material. Second, what is the structure of C/Si composite and the correlation between the structural, chemical, mechanical and electromechanical properties? In addition, the thermochemical conversion process, namely co-pyrolysis of lignin and Si NPs, is the essential synthesis step for lignin-derived C/Si composites. Previous studies have focused on properties of the prepared material and its electrochemical performances, while the pyrolysis process itself was overlooked and generally treated as a black box. It is critical to link thermochemical conversion conditions to the characteristics of C/Si composite.

In this study, a commercial pyrolyzer-GC/MS system was used, to our best knowledge for the first time to, mechanistically investigate the formation process of a C/Si composite through co-pyrolysis of lignin and Si NPs. Comprehensive analytical tools were then used to investigate morphological, physical and chemical structure of the synthesized materials.

Based on those, the impact of the co-pyrolysis to the mechanical and electrochemical performance of the C/Si NPs composite was studied. This study is the first step to understand the processing-structure-property relations and provides a basis to advancing the development of lignin-derived C/Si NP composite anode material.

Experimental

Materials

Kraft lignin (KL) and anhydrous N, N-dimethylformamide (DMF) were purchased from Sigma-Aldrich. Silicon nanoparticles (Si NPs) with a diameter of 30-50 nm were purchased from Nanostructured & Amorphous Materials (Katy, TX). Lithium foil with thickness of 0.75mm was purchased from Alfa Aesar. The electrolyte was 1M LiPF6 in a mixture solution of ethylene carbonate (EC), diethyl carbonate (DEC) and fluoroethylene (FEC) with a ratio of 9:9:2; EC, DEC and FEC were purchased from Gotion (Fremont, CA). A monolayer polypropylene membrane separator (Celgard 2400) was provided by Celgard as a gift. Electrodeposited copper (Cu) foil (thickness, 18 μm; density, 17.48 mg cm^{-2}) was purchased from Pred Materials (New York, NY).

Preparation of lignin-derived C/Si NPs composite

KL was dissolved in DMF to make an 18.5 wt% solution at 60 °C. Afterwards, Si NPs were gradually added into the solution at a 1:1 wt. ratio to lignin with continuous stirring until the Si NPs uniformly dispersed in the solution. The prepared slurry was coated onto the Cu foil using a Doctor blade with a fixed gap of 127 μm and then air-dried at room temperature before vacuum oven drying at 120 °C overnight. After drying, the composite coated Cu foil was transferred into a tube furnace. Under constant argon flow of 0.4 L/min, the furnace was programed to heat from room temperature to 600 °C ramping at 2 °C/min and holding for 2h at the target temperature before cooling down to room temperature.

Morphology and structure characterizations

Images of the kraft lignin (KL) and lignin-derived C/Si NPs composite were obtained using a scanning electron microscopy (SEM, Quanta 250 FEG, Thermo Fisher Scientific) and a transmission electron microscopy (TEM, Talos F200X, Thermo Fisher Scientific). X-ray powder diffraction (XRD) spectra were acquired through X-ray diffractometer with graphite monochromatized Cu-Kα (Kα = 0.15406 nm) radiation (D8, Bruker). Raman spectra of the samples were recorded with a Raman microscope (DXR, Thermo Scientific). Chemical structure of the KL and C/Si NPs composite analysis of the samples were carried out with a Fourier Transform Infrared Spectrometer (FTIR, Nicolet iS50, Thermo Fisher Scientific), at a resolution of 4 cm^{-1} for 32 scans in the range of 450 to 3000 cm^{-1}. Surface chemistry of the samples were examined by an X-ray Photoelectron Spectrometer (XPS) system (K-Alpha, Thermo Fisher Scientific) by irradiating monochromatic Al Kα x-rays (energy of 1486.6 eV) onto a 400 µm diameter focused spot on the sample.

Mechanical property characterization

The mechanical properties were determined through a scratch test using a nanomechanical test system (NanoTest Vantage, Micro Materials), which equipped with a conical diamond stylus (tip radius, 10 µm; cone angle, 60º). In a typical test, a 12 mm diameter electrode disc was glued to a flat sample stage. The applied load was from 0.1 to 40 mN, which was applied after 50 µm and the scratch distance was set to 2500 µm. For each sample, scratch tests were conducted six times to guarantee reproducibility.

Electrochemical performance characterization

The electrochemical performance was determined in CR2025 type half-cell configuration coin cells, which were assembled in an argon-filled glovebox. Electrochemical tests were performed using a multi-channel potentiostat (VMP-3, Bio-Logic Science, Knoxville, TN) at room temperature. The electrochemical properties of the electrodes were measured within a voltage range of 0.01−1.0 V. The Si NPs content of the C/Si NPs composite was calculated by determining the weight change of the electrodes before and after carbonization, while assuming that the weight of Si NPs and Cu foil remain constant. Electrodes were punched into discs with a diameter of 12mm for electrochemical tests and the loading of C/Si NPs was 1.0-1.2 mg cm^{-2}, while the loading of Si NPs was 0.63−0.76 mg cm^{-2} (Si NPs content of the C/Si NPs was around 63%).

Evolved gas analysis-mass spectrometer (EGA-MS) analysis

EGA-MS analysis was performed in a micro-pyrolyzer (EGA/PY-3030D, Frontier Lab, Fukushima, Japan), of which the reactor temperature can be precisely controlled from 40 to 900 °C with 1 °C intervals. At the EGA-MS mode, the micro-pyrolyzer was directly connected to a MS detector (5977A, Agilent, Santa Clara, CA) via a deactivated metal tube (UA-DTM-2.5 N, Frontier Lab) using helium was carrier gas. For a typical EGA-MS analysis, 200 ± 10 µg of the KL or 400 ± 20 µg of KL/Si NPs was placed in a deactivated stainless-steel cup. The reactor temperature of the pyrolyzer was programed to increase from 100 °C to 800 °C with a 2 °C/min ramp. The EGA-MS profiles were displayed by recording total ion intensity of the MS versus the programmed temperature.

Analytical pyrolysis-GC/MS (PY-GC/MS)

For analytical pyrolysis, the micro-pyrolyzer was connected to a GC/MS (7890B/5977A, Agilent, Santa Clara, CA). The volatiles from the pyrolyzer were separated via a capillary GC column (Ultra Alloy-5, Frontier Lab, Fukushima, Japan) using helium as the carrier gas. The GC was equipped with a two-way splitter which directed the gas stream into both MS and flame ionization detector (FID). The MS was used for compound identification and the FID detector was used for compound quantification. The calibration curves of the products were created using five different concentrations of acetic acid (carbohydrates), toluene (aromatic hydrocarbons), phenol (H type substances, C6 and C6C1), 4-propylphenol (H type substances, C6C2), guaiacol (G type substances, C6C1), vanillin (G type substances, other than C6C1), syringaldehyde (S type substances, PAHs, and long chain fatty acid). The GC oven was programed to start by holding at 40 °C for 2 min and then heated to 320 °C at a heating rate of 20 °C/ min before holding at 320 °C for an additional 10 min.

At the fast pyrolysis, the pyrolyzer were preset at the desired temperature before sending the sample cup into reactor. For a typical analysis, 200 ± 10 µg of the KL or 400 ± 20 µg of KL/Si NPs was placed in the deactivated stainless-steel cup. Slow pyrolysis tests were carried out in HC-GC/MS mode. The micro-pyrolyzer system was also equipped with a system (MicroJet Cryo-Trap-1030Ex, Frontier Lab) at the head of the GC column to selectively trap volatiles generated from a desired temperature region with liquid nitrogen before transferring to GC-MS for detailed composition analysis, which is referred as heart-cutting (HC) mode in the present study.

Results and discussion

Morphology and structure

The chemical structure of KL was characterized via $^{13}C{-}^{1}H$ HSQC NMR, as shown in **Figure 5.S1**. The KL was dominated by G-unit (96.4%) with a slight amount of S-unit (3.6%) suggesting a softwood origin. Since kraft lignin is isolated from biomass through kraft process, there are a small amount of polysaccharides, (glucan and xylan, of 0.11% and 0.96%, respectively) (**Table 5.S1**), which remained from the kraft process and ash, mainly composed of inorganic minerals (Al, Ca, Cu, Fe, K, Mg, Mn, Mo, Na, P and S) [275]. GPC analysis showed that the KL has a relatively low molecular weight [175] of 5736.11g/mol and PDI of 1.88 (**Table 5.S1**). Due to the strong correlation between the molecular weight distribution of lignin and its thermal proprieties, it is believed that the low molecular weight corresponds to a better thermal fusibility [276]. In addition, the polydispersity index (PDI) represents the heterogeneity of the molecular size distribution of lignin. A relatively low PDI [175] suggest the KL has good uniformity in its molecular weight distribution. FTIR characterization, as shown in **Figure 5.S2**, indicates that the KL contains several oxygen-containing functionalities, such as C-OH, C=O, COOH etc.

Figure 5.1a illustrates synthesis processes of the lignin-derived C/Si composite material, including preparation of KL/Si NPs mixture and carbonization process to form C/Si NPs composite. The TEM and SEM images of the Si NPs can be seen in **Figure 5.1b - d**. TEM images reveal that the Si NPs is round crystalline particles with a diameter of 30 – 50 nm. It is noted that there is a very thin silicon oxide layer (around 1 nm) on the surface of the Si NP, because pristine silicon is naturally prone to oxidation [277]. The raw KL powders are fine particles with high surface roughness as shown by the SEM image (**Figure**

5.1e) [4]. The solubility of lignin in different solvents is depending on solvent properties (pH, polarity, hydrophilicity etc.), monomer composition and functional groups of the lignin and the fractionation technologies to produce lignin [278]. The KL used in this study was fully dissolved in DMF at room temperature. It is believed that the hydroxyl groups on the lignin structure can form interactions with H bonds of Si NPs [279] when lignin is well dispersed in DMF solution. After the carbonization, the C/Si NPs composite with tunnels and pores in different sizes was formed as shown in **Figure 5.1f**.

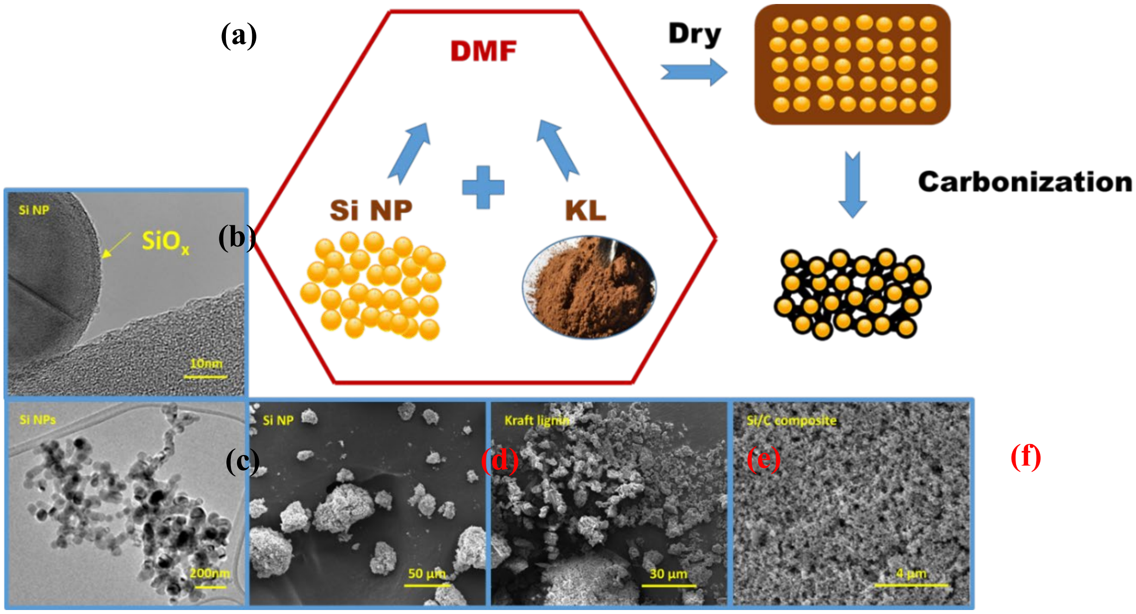

Figure 5.1 a) Schematic illustration of the synthesis of the C/Si NPs composite electrode; TEM images of b) a close view of a Si NP; and c) a cluster of Si NPs; SEM images of d) Si NPs; e) KL and f) the resulting C/Si NPs composite material obtained via pyrolysis at 600 °C.

Figure 5.2a shows XRD patterns of the Si NPs and the lignin-derived C/Si composite obtained from pyrolysis at 600 °C. The characteristic diffraction peaks at 2-theta of 28.47, 47.35, 56.17, 69.20, 76.45, 88.12 degree represent the lattice planes of (111), (220), (311), (400), (331), (422) in silicon, respectively[280]. A previous study has shown a layer of silicon carbide (SiC) coated on the surface of silicon through pyrolysis [281]. However, in this study, no sign of SiC was observed in the XRD spectrum, probably because the formation of silicon carbide requires a higher temperature between 700-1400 ℃ [281]. Silicon carbide is unfavorable since it has a low electronic conductivity, thus leading to a low high electrochemical performance. The overlapping peaks among Si NPs and C/Si NPs composite suggest that Si NPs didn't subject to significant phase change during formation of the C/Si NPs composite [282]. The broad peak appeared around 2-theta of 22 degree after carbonization, corresponds to (002) lattice plane due to the formation of amorphous carbon [283].

Figure 5.2b shows the Raman spectra of Si NPs and the lignin-derived C/Si composite obtained from pyrolysis at 600 ℃. Pristine Si NPs exhibited a sharp peak at 520 cm^{-1} with a barely identifiable shoulder at 480 cm^{-1} (representing the amorphous portion of Si), confirming the crystalline nature of Si NPs [284]. With carbon coated on Si NPs, the C/Si composite displayed two major peaks in addition to the peaks of Si NPs: the disordered carbon (D band) at 1360 cm^{-1} and the graphite band (G band) at 1580 cm^{-1} [285, 286]. The ratio of the D and G band intensities (I_D/I_G) is 1.7, which is in agreement with XRD data, suggesting that the coating of Si NPs was poorly organized amorphous carbon [285].

(a)

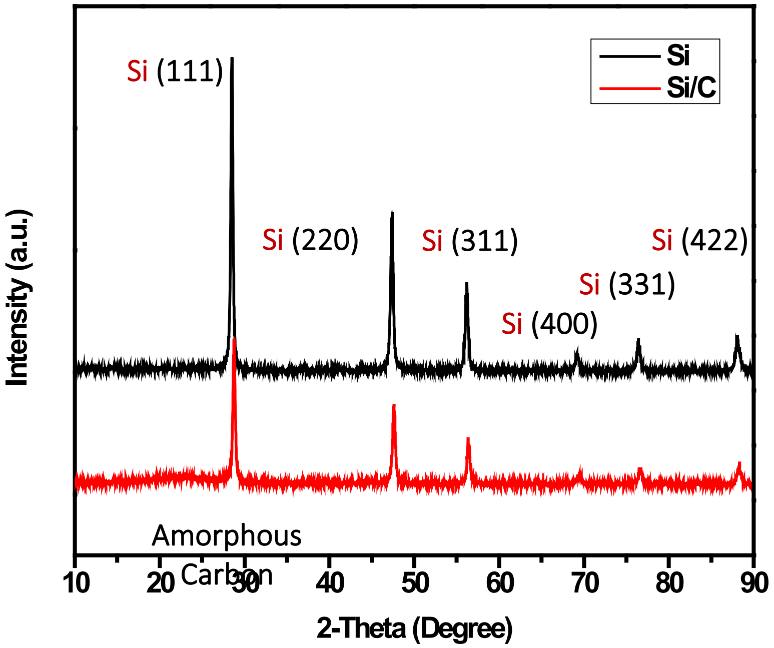

(b)

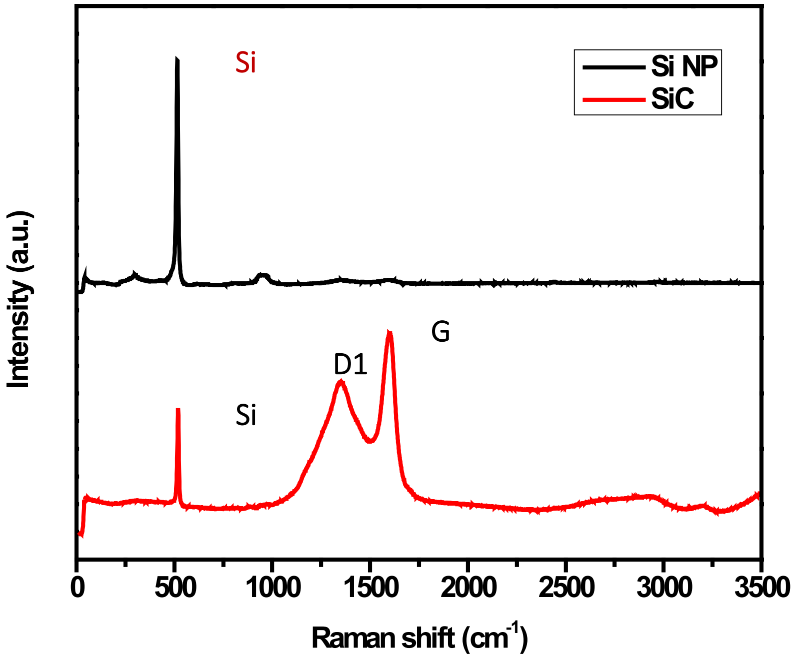

Figure 5.2 a) XRD and b) Raman spectrum of Si NPs and C/Si NPs composite electrode obtained via pyrolysis at 600 °C.

In order to investigate the interactions between C and Si NPs within the C/Si NPs composite, the chemical structure of the C/Si NPs composite were investigated using FTIR and XPS, as shown in **Figure 5.3** Several signature bands were identified in FTIR spectra of the Si NPs and lignin-derived C/Si composite obtained from pyrolysis at 600 °C. The absorbance bands at 2160 and 2254 cm^{-1} correspond to the various SiH_x stretching modes [287]. The broad bands covering from 950 to 1250 cm^{-1} represent Si-O-Si bond, corresponding to the amorphous silicon oxide [287]. The band at 450 cm^{-1} is attributed to Si-O rocking vibration [288]. The presence of amorphous silicon oxide in the Si NPs spectrum is consisted to the native oxide layer surrounding the pristine Si NPs as observed in **Figure 5.1b**. Interestingly, the bands representing Si-O-Si bond and Si-O rocking vibration were significantly increased in C/Si NPs composite. Given the fact that Si-O bond was increased while the Si-C bond is absent, the C and Si NP in the composite were most likely bonded via oxygen (R1-Si-O-C-R2), instead of direct Si-C. While the absence of the SiH_x band in the C/Si composite can be explained by hydrogen desorption from silicon at elevated temperature where the exposed dangling Si–H bond bonds were subsequently taken by oxygen [287].

Figure 5.3b shows the Si 2p spectra of Si NPs and the lignin-derived C/Si NPs composite obtained from pyrolysis at 400, 600 and 800 °C. Generally, the Si 2p XPS spectrum has two distinct binding energy regions. The region centered at 99.4eV corresponds to the elemental Si; while the region centered at 103.5eV represents the native oxide layer around Si NPs. The Si 2p peak of the elemental Si region displays two closely spaced spin-orbit components, namely Si $2p_{1/2}$ and Si $2p_{3/2}$. The splitting can be normally ignored, and the two components just need to be considered as elemental Si. However, it is noted that the spectral resolution of the two spin-orbit component is affected by the amorphous/crystallinity nature of the Si element and better resolution of spin-orbit components usually corresponds to more crystalline Si [289]. So, the satisfying Si 2p spectral resolution of the spin-orbit components displayed in **Figure 5.3b** self-explains the crystalline nature of the Si NPs, which is agreed with results from the Raman spectrum. As carbon coated around Si NPs via carbonization, the intense of elemental Si peak decreases while SiO_x peak increases. The trend gets more pronounced with increasing pyrolysis temperature from 400 to 800 °C. At 800 °C, there was no elemental Si peak at all, indicating that the whole Si NPs were covered by a carbon layer.

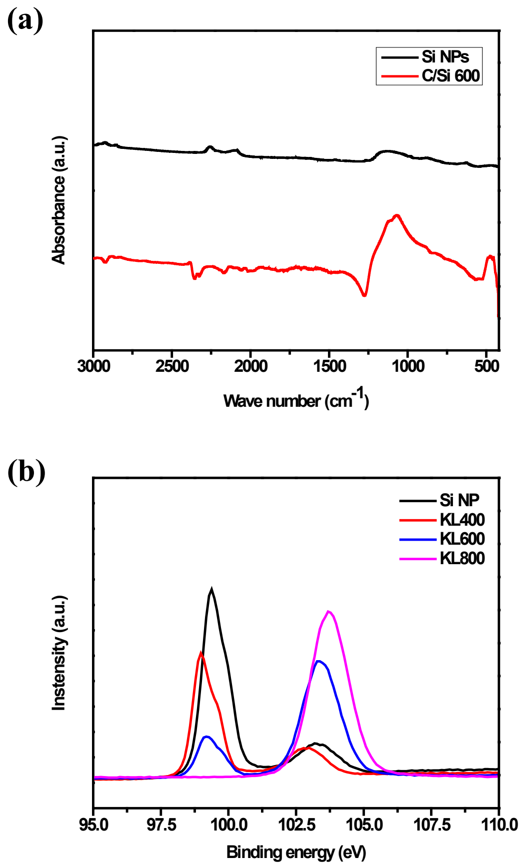

Figure 5.3 a) FTIR and b) XPS spectrum of Si NPs and C/Si NPs composite electrode obtained via pyrolysis at 600 °C.

TEM images of the Si NPs and lignin-derived C/Si composite obtained from pyrolysis at 600 °C provide more direct visual evidences that support the spectrometric results. As can be seen from **Figure 5.4a**, the round crystalline Si NPs with a diameter in range of 30 – 50 nm were coated by a thin layer (around 1nm), representing the amorphous silicon oxide layer that covers the surface of native Si NPs. The coating layer grew significantly to around 5-10 nm on the particles of C/Si NPs composite after carbonization, as shown in **Figure 5.4b**. Surprisingly, the layer was not elementally dominated by C, instead, a mixture of C and O (**Figure 5.4c**, elemental mapping of C, O and Si) and the elemental O was evenly dispersed in the coating layer, as shown in **Figure. 4d** (elemental mapping of just O and Si). This observation corroborates the FTIR and XPS results that Si-O-C and/or Si-O bonds became bountiful in C/Si NPs composite. Interestingly, **Figure 5.4c** also shows that the elemental C in the composite is not evenly dispersed after carbonization. Although the C seems evenly dispersed in the porous carbonaceous layer coated on the surface of Si NPs, there are spots of enriched C between Si NPs (**Figure 5.4c**). Since the intrinsic electrical conductivity of Si is low, conductive additive is usually introduced in Si-based composite anode to satisfy the conductivity requirement and carbonaceous materials are well known for its good electrical conductivity [290]. Those C-rich spots likely serve as bridges linking Si NPs into a network in the C/Si NP composite. The cross-linked network could offer enhanced electrical conductivity as compared to the aggregates of loosely packed C and Si NP particles.

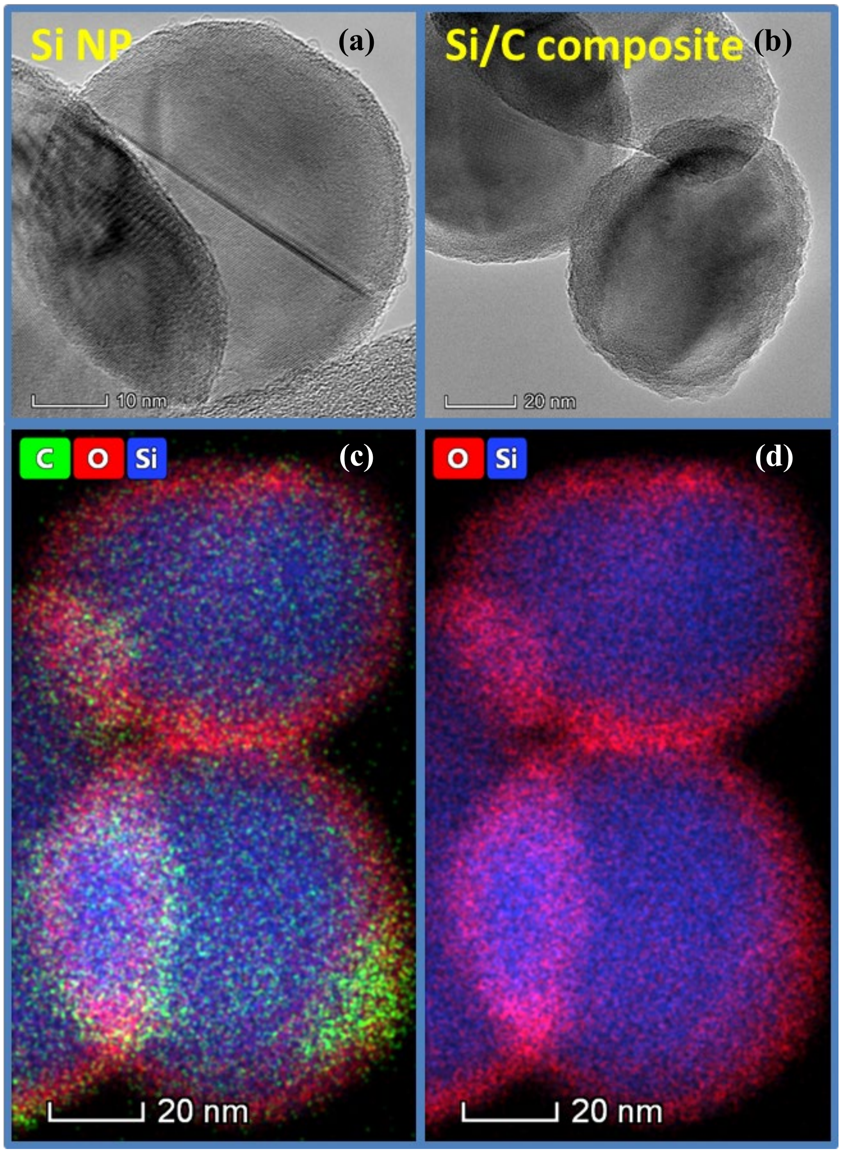

Figure 5.4 TEM images of a) Si NPs and b) C/Si NPs composite and elemental mapping of c) C, O and Si and d) O and Si of the C/Si NPs composite.

Mechanical property

It is believed that the pulverization and delamination of electrode layer caused by the unbounded volume change of Si particles impair the mechanical contact between the active material and the current collector, and thus undermine the electrical conducting network [291]. Therefore, to ensure sufficient mechanical integrity and electronic conductivity of electrode material, a number of polymeric binders have been investigated, such as polyvinylidene fluoride (PVDF), Nafion, sodium alginate (SA) and carboxymethyl cellulose (CMC) [118, 292, 293]. However, the correlation between binder properties and electromechanical stability has not been fully understood. Some believe that a highly extensible elastomeric composite tolerant of huge volumetric changes serves better in maintaining the mechanical integrity and electronic conductivity [294]; while other studies suggested that stiffer binders actually work better in Si-based composite electrodes than those elastomeric alternatives [118, 293]. A recent study demonstrated that when used as a binder in Si-based composite electrodes both the stiffer SA and the more flexible Nafion demonstrated better electrochemical performance than PVDF did [295], despite the fact that both elastic modulus and hardness of PVDF are in between those of SA and Nafion. Adhesion property of electrode to current collector is also believed critical to electrochemical performance of Si-based composite electrodes [296]. PVDF-Cu interface exhibited a much stronger adhesion than SA-Cu, but only demonstrated an inferior electrochemical performance [297]. It is proposed that it is not the mechanical property (elastic modulus and hardness) of the binder material itself, nor the adhesive strength between electrode laminate and current collector, but the cohesive strength between the binder and Si particles which most affects the electrochemical performance of anode material [297]. Therefore, scratch tests were performed to determine the cohesive properties of the C/Si NPs composite in this study.

Scratch tests provide a better understanding of the cohesive properties of different anode materials prepared with PVDF/Si NPs composite and C/Si NPs composite obtained from co-pyrolysis (shown in **Figure. 5.5**). Such cohesive property reflects the interactions among the composite components; for PVDF/Si NPs composite the interaction between PVDF and Si NPs while in case of the C/Si NP composite the interactions between Si NP, O and C. At the same normal load, the scratch depth on the PVDF/Si composite is obviously wider than that of C/Si NPs composite. As indicated by the extent of delamination (**Figure 5.5b-g**), the C/Si NPs composite gained a better scratch resistance as compared to the PVDF/Si NP composite, possibly due to the superior interaction among Si, O and C (R1-Si-O-C-R2). The fluctuations in the scratch depth versus the scratch distance profiles (S-D profiles) shown in **Figure 5a** suggest that mechanical degradations occurred [298]. A giant peak (fluctuation) appeared on the scratch depth profile of PVDF/Si NPs composite in the beginning of the test, suggesting severe failure under a normal loading as low as around 10 mN. In comparison, no obvious fracture was observed on the C/Si NPs composite under a normal loading up to 40 mN (maximum normal loading). The scratch test results indicate that there was an enhanced cohesion strength between Si NPs and C likely due to the bonds formed among Si and C through O during pyrolysis, which in turn significantly improved the mechanical properties of the C/Si composites.

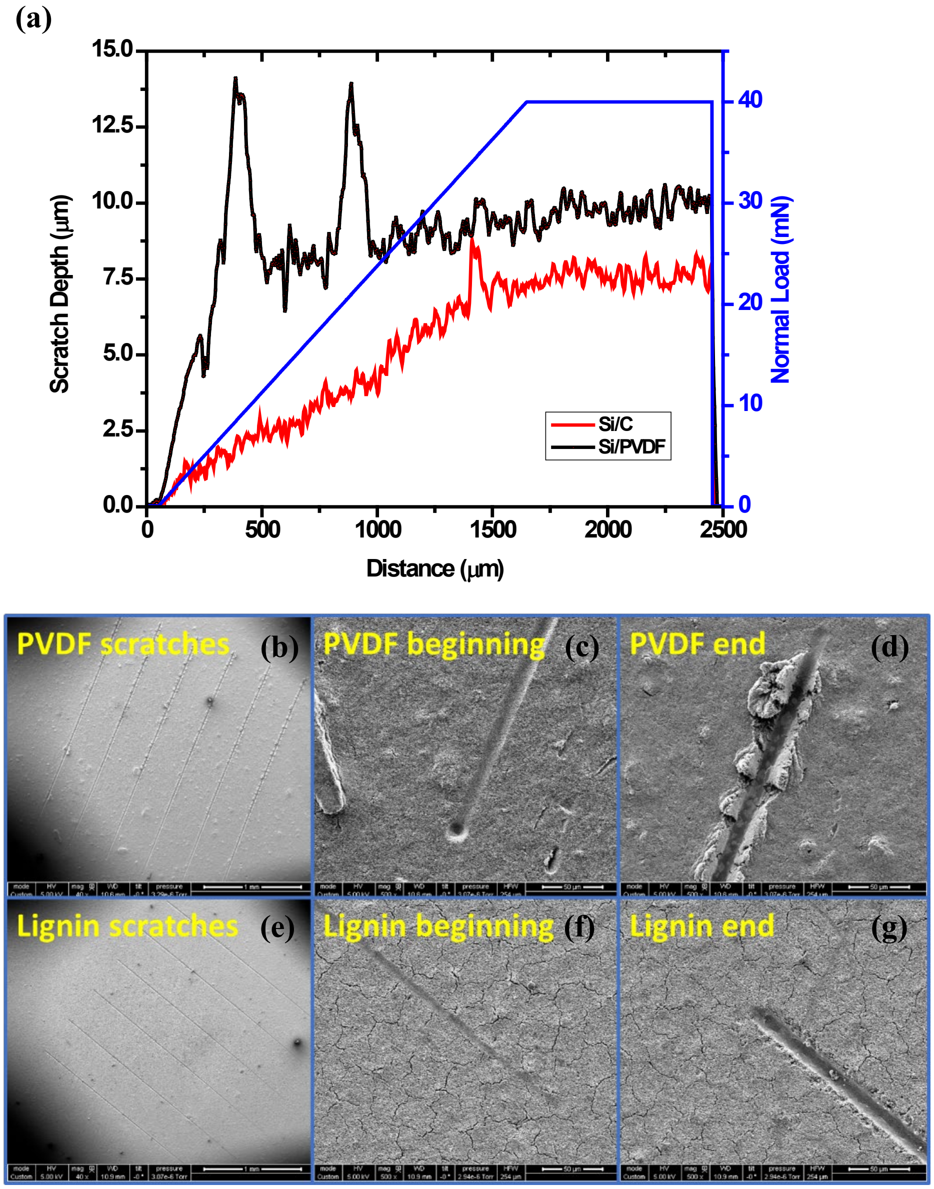

Figure 5.5 Scratch test results of the PVDF and KL electrodes a) Scratch depth profiles of the PVDF and KL binders as a function of scratch distance; SEM images of the b) overall, c) beginning and d) end of micro-scratch tracks for the electrode with PVDF binder and d) overall, e) beginning and f) end of micro-scratch tracks for the electrode with KL binder.

Pyrolysis temperature needs to be well controlled to ensure the quality of the C/Si NPs composite material. As shown in **Figure 5.S3**, the electrode Cu sheet was severely curled and tore as the pyrolysis temperature further increased from 600 to 800 °C. Since

Si-O bond (452kJ/mol) has a stronger bond energy than C-O bond (358kJ/mol), the C-O bond will break before Si-O bond at high temperature of 800 °C [299]. As a result, the dangling O will couple with Si to form more stable O-Si-O [287], which explains the decreasing Si but increasing SiO_x peak with respect of temperature observed in XPS spectra. The increasing bond energy of O-Si-O will give rise to the growth of surface and interface stress [300], which cause the failure of electrode as pyrolysis temperature increased from 600 to 800 °C. Therefore, it suggests that there might be a fine balance between bonding Si and C via O, which can be tailored by controlling thermal conversion conditions.

Electrochemical performance

Figure 5.6 demonstrates the electrochemical behavior of the lignin-derived C/Si NPs composite as compared with currently popular LIB's anode materials at 0.2C (1 C=3579 mAh g^{-1}), including PVDF, Nafion, sodium alginate (SA) and carboxymethyl cellulose (CMC). The discharging capacity of PVDF/Si electrodes degrades severely from 3533 to 882 mAh g^{-1} in the first 4 cycles, which followed by a continuously falling to 510 mAh g^{-1} until finally arriving at 334 mAh g^{-1} at 100 cycles. CMC/Si, SA/Si and Nafion/Si significantly improved cycling performance of Si composite anode, retaining capability of 1295, 1680, and 1984 mAh g^{-1}, respectively, after 100 cycles. Comparing to the four popular binders, the C/Si NPs composite exhibited a comparable cycling performance to CMC/Si, SA/Si but was better than Nafion/Si. The C/Si NPs composite achieved a reversible capacity of 2932 mAh g^{-1}, at the first cycle and maintained capacity over 2500 mAh g^{-1} until the 73 cycles before retaining at 1760 mAh g^{-1} after 100 cycles.

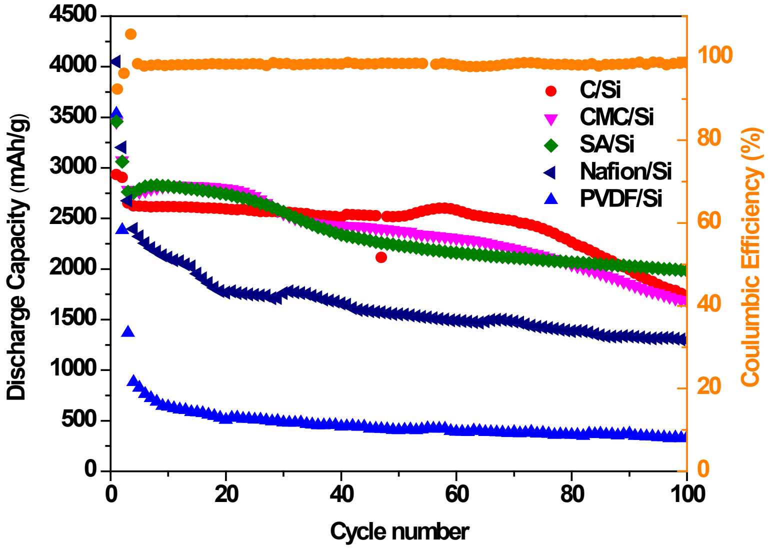

Figure 5.6 Electrochemical performance of C/Si NPs composite electrodes compared with currently popular Si-based anode electrode materials [119].

Recent studies have shown that the rapid capacity loss of Si NPs composite electrodes is caused by mechanical degradations as a result of severe volume change during charge and discharge [118]. The good electrochemical performance of a C/Si composite-based anode demonstrates that the enhanced cohesion strength between Si NPs and lignin-derived carbonaceous material significantly improved the cycling stability of the C/Si composites electrode, which can be attribute to the following aspects. First, the coating layer is able to mitigate the mechanical degradation through either restricting excessive volume change during electrochemical cycling with chemical bond among Si, O, and C, or form a shell to protect the Si NP core from redundant lithiation. Second, the aggregated carbon framework bridges the Si NPs to assure a sound electronic conductivity; while the porous carbonaceous layer surrounding the Si NPs allows Li ions to permeate the coating layer thus provide excellent ionic conductivity of the C/Si composite electrode.

EGA-MS and HC-GC/MS

Knowing that the physical, mechanical and electrochemical performance of the C/Si NP composite materials are dependent on pyrolysis conditions such as temperature and heating rate, it is critical to understand the chemical aspect of the pyrolysis process to correlate the pyrolysis chemistry with the material property. Such knowledge can help to guide the synthesis process and ensure the quality control of the mechanical and electrochemical performance of the prepared materials. However, this knowledge is currently missing. To better understanding the formation mechanisms of the C/Si NPs composite, EGA-MS and HC-GC/MS analysis were carried out as discussed in the following section.

Figure 5.7a compared the GC/MS chromatograms acquired from fast pyrolysis of KL and KL/Si NPs (1: 1 wt. ratio). The temperature ramp of fast pyrolysis was as fast as a few hundred degrees Celsius per second. No differences on either products distribution or yields can be observed from the chromatograms, which indicates that Si NP did not cause significant change to the thermochemical reactions of KL during fast pyrolysis. However, the effect of Si NP on the KL depolymerization became obvious during slow pyrolysis as temperature ramp decreases to 2 °C/min. As shown in **Figure 5.7b**, two continuous peaks can be seen on the EGA-MS profile during slow pyrolysis of KL at 2 °C/min. The first started at ~120 °C and peaked at ~220 °C, followed by a broad second peak at ~334 °C before it became flat at 500 °C. The profile indicates the thermal decomposition of KL started at temperature as low as 120 °C, while most volatiles evolved at around 334 °C and the reaction terminated at around 500 °C. In comparison, when KL and Si NPs was co-pyrolyzed (at 1:1 ratio) at 2 °C/min ramp, besides the large peaks, there was an additional volatile peak appeared between 500 to 700 °C, where the pyrolysis of just KL had completed at this temperature. The peak at 500-700 °C increased accordingly when KL to Si NPs ratio was reduced to 1:2. However, no such peak can be spotted during co-pyrolysis of KL and SiOx NPs regardless the mixture ratios (**Figure 5.7c**). This observation points to possible interactions or even reactions between KL to Si NPs during slow pyrolysis. The EGA-MS profile only offers a rough snapshot about the KL decomposition with or without the presence of Si NPs during temperature from 100 to 800 °C. To gain more insights about the product evolving profile, volatiles collected from two temperature regions, 100-500 °C and 500-800 °C, respectively, were further analyzed by GC/MS using the heart-cut (HC) mode.

(a)

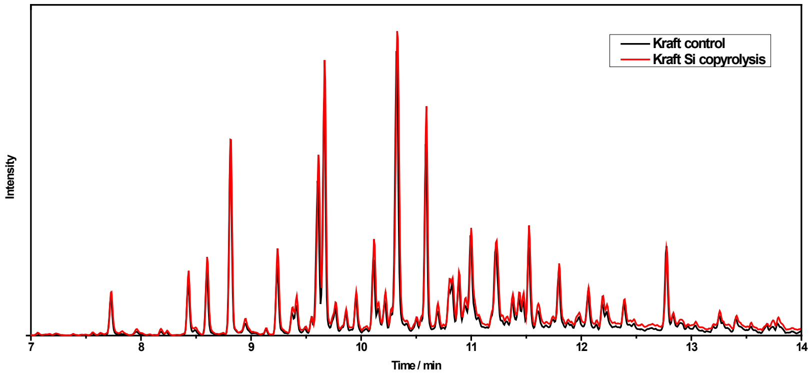

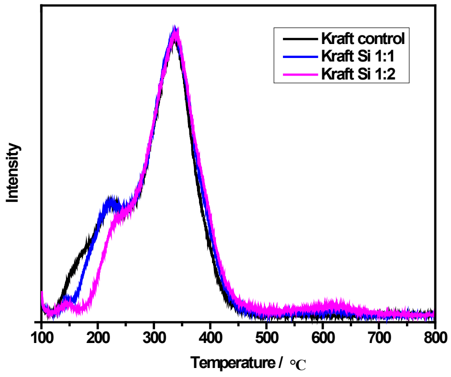

(c)

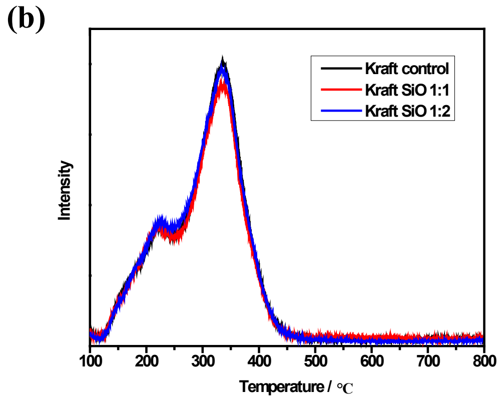

Figure 5.7 a) Fast pyrolysis of KL and KL/Si NPs (1:1) at 600 °C; EGA-MS profiles for pyrolysis of b) KL/Si NPs and c) KL/SiO NPs from 100 to 800 °C with a 2 °C/min ramp.

Table 5.S2 shows the yields of GC/MS detectable volatile compounds and solid residues from co-pyrolysis of KL and Si NPs at 2 °C/min ramp in the temperature regions of 100-500 °C and 500-800 °C, respectively, of which 40 compounds were identified and quantified. For comparison, as shown in **Table 5.1**, the 40 compounds evolved through pyrolysis of KL and KL/Si NPs from 100 to 800 °C at 2 °C/min were classified into seven categories and detailed formation mechanisms of each category from slow pyrolysis according to a previous study [37]. No noticeable difference in either composition or yield can be observed between pyrolysis of KL and KL/Si NPs in the temperature region of 100-500 °C, suggesting that the reactions was more related to lignin pyrolysis despite the interactions between Si NPs and C may have started playing a role. However, significant change in product distribution was observed in temperature region of 500-800 °C. The volatiles yield was 0.23 g/100g when just KL was pyrolyzed as compared to a yield of 2.5 g/100g when KL was co-pyrolyzed with Si NPs. The significant increase in volatiles yield in temperature region of 500-800 °C suggests possible interactions or even reactions between KL and Si NPs during co-pyrolysis. Among the volatiles, there are about 0.68 g/100g H and G-type compounds, such as phenol, methylphenol and 2-methoxy-4-

vinylphenol. Vinylphenols are believed to be the primary products of β-*O*-4 cleavage of lignin, while phenol and methylphenol are involved with the secondary reactions of vinylphenols via demothoxylation and demethylation reactions [37, 38]. The light phenolic compounds are probably derived from dimers, trimers or small oligomers which originally generated from lignin decomposition during pyrolysis at low temperature. Upon generation, the dimer, trimer or oligomers might be subject to interactions with Si NPs thus give rise to the R1-Si-O-C-R2. Due to the higher bond energy of Si-O, the R1-Si-O-C-R2 may not be depolymerized at temperatures under 500 °C; however, as temperature increases, the relatively weaker C-O bond starts to break. In addition to the phenolic compounds, around 1.69 g/100g hydrocarbon (mostly benzene, toluene and xylene) was produced during co-pyrolysis of KL/Si NPs at 500-800 °C, accounting for 66.27% of total phenolic compounds at this temperature region. The aromatic hydrocarbons could be formed either through dehydration of the phenolic compounds or via Diels–Alder reaction with light olefins, such as ethylene and propylene, at high temperature (above 700 °C) [218].

Table 5.1 Product distribution of KL and KL/Si NPs slow pyrolysis at two temperature regions

Compound name	100-500 °C		500-800 °C	
	KL, g/100g KL	KL/Si NPs, g/100g KL	KL, g/100g KL	KL/Si NPs, g/100g KL
Hydrocarbons	2.09 ± 0.15	1.85 ± 0.15	0.23 ± 0.16	1.69 ± 0.40
Carbohydrates	1.43 ± 0.51	1.58 ± 0.42	-	-
H-type substances	4.54 ± 0.14	4.74 ± 0.11	-	0.48 ± 0.16
G-type substances	12.05 ± 0.39	12.26 ± 0.69	-	0.20 ± 0.15
S-type substances	0.59 ± 0.05	0.64 ± 0.22	-	-
PAHs	1.54 ± 0.09	1.53 ± 0.12	-	0.18 ± 0.00
Others	1.65 ± 0.24	1.35 ± 0.32	-	-
Total volatiles yield	23.89 ± 1.57	23.95 ± 2.03	0.23 ± 0.16	2.55 ± 0.71 $_{p = 0.0053}$

The EGA-MS and HC-GC/MS analyses further confirm that the previous assumption - that adding Si NPs to KL affected the slow pyrolysis of KL by building up bonds between Si and C via O around the surface of the Si NPs. Thermal conversion temperature needs to be controlled to ensure a balanced ratio between Si-O and Si-C When KL/Si NPs (1 to 1) is pyrolyzed with a 2 ℃/min ramp, the formation of prepared C/Si composite can be divided into several phases in respect to temperature. At pyrolysis temperature far below 500 ℃, the reactions are primarily related to KL pyrolysis, which is followed by or coincides the formation of partially pyrolyzed lignin coating on the surface of Si NPs. When the temperature further increases to ~500 ℃, lignin was carbonized and the bonds between Si NPs and C via O were formed. As temperature increases to 500-800 ℃, more stable SiO_2 will gradually form on the surface of Si NPs at the expense of Si-O-C bond, which cause increase in the surface and interface stress of C/Si composite. The intense stress negatively affects both quality and uniformity of the lignin-derived C/Si composite electrode thus leads to reduced electrochemical performance [133].

Conclusions

In this study, a three-dimensional, interconnected C/Si composite was synthesized from kraft lignin and silicon nanoparticles through a one-pot pyrolysis process. It was found the elemental Si and C of the C/Si NPs were most likely linked via O rather than direct Si-C bond. The formed coating layer on the surface of Si NPs may serve to alleviate the mechanical degradation through either restricting excessive volume change during electrochemical cycling with chemical bond among Si, O, and C, or form a shell to protect the Si NP core from redundant lithiation. Additionally, the enriched carbon framework bridges the Si NPs to assure a sound electronic conductivity; while the porous carbonaceous layer surrounding the Si NPs allows Li ions to permeate the coating layer thus provides excellent ionic conductivity of the C/Si composite electrode. All of those contribute to an enhanced electronic performance. When examined as anode of LIBs, the lignin-derived C/Si NPs composite delivered a high initial specific capacity of 2932 mAh/g and a retaining capacity of 1760 mAh/g after 100 cycles at 0.72 A/g. EGA-MS and HC-GC/MS analysis suggest that the interaction of the Si, O and C can be tailored by controlling pyrolysis conditions.

Acknowledgements

This work was supported by the USDA National Institute of Food and Agriculture under project accession no. 1015068 and the National Science Foundation under Cooperative Agreements 1355438.

Electronic Supplemental Information

Understanding Lignin as Binder for Silicon-Based Lithium-ion Battery Negative Electrode

Kraft lignin characterization

Gel Permeation Chromatography (GPC)

For molecular weight measurement, KL was treated by the acetylation method[252]. Typically, 10 mg of KL was dissolved in 2.5 ml 92:8 (v/v) anhydrous acetic acid and acetyl bromide mixture with continuous stirring at 50 °C for 2 h. The acetic acid and excess acetyl bromide solvent were dried in N_2 before dissolved in tetrahydrofuran (THF). The molecular weight distribution of the lignin samples was determined by an HPLC system (Ultimate 3000, Dionex Corporation, Sunnyvale, CA, USA) equipped with an ultraviolet detector and an organic GPC column (PLgel 5 μm Mixed-D, Agilent Technologies, Santa Clara, CA, USA) using THF as mobile phase at a flow rate of 0.5 ml/min. The materials eluting from the column was monitored by recording absorbance at 290 nm. The chromatography was calibrated using low molecular weight polystyrene standards (Product No. 48937, Sigma-Aldrich).

2D $^{13}C-^{1}H$ HSQC NMR spectroscopic analysis

Nuclear magnetic resonance (NMR) spectra of lignin samples were acquired in a Bruker Avance III HD 500-MHz spectrometer. KL (~10 mg) were dissolved in 110 mg DMSO-d_6 before transferring to the micro-NMR tube. Heteronuclear single quantum coherence (HSQC) tests were carried out with a Bruker pulse sequence (hsqcetgpspsi2.2) on a N_2 cryoprobe (BBO 1H & 19F-5mm) with the following acquisition parameters: spectra width 12 ppm in F2 (^{1}H) dimension with 1024 data points (acquisition time 85.2 ms), 166 ppm in F1 (^{13}C) dimension with 256 increments (acquisition time 6.1 ms), a 1.0-s delay, a $^1J_{C–H}$ of 145 Hz, and 128 scans. The central DMSO-d_6 solvent peak (δ_C/δ_H at 39.5/2.49) was used for chemical shifts calibration. Assignment and the relative abundance of lignin compositional subunits and interunit linkage were estimated using volume integration of contours in HSQC spectra according to published literature [183, 185]. For volume integration of monolignol compositions of syringyl (S), guaiacyl (G), and *p*-hydroxyphenyl (H), the cross peaks of $S_{2/6}$, G_2, and $H_{2/6}$ contours were used with G_2 integrals doubled. The abundances of aromatics and side-chain linkages were presented as percentage of total aromatic SGH units.

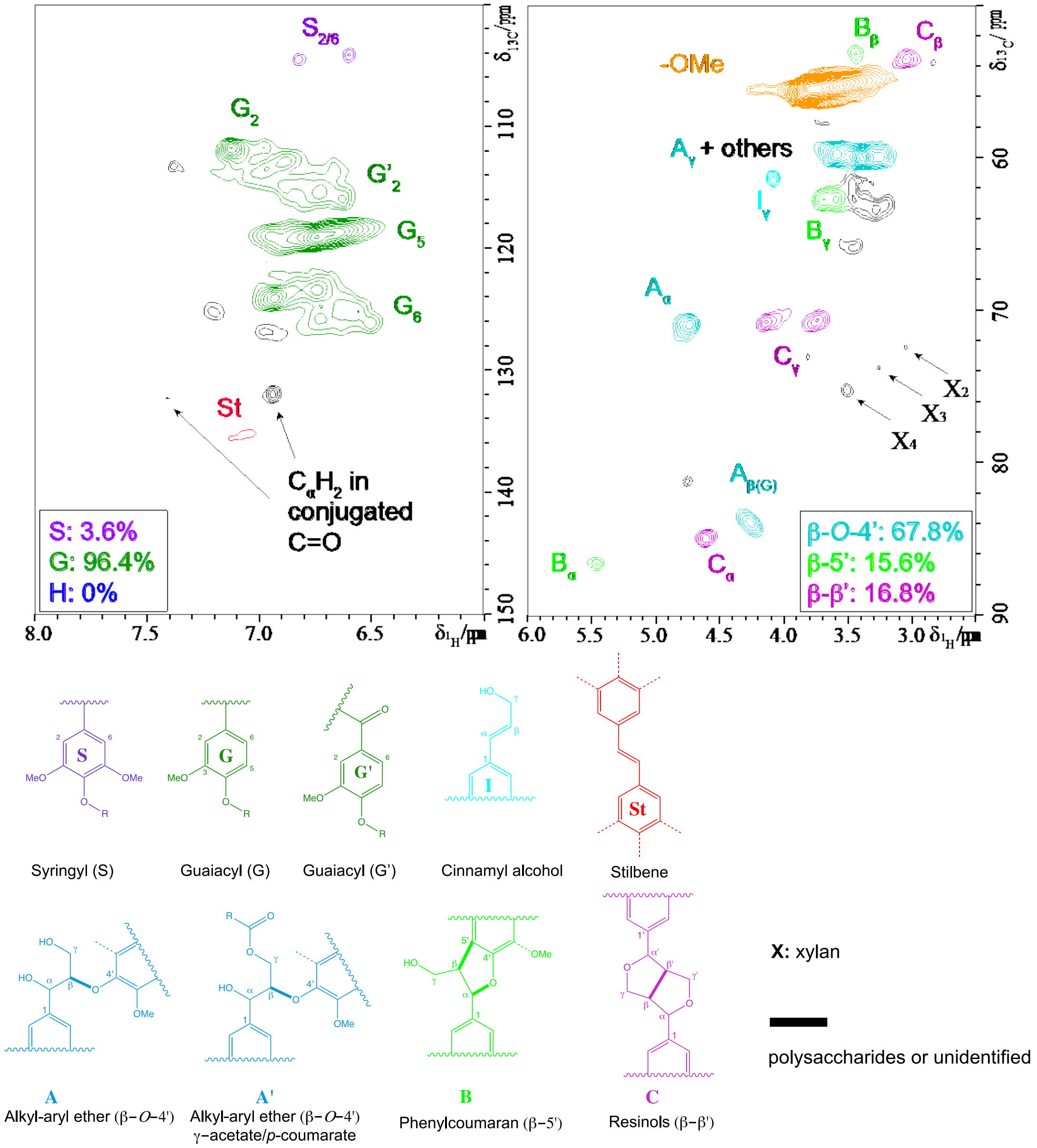

Figure 5.S1 ^{13}C-^{1}H (HSQC) spectra of aromatic (top) and aliphatic (bottom) regions of kraft lignin.

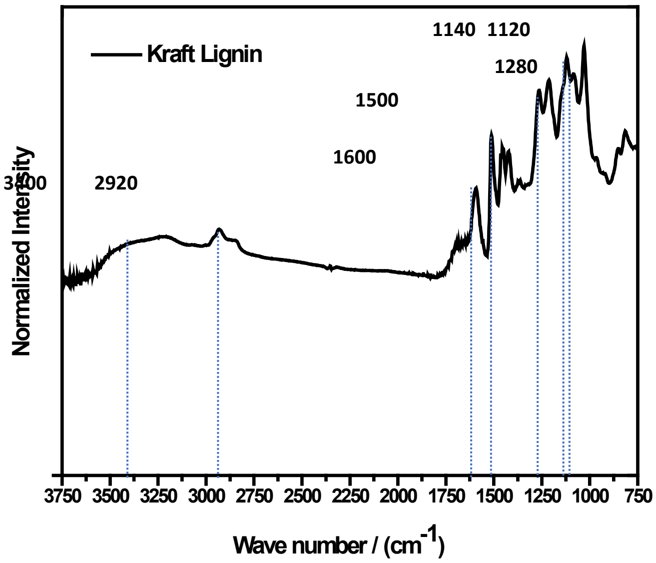

Figure 5.S2 FTIR spectra of kraft lignin.

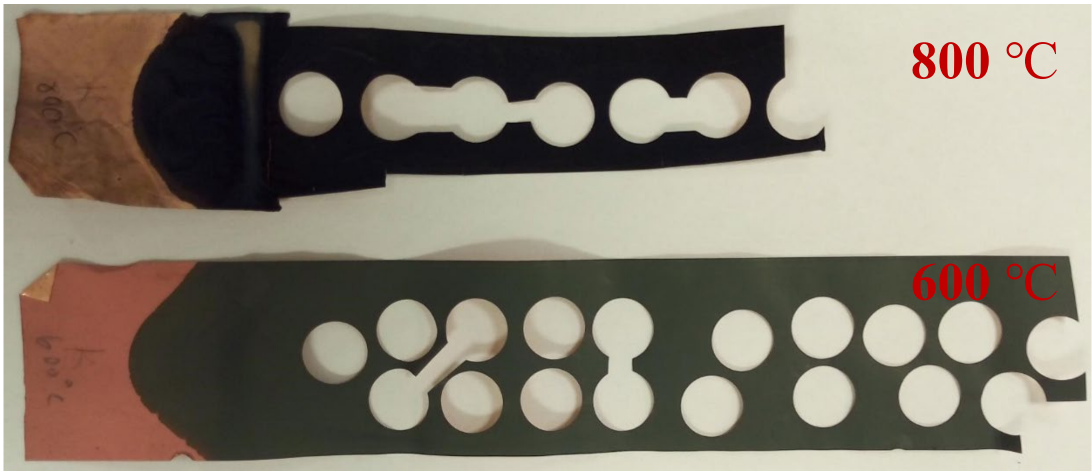

Figure 5.S3 Image of the C/Si NPs composite electrode from pyrolysis at 600 and 800 °C.

Table 5.S1 Molecular weight and composition analysis of kraft lignin

	M_w (g/mol)	M_n (g/mol)	PDI	Glucan (g/100g KL)	Xylan (g/100g KL)	Purity (%)
KL	5736.11	3056.34	1.88	0.11 ± 0.01	0.96 ± 0.03	98.94 ± 0.03

Table 5.S2 Product distribution of kraft lignin slow pyrolysis at multiple temperature regions

	Compound name	**100-500** °C (g/100g KL)		**500-800** °C (g/100g KL)	
		KL	KL/Si NPs	KL	KL/Si NPs
1	2-butene	0.69 ± 0.10	0.66 ± 0.04	0.01 ± 0.01	0.06 ± 0.02
2	acetone	0.07 ± 0.02	0.06 ± 0.02	-	-
3	benzene	0.37 ± 0.00	0.27 ± 0.01	0.14 ± 0.10	0.54 ± 0.11
4	acetic acid	0.47 ± 0.02	0.26 ± 0.01	-	-
5	toluene	0.65 ± 0.02	0.47 ± 0.03	0.07 ± 0.04	0.77 ± 0.17
6	3-furaldehyde	0.08 ± 0.00	0.08 ± 0.01	-	-
7	ethylbenzene	0.01 ± 0.00	0.01 ± 0.00	-	-
8	xylenes	0.32 ± 0.02	0.27 ± 0.05	0.01 ± 0.01	0.32 ± 0.10
9	phenol	1.61 ± 0.05	1.30 ± 0.06	-	0.21 ± 0.05
10	methylphenols	1.59 ± 0.02	1.71 ± 0.01	-	0.27 ± 0.11
11	guaiacol	1.11 ± 0.03	0.86 ± 0.03	-	-
12	dimethylphenols	1.08 ± 0.06	1.19 ± 0.06	-	-
13	creosol	2.09 ± 0.02	2019 ± 0.05		0.02 ± 0.02
14	3,4-dimethoxytoluene	0.12 ± 0.00	0.49 ± 0.02	-	-
15	1,2-bizenediol,3-methyl	0.46 ± 0.06	0.47 ± 0.06	-	-
16	4-ethyl-2-methoxyphenol	0.58 ± 0.05	0.33 ± 0.02	-	-
17	2-methoxy-4-vinylphenol	5.92 ± 0.15	6.73 ± 0.15	-	0.16 ± 0.12
18	2,6-dimethoxyphenol	0.34 ± 0.03	0.26 ± 0.17	-	-
19	trans-isoeugenol	-	0.10 ± 0.06	-	-
20	2-methoxy-4-propylphenol	0.07 ± 0.01	0.03 ± 0.01	-	-
21	4-Ethylcatechol	0.13 ± 0.02	0.08 ± 0.01	-	0.01 ± 0.00
22	vanillin	0.25 ± 0.04	0.30 ± 0.16	-	-
23	isoeugenol	0.76 ± 0.01	0.56 ± 0.02		0.01 ± 0.00
24	apocynin	0.22 ± 0.01	0.17 ± 0.01	-	-
25	benzene, 1,2,3-trimethoxy-5-methyl-	0.41 ± 0.06	0.45 ± 0.26	-	-
26	2-Propanone, 1-(4-hydroxy-3-methoxyphenyl)-	0.17 ± 0.02	0.16 ± 0.02	-	-
27	3,5-dimethoxyacetophenone	0.14 ± 0.02	0.07 ± 0.01	-	-
28	methyl homovanillate	0.03 ± 0.02	0.06 ± 0.04	-	-
29	3-Ethoxy-4-methoxybenzaldehyde	0.48 ± 0.08	0.40 ± 0.17	-	-
30	homovanillic acid	0.48 ± 0.02	0.49 ± 0.25	-	0.01 ± 0.01
31	2 6-dimethoxy-4-(2-propenyl)-phenol	0.23 ± 0.02	0.18 ± 0.02	-	-
32	Acetophenone, 4'-hydroxy-3,5-dimethoxyphenhl	-	0.11 ± 0.04	-	-
33	hexadecanoic acid	0.30 ± 0.11	0.26 ± 0.03	-	-
34	oleic acid	0.25 ± 0.21	0.34 ± 0.05	-	-
35	octadecanoic acid	0.21 ± 0.12	0.27 ± 0.02	-	-
36	2,3,8-thihydroxy-4-isopropyl-6-methyl-1-naphthaldehyde	0.15 ± 0.01	0.19 ± 0.06	-	-
37	6- methoxyhemigossypol	0.14 ± 0.02	0.15 ± 0.02	-	0.01 ± 0.00
38	5-methoxy-7-methylbenz(a)anthracene	0.59 ± 0.04	0.92 ± 0.45	-	-
39	secoisolariciresinol	-	0.33 ± 0.24	-	0.12 ± 0.00
40	benzo[vwx]hexaphene	0.59 ± 0.03	0.46 ± 0.09	-	0.05 ± 0.00
	Volatiles yield	23.18 ± 1.52	23.66 ± 2.85	0.23 ± 0.16	2.55 ± 0.71
	Char weight	N/A	N/A	48.72 ± 1.72	49.18 ± 2.49
	Total yield			72.13 ± 3.56	75.39 ± 5.34

CHAPTER 6. CONCLUSIONS AND FUTURE WORK

Conclusions

Aiming to unlock the full potential of lignin and fulfill lignocellulosic biorefineries' economic viability, in the present study, a practical strategy that convert lignin from the remaining by-product of biofuel production into energy storage material was mechanistically investigated. First of all, a novel lignin fractionation method to extract lignin from various biomass feedstocks was developed. Additionally, based on a fundamental investigation of slow pyrolysis, further investigations were performed on 1) the effect of lignin sources on the pore structure formation of lignin-derived ACs; and 2) the lignin-nanoparticle interactions during thermal processing and characterize the chemical, structural, mechanical and electrochemical proprieties of the derived nanocomposite materials. The knowledge acquired can be applied to improve electrochemical performance of lignin-derived activate carbon and nanocomposite materials for energy storage purpose and establishing processing-structure-function relationships to provide critical knowledge and guidance on designing lignin-based carbon materials for electrochemical energy storage applications.

Walnut and peach endocarps have high lignin content, bulk density, and energy density compared to other common biomass feedstocks due to the unique plant cell wall structures. DES pretreatment was shown to be an effective method to fractionate endocarps by depolymerizing the native lignin while at the same time keeping thermal stability. Over 90% sugar yields were achieved during enzymatic hydrolysis of DES pretreated peach and walnut endocarps while lignins were extracted at high yields and purity. The native walnut and peach CELs are SGH type lignin with dominant G units.

The DES pretreatment significantly removes the S and H unit while condenses the G unit. Meanwhile, nearly all β-*O*-4’ and a large portion of β-5’ linkages were removed; the relative abundance of β-β’ linkages in DES extracted lignin increased during DES pretreatment.

As for slow pyrolysis of lignin, vinylphenols are the primary products corresponding to cleavage of the β-*O*-4 linkages while the primary products underwent a series of secondary reactions and produce a variety of H, G and S type compounds. As heating rate increases, the volatile yield increased while solid residues yield decreased. With increasing pyrolysis temperature, specific surface areas of the lignin-derived solid residues increased. Pyrolysis breaks the primary ether linkages of lignin units and side chains, which contribute to the decrease of relative degree of aromaticity and polarity as pyrolysis temperature increases. Although elemental C increases and O reduces in respect to temperature, the oxygen-containing functional groups on the surface of solids increased significantly when pyrolysis temperature is higher than 600 °C.

When applied to electrode material of supercapacitors, lignin-derived AC exhibited a three-dimensional pore structure with numerous micro-, meso- and macro-porous channels. Comparing with pine (softwood) lignin-derived AC, poplar (hardwood) lignin-derived AC showed a higher level of specific surface area and volume of both mesopores and micropores, which contribute to a higher value of specific capacitance obtained from the poplar lignin-derived AC than the softwood lignin-derived AC.

Through slow pyrolysis, a 3-dimensional, interconnected C/Si composite can be synthesized from lignin and silicon nanoparticles. It was found the elemental Si and C of the C/Si NPs were most likely linked via O rather than direct Si-C bond. The formed coating layer on the surface of Si NPs may serve to alleviate the mechanical degradation through either restricting excessive volume change during electrochemical cycling with chemical bond among Si, O, and C, or form a shell to protect the Si NP core from redundant lithiation. In addition, the enriched carbon framework bridges the Si NPs to assure a sound electronic conductivity; while the porous carbonaceous layer surrounding the Si NPs allows Li ions to permeate the coating layer thus provides excellent ionic conductivity of the C/Si composite electrode. All of those contribute to an enhanced electronic performance. EGA-MS and HC-GC/MS analyses suggest that the interaction of the Si, O and C can be tailored by controlling pyrolysis conditions.

Future work

Although DES pretreatment was demonstrated to be an effective method to fractionate biomass for biorefineries to produce both biofuels and high-quality lignin streams, the cost is still too high. Therefore, reducing costs of DES pretreatment are critical for industrial application. Such efforts include finding low-cost and biocompatible precursors, pretreatment at high biomass loadings, process integration and intensification. Furthermore, the properties of the DES extract lignin need to be linked to performance of the carbon materials for electrochemical energy storage applications.

The effect of lignin pyrolysis on the resulting carbon material was investigated in this study. However, the connections between operation condition of activation process and lignin-derived AC as well as the possible interactions between carbonization and activation are not yet clear. Additionally, the variation of pyrolytic biochar and hydrothermal biochar to the functional material application has not been touched. Therefore, future work is needed to link the synthesis condition, properties and performance of functional materials.

This study points to several promising directions about tailoring the properties of synthesized C/Si composite for LIBs negative electrode or even lignin-derived carbon fibers via tuning pyrolysis condition. Since elemental O plays a significant role when synthesis C/Si composite for LIBs application, it will be interesting to study oxygen containing additives, such as PEO into the co-pyrolysis process. Instead of using inert carrier gas (argon), it might be possible to introduce partial oxygen or air into the atmosphere during pyrolysis. Additionally, systematical optimization of operation conditions will help to obtain improved electrochemical performance.

Finally, it is worthwhile evaluating feedstock logistics and economic potential of the developed lignin valorization strategy to aid the process design and optimization through coproducing lignin-derived carbon materials in a biorefinery. Simulation software such as Aspen Plus can be used for modeling the whole process with unit operations such as feedstock preprocessing, biomass fractionation, carbon material preparation, chemical recycling, and waste handling to calculate the energy and mass balances. The results will allow an assessment of the technical maturity and cost of the individual steps and overall process.

REFERENCES

1. Vincent, J., *From cellulose to cell.* Journal of Experimental Biology, 1999. **202**(23): p. 3263-3268.
2. Boerjan, W., J. Ralph, and M. Baucher, *Lignin biosynthesis.* Annual review of plant biology, 2003. **54**(1): p. 519-546.
3. Mansfield, S.D., et al., *Whole plant cell wall characterization using solution-state 2D NMR.* 2012. **7**(9): p. 1579.
4. Li, W., et al., *Fractionation and characterization of lignin streams from unique high-lignin content endocarp feedstocks.* 2018. **11**(1): p. 304.
5. Azadi, P., et al., *Liquid fuels, hydrogen and chemicals from lignin: A critical review.* Renewable and Sustainable Energy Reviews, 2013. **21**: p. 506-523.
6. Hatakeyama, H. and T. Hatakeyama, *Lignin structure, properties, and applications*, in *Biopolymers*. 2009, Springer. p. 1-63.
7. Li, C., et al., *Catalytic Transformation of Lignin for the Production of Chemicals and Fuels.* Chem Rev, 2015. **115**(21): p. 11559-624.
8. Chen, F. and R.A. Dixon, *Lignin modification improves fermentable sugar yields for biofuel production.* Nature biotechnology, 2007. **25**(7): p. 759-761.
9. Stevens, J.C. and J. Shi, *Biocatalysis in ionic liquids for lignin valorization: Opportunities and recent developments.* Biotechnology advances, 2019: p. 107418.
10. Grabber, J.H., *How do lignin composition, structure, and cross-linking affect degradability? A review of cell wall model studies.* Crop Science, 2005. **45**(3): p. 820-831.
11. Calvo‐Flores, F.G. and J.A. Dobado, *Lignin as renewable raw material.* ChemSusChem, 2010. **3**(11): p. 1227-1235.
12. U.S. Department of Energy, I.N.L., *Bioenergy Feedstock Library.* 2016.
13. Menind, A., et al., *Pretreatment and usage of pulp and paper industry residues for fuels production and their energetic potential.* Estonian Research Institute of Agriculture, 2012. **10**: p. 149-155.
14. Wyman, C.E., et al., *Comparative data on effects of leading pretreatments and enzyme loadings and formulations on sugar yields from different switchgrass sources.* Bioresource Technology, 2011. **102**(24): p. 11052-11062.
15. Yang, B. and C.E. Wyman, *Effect of xylan and lignin removal by batch and flowthrough pretreatment on the enzymatic digestibility of corn stover cellulose.* Biotechnology and bioengineering, 2004. **86**(1): p. 88-98.
16. Ragauskas, A.J., et al., *Lignin Valorization: Improving Lignin Processing in the Biorefinery.* Science, 2014. **344**(6185): p. 709-+.
17. Yoo, C.G., et al., *Effects of organosolv and ammonia pretreatments on lignin properties and its inhibition for enzymatic hydrolysis.* Green Chemistry, 2017. **19**(8): p. 2006-2016.
18. Rogers, R.D. and G.A. Voth, *Guest editorial-Ionic liquids*. 2007, AMER CHEMICAL SOC 1155 16TH ST, NW, WASHINGTON, DC 20036 USA.
19. Plechkova, N.V. and K.R. Seddon, *Ionic liquids:"designer" solvents for green*

chemistry. Vol. 105. 2007: Wiley: New York.

20. George, A., et al., *The effect of ionic liquid cation and anion combinations on the macromolecular structure of lignins.* Green chemistry, 2011. **13**(12): p. 3375-3385.
21. Alvira, P., et al., *Pretreatment technologies for an efficient bioethanol production process based on enzymatic hydrolysis: a review.* Bioresource technology, 2010. **101**(13): p. 4851-4861.
22. Humbird, D., et al., *Process design and economics for biochemical conversion of lignocellulosic biomass to ethanol: dilute-acid pretreatment and enzymatic hydrolysis of corn stover*. 2011, National Renewable Energy Laboratory (NREL), Golden, CO.
23. Tao, L., et al., *Process and technoeconomic analysis of leading pretreatment technologies for lignocellulosic ethanol production using switchgrass.* Bioresource technology, 2011. **102**(24): p. 11105-11114.
24. Zhang, Q., et al., *Deep eutectic solvents: syntheses, properties and applications.* Chemical Society Reviews, 2012. **41**(21): p. 7108-7146.
25. Francisco, M., A. van den Bruinhorst, and M.C. Kroon, *New natural and renewable low transition temperature mixtures (LTTMs): screening as solvents for lignocellulosic biomass processing.* Green Chemistry, 2012. **14**(8): p. 2153-2157.
26. Abbott, A.P., et al., *Deep eutectic solvents formed between choline chloride and carboxylic acids: versatile alternatives to ionic liquids.* Journal of the American Chemical Society, 2004. **126**(29): p. 9142-9147.
27. Florindo, C., et al., *Insights into the synthesis and properties of deep eutectic solvents based on cholinium chloride and carboxylic acids.* ACS Sustainable Chemistry & Engineering, 2014. **2**(10): p. 2416-2425.
28. Alvarez-Vasco, C., et al., *Unique low-molecular-weight lignin with high purity extracted from wood by deep eutectic solvents (DES): a source of lignin for valorization.* Green Chemistry, 2016. **18**(19): p. 5133-5141.
29. Behling, R., S. Valange, and G. Chatel, *Heterogeneous catalytic oxidation for lignin valorization into valuable chemicals: what results? What limitations? What trends?* Green Chemistry, 2016. **18**(7): p. 1839-1854.
30. Yang, B. and C.E. Wyman, *Pretreatment: the key to unlocking low‐cost cellulosic ethanol.* Biofuels, Bioproducts and Biorefining, 2008. **2**(1): p. 26-40.
31. Hashimoto, A., et al., *Direct evidence for atomic defects in graphene layers.* Nature, 2004. **430**(7002): p. 870.
32. Ebbesen, T. and P. Ajayan, *Large-scale synthesis of carbon nanotubes.* Nature, 1992. **358**(6383): p. 220.
33. Kroto, H.W., et al., *C60: Buckminsterfullerene.* nature, 1985. **318**(6042): p. 162-163.
34. Liu, W.J., H. Jiang, and H.Q. Yu, *Thermochemical conversion of lignin to functional materials: a review and future directions.* Green Chemistry, 2015. **17**(11): p. 4888-4907.
35. Zhu, J., et al., *A sustainable platform of lignin: From bioresources to materials and their applications in rechargeable batteries and supercapacitors.* Progress in Energy and Combustion Science, 2020. **76**: p. 100788.

36. Sen, S., S. Patil, and D.S. Argyropoulos, *Thermal properties of lignin in copolymers, blends, and composites: a review.* Green Chemistry, 2015. **17**(11): p. 4862-4887.
37. Wenqi Li, N.W., Xin Gao, Doo Young Kim, Jian Shi, *Understanding slow pyrolysis of lignin by linking the pyrolysis chemistry and material properties.* 2020.
38. Li, W., et al., *Understanding Low-pressure Hydropyrolysis of Lignin using Deuterated Sodium Formate.* ACS Sustainable Chemistry & Engineering, 2017.
39. Ferdous, D., et al., *Pyrolysis of lignins: experimental and kinetics studies.* Energy & Fuels, 2002. **16**(6): p. 1405-1412.
40. Yang, H., et al., *Characteristics of hemicellulose, cellulose and lignin pyrolysis.* Fuel, 2007. **86**(12-13): p. 1781-1788.
41. Patwardhan, P.R., *Understanding the Product Distribution from Biomass Fast Pyrolysis.* 2010.
42. Zhao, J., et al., *Thermal degradation of softwood lignin and hardwood lignin by TG-FTIR and Py-GC/MS.* Polymer degradation and stability, 2014. **108**: p. 133-138.
43. Asmadi, M., H. Kawamoto, and S. Saka, *Gas- and solid/liquid-phase reactions during pyrolysis of softwood and hardwood lignins.* Journal of Analytical and Applied Pyrolysis, 2011. **92**(2): p. 417-425.
44. Li, W., et al., *Linking lignin source with structural and electrochemical properties of lignin-derived carbon materials.* 2018. **8**(68): p. 38721-38732.
45. Sugimoto, Y. and Y. Miki. *Chemical structure of artificial coals obtained from cellulose, wood and peat*. in *Proceedings of the 9th International Conference on Coal Science ICCS*. 1997.
46. Van Krevelen, D.W., *Coal: typology, physics, chemistry, constitution*. 1993: Elsevier Amsterdam.
47. Pandey, A., et al., *Recent advances in thermochemical conversion of biomass*. 2015: Elsevier.
48. Funke, A. and F. Ziegler, *Hydrothermal carbonization of biomass: a summary and discussion of chemical mechanisms for process engineering.* Biofuels, Bioproducts and Biorefining, 2010. **4**(2): p. 160-177.
49. Kuster, B., *5‐Hydroxymethylfurfural (HMF). A review focussing on its manufacture.* Starch‐Stärke, 1990. **42**(8): p. 314-321.
50. Bergius, F., *Beiträge zur Theorie der Kohleentstehung.* Naturwissenschaften, 1928. **16**(1): p. 1-10.
51. Lau, F.S., et al., *Peat beneficiation by wet carbonization.* International journal of coal geology, 1987. **8**(1-2): p. 111-121.
52. Blazsó, M., et al., *The effect of hydrothermal treatment on a Merseburg lignite.* Fuel, 1986. **65**(3): p. 337-341.
53. Murray, J.a. and D. Evans, *The brown-coal/water system: Part 3. Thermal dewatering of brown coal.* Fuel, 1972. **51**(4): p. 290-296.
54. Terres, E., *Uber die Entwgsserung und Veredlung von Rohtorf und Rohbraumkohle.* Brennstoff-Chemie, 1952. **2**: p. 1-12.
55. Molton, P.M. and T. Demmitt, *Reaction mechanisms in cellulose pyrolysis: a*

literature review. 1977, Battelle Pacific Northwest Labs., Richland, WA (USA).

56. Knezevic, D., W.P.M. van Swaaij, and S.R. Kersten, *Hydrothermal conversion of biomass: I, glucose conversion in hot compressed water.* Industrial & Engineering Chemistry Research, 2009. **48**(10): p. 4731-4743.
57. Nelson, D.A., et al., *Application of direct thermal liquefaction for the conversion of cellulosic biomass.* Industrial & engineering chemistry product research and development, 1984. **23**(3): p. 471-475.
58. Boehm, H., *Some aspects of the surface chemistry of carbon blacks and other carbons.* Carbon, 1994. **32**(5): p. 759-769.
59. Kinoshita, K., *Carbon: electrochemical and physicochemical properties.* 1988.
60. Pandolfo, A. and A. Hollenkamp, *Carbon properties and their role in supercapacitors.* Journal of power sources, 2006. **157**(1): p. 11-27.
61. Bimer, J., et al., *Modified active carbons from precursors enriched with nitrogen functions: sulfur removal capabilities.* Fuel, 1998. **77**(6): p. 519-525.
62. Jurewicz, K., et al., *Ammoxidation of brown coals for supercapacitors.* Fuel Processing Technology, 2002. **77-78**: p. 191-198.
63. Jurewicz, K., et al., *Ammoxidation of active carbons for improvement of supercapacitor characteristics.* Electrochimica Acta, 2003. **48**(11): p. 1491-1498.
64. Cagniant, D., et al., *Structural characterization of nitrogen-enriched coals.* Energy & fuels, 1998. **12**(4): p. 672-681.
65. Carrott, P.J.M., et al., *Reactivity and porosity development during pyrolysis and physical activation in CO2 or steam of kraft and hydrolytic lignins.* Journal of Analytical and Applied Pyrolysis, 2008. **82**(2): p. 264-271.
66. Suhas, P.J.M. Carrott, and M.M.L.R. Carrott, *Using alkali metals to control reactivity and porosity during physical activation of demineralised kraft lignin.* Carbon, 2009. **47**(4): p. 1012-1017.
67. Liu, J., et al., *Three-dimensional hierarchical and interconnected honeycomb-like porous carbon derived from pomelo peel for high performance supercapacitors.* Journal of Solid State Chemistry, 2018. **257**: p. 64-71.
68. Wang, J. and S. Kaskel, *KOH activation of carbon-based materials for energy storage.* Journal of Materials Chemistry, 2012. **22**(45): p. 23710-23725.
69. Montané, D., V. Torné-Fernández, and V. Fierro, *Activated carbons from lignin: kinetic modeling of the pyrolysis of Kraft lignin activated with phosphoric acid.* Chemical Engineering Journal, 2005. **106**(1): p. 1-12.
70. Gonzalez-Serrano, E., et al., *Development of porosity upon chemical activation of kraft lignin with ZnCl2.* Industrial & engineering chemistry research, 1997. **36**(11): p. 4832-4838.
71. Saha, D., et al., *Studies on Supercapacitor Electrode Material from Activated Lignin-Derived Mesoporous Carbon.* Langmuir, 2014. **30**(3): p. 900-910.
72. Fierro, C.M., et al., *Colloidal templating synthesis and adsorption characteristics of microporous–mesoporous carbons from Kraft lignin.* Carbon, 2013. **62**: p. 233-239.
73. Gu, W. and G. Yushin, *Review of nanostructured carbon materials for electrochemical capacitor applications: advantages and limitations of activated*

carbon, carbide‐derived carbon, zeolite‐templated carbon, carbon aerogels, carbon nanotubes, onion‐like carbon, and graphene. Wiley Interdisciplinary Reviews: Energy and Environment, 2014. **3**(5): p. 424-473.

74. Winter, M. and R.J. Brodd, *What are batteries, fuel cells, and supercapacitors?* Chemical reviews, 2004. **104**(10): p. 4245-4270.
75. Tutorials, E., *Ultracapacitors.* 2019.
76. Zhai, Y.P., et al., *Carbon Materials for Chemical Capacitive Energy Storage.* Advanced Materials, 2011. **23**(42): p. 4828-4850.
77. C-Zhang, W.L., et al., *3D Hierarchical Porous Carbon for Supercapacitors Prepared from Lignin through a Facile Template-Free Method.* Chemsuschem, 2015. **8**(12): p. 2114-2122.
78. Wu, Y., et al., *One-step Preparation of Alkaline Lignin-based Activated Carbons with Different Activating Agents for Electric Double Layer Capacitor.* Int. J. Electrochem. Sci, 2017. **12**: p. 7227-7239.
79. Guo, N., et al., *Enzymatic hydrolysis lignin derived hierarchical porous carbon for supercapacitors in ionic liquids with high power and energy densities.* Green Chemistry, 2017. **19**(11): p. 2595-2602.
80. Navarro-Suárez, A.M., et al., *Nanoporous carbons from natural lignin: study of structural–textural properties and application to organic-based supercapacitors.* RSC Advances, 2014. **4**(89): p. 48336-48343.
81. Zhang, W., et al., *Hierarchical porous carbon derived from lignin for high performance supercapacitor.* Colloids and Surfaces A: Physicochemical and Engineering Aspects, 2015. **484**: p. 518-527.
82. Jeon, J.W., et al., *Controlling Porosity in Lignin‐Derived Nanoporous Carbon for Supercapacitor Applications.* ChemSusChem, 2015. **8**(3): p. 428-432.
83. Klose, M., et al., *Softwood lignin as a sustainable feedstock for porous carbons as active material for supercapacitors using an ionic liquid electrolyte.* ACS Sustainable Chemistry & Engineering, 2017. **5**(5): p. 4094-4102.
84. Li, H., et al., *Lignin-derived interconnected hierarchical porous carbon monolith with large areal/volumetric capacitances for supercapacitor.* Carbon, 2016. **100**: p. 151-157.
85. Ruiz‐Rosas, R., et al., *Electrochemical performance of hierarchical porous carbon materials obtained from the infiltration of lignin into zeolite templates.* ChemSusChem, 2014. **7**(5): p. 1458-1467.
86. Salinas-Torres, D., et al., *Asymmetric capacitors using lignin-based hierarchical porous carbons.* Journal of Power Sources, 2016. **326**: p. 641-651.
87. Ago, M., et al., *Mesoporous carbon soft-templated from lignin nanofiber networks: microphase separation boosts supercapacitance in conductive electrodes.* RSC Advances, 2016. **6**(89): p. 85802-85810.
88. Lai, C., et al., *Free-standing and mechanically flexible mats consisting of electrospun carbon nanofibers made from a natural product of alkali lignin as binder-free electrodes for high-performance supercapacitors.* Journal of Power Sources, 2014. **247**: p. 134-141.
89. Hu, S., et al., *High energy density supercapacitors from lignin derived submicron*

activated carbon fibers in aqueous electrolytes. Journal of Power Sources, 2014. **270**: p. 106-112.

90. Yang, J., et al., *Facile Preparation of Self-Standing Hierarchical Porous Nitrogen-Doped Carbon Fibers for Supercapacitors from Plant Protein–Lignin Electrospun Fibers.* ACS Omega, 2018. **3**(4): p. 4647-4656.
91. Zhang, L., et al., *Interconnected hierarchical porous carbon from lignin-derived byproducts of bioethanol production for ultra-high performance supercapacitors.* ACS applied materials & interfaces, 2016. **8**(22): p. 13918-13925.
92. Tian, J., et al., *Hierarchical S-doped porous carbon derived from by-product lignin for high-performance supercapacitors.* RSC Advances, 2017. **7**(20): p. 12089-12097.
93. Youe, W.-J., et al., *MnO2-deposited lignin-based carbon nanofiber mats for application as electrodes in symmetric pseudocapacitors.* International journal of biological macromolecules, 2018. **112**: p. 943-950.
94. Yu, B., A. Gele, and L. Wang, *Iron oxide/lignin-based hollow carbon nanofibers nanocomposite as an application electrode materials for supercapacitors.* International journal of biological macromolecules, 2018. **118**: p. 478-484.
95. Chen, F., et al., *Self-assembly of NiO nanoparticles in lignin-derived mesoporous carbons for supercapacitor applications.* Green Chemistry, 2013. **15**(11): p. 3057-3063.
96. Ye, W., et al., *Lignin as a green reductant and morphology directing agent in the fabrication of 3D graphene-based composites for high-performance supercapacitors.* Industrial crops and products, 2017. **109**: p. 410-419.
97. Peng, Z., et al., *High-performance biomass-based flexible solid-state supercapacitor constructed of pressure-sensitive lignin-based and cellulose hydrogels.* ACS applied materials & interfaces, 2018. **10**(26): p. 22190-22200.
98. Fang, W., et al., *Manufacture and application of lignin-based carbon fibers (LCFs) and lignin-based carbon nanofibers (LCNFs).* Green Chemistry, 2017. **19**(8): p. 1794-1827.
99. Cheng, Q., et al., *Graphene and nanostructured MnO2 composite electrodes for supercapacitors.* Carbon, 2011. **49**(9): p. 2917-2925.
100. Hadjipaschalis, I., A. Poullikkas, and V. Efthimiou, *Overview of current and future energy storage technologies for electric power applications.* Renewable and sustainable energy reviews, 2009. **13**(6-7): p. 1513-1522.
101. Musolino, V. and E. Tironi. *A comparison of supercapacitor and high-power lithium batteries*. in *Electrical Systems for Aircraft, Railway and Ship Propulsion (ESARS), 2010.* 2010. IEEE.
102. Evans, J.W.J.T.o.t.P.S., *V.—THE MEANINGS AND SYNONYMS OF PLUMBAGO.* 1908. **26**(2): p. 133-179.
103. Nitta, N., et al., *Li-ion battery materials: present and future.* 2015. **18**(5): p. 252-264.
104. Jian, Z., et al., *Insights on the mechanism of Na-ion storage in soft carbon anode.* Chemistry of Materials, 2017. **29**(5): p. 2314-2320.
105. Irisarri, E., A. Ponrouch, and M. Palacin, *Review—hard carbon negative*

electrode materials for sodium-ion batteries. Journal of The Electrochemical Society, 2015. **162**(14): p. A2476-A2482.

106. Franklin, R.E.J.P.o.t.R.S.o.L.S.A.M. and P. Sciences, *Crystallite growth in graphitizing and non-graphitizing carbons.* 1951. **209**(1097): p. 196-218.
107. Dahn, J.R., et al., *Mechanisms for lithium insertion in carbonaceous materials.* Science, 1995. **270**(5236): p. 590-593.
108. Gupta, A. and I.R. Harrison, *Small-angle X-ray scattering (SAXS) in carbonized phenolic resins.* Carbon, 1994. **32**(5): p. 953-960.
109. Flandrois, S. and B. Simon, *Carbon materials for lithium-ion rechargeable batteries.* Carbon, 1999. **37**(2): p. 165-180.
110. Stevens, D. and J.J.J.o.t.E.S. Dahn, *High capacity anode materials for rechargeable sodium - ion batteries.* 2000. **147**(4): p. 1271-1273.
111. Lu, H., X.J.S.E. Zhao, and Fuels, *Biomass-derived carbon electrode materials for supercapacitors.* 2017. **1**(6): p. 1265-1281.
112. Hayashi, H. and M. Satoh, *Secondary battery or cell with improved rechargeability*. 1986, Google Patents.
113. Xing, W., et al., *Correlation between lithium intercalation capacity and microstructure in hard carbons.* 1996. **143**(11): p. 3482-3491.
114. Wang, S.-X., et al., *Lignin-derived fused electrospun carbon fibrous mats as high performance anode materials for lithium ion batteries.* 2013. **5**(23): p. 12275-12282.
115. Zhang, W., et al., *Facile preparation of 3D hierarchical porous carbon from lignin for the anode material in lithium ion battery with high rate performance.* 2015. **176**: p. 1136-1142.
116. Yi, X., et al., *Graphene-like carbon sheet/Fe3O4 nanocomposites derived from soda papermaking black liquor for high performance lithium ion batteries.* 2017. **232**: p. 550-560.
117. Ma, D., Z. Cao, and A.J.N.-M.L. Hu, *Si-based anode materials for Li-ion batteries: a mini review.* 2014. **6**(4): p. 347-358.
118. Kovalenko, I., et al., *A major constituent of brown algae for use in high-capacity Li-ion batteries.* 2011. **334**(6052): p. 75-79.
119. Wang, Y., et al., *Influence of polymeric binders on mechanical properties and microstructure evolution of silicon composite electrodes during electrochemical cycling.* Journal of Power Sources, 2019. **425**: p. 170-178.
120. Nakagame, S., R.P. Chandra, and J.N. Saddler, *The effect of isolated lignins, obtained from a range of pretreated lignocellulosic substrates, on enzymatic hydrolysis.* Biotechnology and bioengineering, 2010. **105**(5): p. 871-879.
121. Pinson, M.B. and M.Z. Bazant, *Theory of SEI formation in rechargeable batteries: capacity fade, accelerated aging and lifetime prediction.* Journal of the Electrochemical Society, 2013. **160**(2): p. A243-A250.
122. Jin, Y., et al., *Challenges and Recent Progress in the Development of Si Anodes for Lithium - Ion Battery.* Advanced Energy Materials, 2017. **7**(23): p. 1700715.
123. Szczech, J.R. and S. Jin, *Nanostructured silicon for high capacity lithium battery anodes.* Energy & Environmental Science, 2011. **4**(1): p. 56-72.

124. Kim, H., et al., *Three‐dimensional porous silicon particles for use in high‐performance lithium secondary batteries.* Angewandte Chemie International Edition, 2008. **47**(52): p. 10151-10154.
125. Shin, J. and E. Cho, *Agglomeration mechanism and a protective role of Al2O3 for prolonged cycle life of Si anode in lithium-ion batteries.* Chemistry of Materials, 2018. **30**(10): p. 3233-3243.
126. Choi, J.Y., et al., *Silicon nanofibrils on a flexible current collector for bendable lithium‐ion battery anodes.* Advanced Functional Materials, 2013. **23**(17): p. 2108-2114.
127. Forney, M.W., et al., *Prelithiation of silicon–carbon nanotube anodes for lithium ion batteries by stabilized lithium metal powder (SLMP).* Nano letters, 2013. **13**(9): p. 4158-4163.
128. Chen, X., et al., *Reduction mechanism of fluoroethylene carbonate for stable solid–electrolyte interphase film on silicon anode.* ChemSusChem, 2014. **7**(2): p. 549-554.
129. Kovalenko, I., et al., *A major constituent of brown algae for use in high-capacity Li-ion batteries.* Science, 2011. **334**(6052): p. 75-79.
130. Bridel, J.-S., et al., *Key parameters governing the reversibility of Si/carbon/CMC electrodes for Li-ion batteries.* Chemistry of materials, 2009. **22**(3): p. 1229-1241.
131. Magasinski, A., et al., *Toward efficient binders for Li-ion battery Si-based anodes: polyacrylic acid.* ACS applied materials & interfaces, 2010. **2**(11): p. 3004-3010.
132. Wang, B., et al., *Adaptable silicon–carbon nanocables sandwiched between reduced graphene oxide sheets as lithium ion battery anodes.* ACS nano, 2013. **7**(2): p. 1437-1445.
133. Chen, T., et al., *Low-Temperature Treated Lignin as Both Binder and Conductive Additive for Silicon Nanoparticle Composite Electrodes in Lithium-Ion Batteries.* ACS applied materials & interfaces, 2016. **8**(47): p. 32341-32348.
134. Ng, S.H., et al., *Highly reversible lithium storage in spheroidal carbon‐coated silicon nanocomposites as anodes for lithium‐ion batteries.* Angewandte Chemie International Edition, 2006. **45**(41): p. 6896-6899.
135. Rios, O., et al., *Monolithic Composite Electrodes Comprising Silicon Nanoparticles Embedded in Lignin‐derived Carbon Fibers for Lithium‐Ion Batteries.* 2014. **2**(9‐10): p. 773-777.
136. Chen, T., et al., *Binder-free lithium ion battery electrodes made of silicon and pyrolized lignin.* Rsc Advances, 2016. **6**(35): p. 29308-29313.
137. Chen, T., et al., *High performance binder-free SiOx/C composite LIB electrode made of SiOx and lignin.* Journal of Power Sources, 2017. **362**: p. 236-242.
138. Obama, B., *The irreversible momentum of clean energy.* Science, 2017.
139. Chu, S. and A. Majumdar, *Opportunities and challenges for a sustainable energy future.* nature, 2012. **488**(7411): p. 294-303.
140. Ragauskas, A.J., et al., *Lignin Valorization: Improving Lignin Processing in the Biorefinery.* Science, 2014. **344**(6185).

141. Beckham, G.T., et al., *Opportunities and challenges in biological lignin valorization.* Current opinion in biotechnology, 2016. **42**: p. 40-53.

142. USDA. *The Fruit and Tree Nuts Yearbook.* 2016; Available from: https://www.ers.usda.gov/data-products/fruit-and-tree-nut-data/yearbook-tables/.

143. Mendu, V., et al., *Identification and thermochemical analysis of high-lignin feedstocks for biofuel and biochemical production.* Biotechnology for biofuels, 2011. **4**(1): p. 43.

144. Shi, J., et al., *Impact of mixed feedstocks and feedstock densification on ionic liquid pretreatment efficiency.* Biofuels, 2013. **4**(1): p. 63-72.

145. Shi, J., et al., *Impact of pretreatment technologies on saccharification and isopentenol fermentation of mixed lignocellulosic feedstocks.* BioEnergy Research, 2015. **8**(3): p. 1004-1013.

146. Mosier, N., et al., *Features of promising technologies for pretreatment of lignocellulosic biomass.* Bioresource Technology, 2005. **96**(6): p. 673-686.

147. Li, M., et al., *The effect of liquid hot water pretreatment on the chemical–structural alteration and the reduced recalcitrance in poplar.* Biotechnology for Biofuels, 2017. **10**(1): p. 237.

148. Esteghlalian, A., et al., *Modeling and optimization of the dilute-sulfuric-acid pretreatment of corn stover, poplar and switchgrass.* Bioresource Technology, 1997. **59**(2-3): p. 129-136.

149. Shi, J., M.A. Ebrik, and C.E. Wyman, *Sugar yields from dilute sulfuric acid and sulfur dioxide pretreatments and subsequent enzymatic hydrolysis of switchgrass.* Bioresource technology, 2011. **102**(19): p. 8930-8938.

150. Cui, Z., et al., *Comparison of alkaline- and fungi-assisted wet-storage of corn stover.* Bioresource Technology, 2012. **109**: p. 98-104.

151. Xu, J., et al., *Sodium hydroxide pretreatment of switchgrass for ethanol production.* Energy & Fuels, 2010. **24**(3): p. 2113-2119.

152. Silverstein, R.A., et al., *A comparison of chemical pretreatment methods for improving saccharification of cotton stalks.* Bioresource technology, 2007. **98**(16): p. 3000-3011.

153. Sympson, W., S. Nokes, and A. Hickman, *Recirculating calcium hydroxide solution: A practical choice for on-farm high solids lignocellulose pretreatment.* Industrial crops and products, 2017. **97**: p. 492-497.

154. Kim, K.H., et al., *Biomass Pretreatment using Deep Eutectic Solvent from Lignin derived Phenols.* Green Chemistry, 2018.

155. Kumar, A.K., B.S. Parikh, and M. Pravakar, *Natural deep eutectic solvent mediated pretreatment of rice straw: bioanalytical characterization of lignin extract and enzymatic hydrolysis of pretreated biomass residue.* Environmental Science and Pollution Research, 2016. **23**(10): p. 9265-9275.

156. Li, T., et al., *Deep Eutectic Solvents (DESs) for the Isolation of Willow Lignin (Salix matsudana cv. Zhuliu).* International journal of molecular sciences, 2017. **18**(11): p. 2266.

157. Mitra, P.P. and D. Loqué, *Histochemical staining of Arabidopsis thaliana secondary cell wall elements.* Journal of visualized experiments: JoVE, 2014(87).

158. O'brien, T., N. Feder, and M.E. McCully, *Polychromatic staining of plant cell walls by toluidine blue O.* Protoplasma, 1964. **59**(2): p. 368-373.
159. Mori, B. and L.M. Bellani, *Differential staining for cellulosic and modified plant cell walls.* Biotechnic & histochemistry, 1996. **71**(2): p. 71-72.
160. Liljegren, S., *Phloroglucinol stain for lignin.* Cold Spring Harbor Protocols, 2010. **2010**(1): p. pdb. prot4954.
161. Adler, E., *Lignin chemistry—past, present and future.* Wood science and technology, 1977. **11**(3): p. 169-218.
162. Rodrigues, P.R., et al., *Evaluation of buriti endocarp as lignocellulosic substrate for second generation ethanol production.* PeerJ PrePrints, 2018.
163. Fernandez-Bolanos, J., et al., *Steam-explosion of olive stones: hemicellulose solubilization and enhancement of enzymatic hydrolysis of cellulose.* Bioresource Technology, 2001. **79**(1): p. 53-61.
164. da Costa Sousa, L., et al., *'Cradle-to-grave'assessment of existing lignocellulose pretreatment technologies.* Current opinion in biotechnology, 2009. **20**(3): p. 339-347.
165. Wyman, C.E., *Biomass ethanol: technical progress, opportunities, and commercial challenges.* Annual review of energy and the environment, 1999. **24**(1): p. 189.
166. Procentese, A., et al., *Deep eutectic solvent pretreatment and subsequent saccharification of corncob.* Bioresource technology, 2015. **192**: p. 31-36.
167. Wang, S., et al., *Comparison of the pyrolysis behavior of lignins from different tree species.* Biotechnology Advances, 2009. **27**(5): p. 562-567.
168. Canetti, M., et al., *Thermal degradation behaviour of isotactic polypropylene blended with lignin.* Polymer Degradation and Stability, 2006. **91**(3): p. 494-498.
169. Burhenne, L., et al., *The effect of the biomass components lignin, cellulose and hemicellulose on TGA and fixed bed pyrolysis.* Journal of Analytical and Applied Pyrolysis, 2013. **101**: p. 177-184.
170. Faix, O., *Classification of lignins from different botanical origins by FT-IR spectroscopy.* Holzforschung-International Journal of the Biology, Chemistry, Physics and Technology of Wood, 1991. **45**(s1): p. 21-28.
171. Tejado, A., et al., *Physico-chemical characterization of lignins from different sources for use in phenol–formaldehyde resin synthesis.* Bioresource Technology, 2007. **98**(8): p. 1655-1663.
172. Wen, J.-L., et al., *Quantitative structures and thermal properties of birch lignins after ionic liquid pretreatment.* Journal of agricultural and food chemistry, 2013. **61**(3): p. 635-645.
173. Gordobil, O., et al., *Assesment of technical lignins for uses in biofuels and biomaterials: Structure-related properties, proximate analysis and chemical modification.* Industrial crops and products, 2016. **83**: p. 155-165.
174. García, A., et al., *Effect of ultrasound treatment on the physicochemical properties of alkaline lignin.* Chemical Engineering and Processing: Process Intensification, 2012. **62**: p. 150-158.
175. Song, Y., et al., *Gold-catalyzed conversion of lignin to low molecular weight*

aromatics. 2018. **9**(42): p. 8127-8133.

176. Lewandowski, A. and M. Galiński, *Carbon–ionic liquid double-layer capacitors*. Journal of Physics and Chemistry of Solids, 2004. **65**(2-3): p. 281-286.
177. Das, L.L., Mi; Stevens, Joseph; Li, Wenqi; Pu, Yunqiao; Ragauskas, Arthur; Shi, Jian, *Characterization and catalytic transfer hydrogenolysis of deep eutectic solvent extracted sorghum lignin to phenolic compounds*. ACS Sustainable Chemistry & Engineering, Forthcoming 2018.
178. Carlos Alvarez-Vasco, R.M., Melissa Quintero, Mond Guo, Scott Geleynse, Karthikeyan K. Ramasamy, Michael Wolcottc and Xiao Zhang, *Unique low-molecular-weight lignin with high purity extracted from wood by deep eutectic solvents (DES): a source of lignin for valorization*. Green Chemistry, 2016.
179. Sluiter, A., et al., *Determination of structural carbohydrates and lignin in biomass*. Laboratory analytical procedure, 2008. **1617**: p. 1-16.
180. Selig, M., N. Weiss, and Y. Ji, *Enzymatic Saccharification of Lignocellulosic Biomass: Laboratory Analytical Procedure (LAP): Issue Date, 3/21/2008*. 2008: National Renewable Energy Laboratory.
181. Ragauskas, A., et al., *Structural characterization of lignin in wild-type versus COMT down-regulated switchgrass*. Frontiers in Energy Research, 2014. **1**: p. 14.
182. Duval, A. and M. Lawoko, *A review on lignin-based polymeric, micro-and nano-structured materials*. Reactive and Functional Polymers, 2014. **85**: p. 78-96.
183. Yoo, C.G., et al., *Elucidating Structural Characteristics of Biomass using Solution‐State 2 D NMR with a Mixture of Deuterated Dimethylsulfoxide and Hexamethylphosphoramide*. ChemSusChem, 2016. **9**(10): p. 1090-1095.
184. Hu, Z., et al., *Elucidation of the structure of cellulolytic enzyme lignin*. Holzforschung, 2006. **60**(4): p. 389-397.
185. Sun, S.-L., et al., *Structural elucidation of sorghum lignins from an integrated biorefinery process based on hydrothermal and alkaline treatments*. Journal of agricultural and food chemistry, 2014. **62**(32): p. 8120-8128.
186. IPCC, *Special Report: Global Warming of 1.5 ℃*.
187. Administration, U.S.E.I., *Energy and the environment explained where greenhouse gases come from*. 2019, June 19.
188. Panwar, N., S. Kaushik, and S. Kothari, *Role of renewable energy sources in environmental protection: a review*. Renewable and Sustainable Energy Reviews, 2011. **15**(3): p. 1513-1524.
189. Sharma, R.K., et al., *Characterization of chars from pyrolysis of lignin*. 2004. **83**(11-12): p. 1469-1482.
190. Reti, C., et al., *Flammability properties of intumescent PLA including starch and lignin*. Polymers for Advanced Technologies, 2008. **19**(6): p. 628-635.
191. Brown, R.C. and T.R. Brown, *Biorenewable resources: engineering new products from agriculture*. 2013: John Wiley & Sons.
192. Peacocke, A.V.B.G.V.C., *Fast pyrolysis processes for biomass*. Renewable and Sustainable Energy Reviews, 2000. **4**: p. 2000.
193. Bridgewater, S.C.A.V., *Overview of Applications of Biomass Fast Pyrolysis Oil*. Energy & Fuels, 2004. **18**: p. 590-598.

194. Jiang, G., et al., *Effect of the temperature on the composition of lignin pyrolysis products.* 2010. **24**(8): p. 4470-4475.

195. Iatridis, B., et al., *Pyrolysis of a precipitated kraft lignin.* 1979. **18**(2): p. 127-130.

196. Hu, X., et al., *Acid-catalysed reactions between methanol and the bio-oil from the fast pyrolysis of mallee bark.* Fuel, 2012. **97**: p. 512-522.

197. Bai, X., et al., *Formation of phenolic oligomers during fast pyrolysis of lignin.* Fuel, 2014. **128**: p. 170-179.

198. Li, W., *Improving bio-oil quality and stability based on capping reactions.* 2016.

199. Zhou, S., *Understanding lignin pyrolysis reactions on the formation of mono-phenols and pyrolytic lignin from lignocellulosic materials*. 2013: Washington State University.

200. Demirbaş, A., *Mechanisms of liquefaction and pyrolysis reactions of biomass.* Energy Conversion and Management, 2000. **41**(6): p. 633-646.

201. Branca, C., et al., *GC/MS characterization of liquids generated from low-temperature pyrolysis of wood.* 2003. **42**(14): p. 3190-3202.

202. Murwanashyaka, J.N., H. Pakdel, and C. Roy, *Step-wise and one-step vacuum pyrolysis of birch-derived biomass to monitor the evolution of phenols.* Journal of Analytical and Applied Pyrolysis, 2001. **60**(2): p. 219-231.

203. Piskorz, J., P. Majerski, and D. Radlein. *Pyrolysis of Biomass–Aerosol Generation: Properties, Applications, and Significance for Process Engineers*. in *Biomass Conference of the Americas, 4th. Biomass: A Growth Opportunity in Green Energy and Value-Added Products, Elsevier Science, Oxford, UK, Oakland California*. 1999.

204. Patwardhan, P.R., R.C. Brown, and B.H.J.C. Shanks, *Understanding the fast pyrolysis of lignin.* 2011. **4**(11): p. 1629-1636.

205. Carrott, P. and M.R.J.B.t. Carrott, *Lignin–from natural adsorbent to activated carbon: a review.* 2007. **98**(12): p. 2301-2312.

206. Lu, H., et al., *Lignin as a binder material for eco-friendly Li-ion batteries.* Materials, 2016. **9**(3): p. 127.

207. Ma, Y., et al., *A biomass based free radical scavenger binder endowing a compatible cathode interface for 5 V lithium-ion batteries.* Energy & Environmental Science, 2019. **12**(1): p. 273-280.

208. Guo, F., Z.-L. Xiu, and Z.-X. Liang, *Synthesis of biodiesel from acidified soybean soapstock using a lignin-derived carbonaceous catalyst.* Applied energy, 2012. **98**: p. 47-52.

209. Zhao, X.-Y., et al., *Electric double-layer capacitors from activated carbon derived from black liquor.* Energy & Fuels, 2010. **24**(3): p. 1889-1893.

210. Sonibare, O.O., T. Haeger, and S.F. Foley, *Structural characterization of Nigerian coals by X-ray diffraction, Raman and FTIR spectroscopy.* Energy, 2010. **35**(12): p. 5347-5353.

211. Zhou, S., et al., *Lignin Valorization through Thermochemical Conversion: Comparison of Hardwood, Softwood and Herbaceous Lignin.* ACS Sustainable Chemistry & Engineering, 2016. **4**(12): p. 6608-6617.

212. Zhang, M., et al., *Pyrolysis of lignin extracted from prairie cordgrass, aspen, and Kraft lignin by Py-GC/MS and TGA/FTIR.* Journal of Analytical and Applied Pyrolysis, 2012. **98**: p. 65-71.
213. Demirbaş, A.J.E.c. and management, *Mechanisms of liquefaction and pyrolysis reactions of biomass.* 2000. **41**(6): p. 633-646.
214. Monteil-Rivera, F., et al., *Isolation and characterization of herbaceous lignins for applications in biomaterials.* Industrial Crops and Products, 2013. **41**: p. 356-364.
215. Harman-Ware, A.E., et al., *Pyrolysis–GC/MS of sinapyl and coniferyl alcohol.* 2013. **99**: p. 161-169.
216. Ledesma, E.B., et al., *Lumped kinetics for biomass tar cracking using 4-propylguaiacol as a model compound.* Industrial & Engineering Chemistry Research, 2015. **54**(21): p. 5613-5623.
217. Hosoya, T., H. Kawamoto, and S. Saka, *Role of methoxyl group in char formation from lignin-related compounds.* Journal of Analytical and Applied Pyrolysis, 2009. **84**(1): p. 79-83.
218. Cypres, R., *Aromatic hydrocarbons formation during coal pyrolysis.* Fuel processing technology, 1987. **15**: p. 1-15.
219. Richter, H., J.B.J.P.i.E. Howard, and C. science, *Formation of polycyclic aromatic hydrocarbons and their growth to soot—a review of chemical reaction pathways.* 2000. **26**(4-6): p. 565-608.
220. Zhou, H., et al., *Polycyclic aromatic hydrocarbon formation from the pyrolysis/gasification of lignin at different reaction conditions.* 2014. **28**(10): p. 6371-6379.
221. Ma, Z., E. Troussard, and J.A. van Bokhoven, *Controlling the selectivity to chemicals from lignin via catalytic fast pyrolysis.* Applied Catalysis A: General, 2012. **423**: p. 130-136.
222. Li, J., G. Henriksson, and G. Gellerstedt, *Lignin depolymerization/repolymerization and its critical role for delignification of aspen wood by steam explosion.* Bioresource technology, 2007. **98**(16): p. 3061-3068.
223. Chu, S., A.V. Subrahmanyam, and G.W.J.G.c. Huber, *The pyrolysis chemistry of a β-O-4 type oligomeric lignin model compound.* 2013. **15**(1): p. 125-136.
224. Petrakis, L. and D. Grandy, *Electron spin resonance spectrometric study of free radicals in coals.* Analytical Chemistry, 1978. **50**(2): p. 303-308.
225. Pineda, A. and A.F. Lee, *Heterogeneously catalyzed lignin depolymerization.* Applied Petrochemical Research, 2016. **6**(3): p. 243-256.
226. Barreiro, D.L., et al., *Molecular characterization and atomistic model of biocrude oils from hydrothermal liquefaction of microalgae.* Algal research, 2018. **35**: p. 262-273.
227. Reza, M.T., et al., *Pelletization of biochar from hydrothermally carbonized wood.* Environmental Progress & Sustainable Energy, 2012. **31**(2): p. 225-234.
228. Chen, B., et al., *Sorption of polar and nonpolar aromatic organic contaminants by plant cuticular materials: role of polarity and accessibility.* Environmental science & technology, 2005. **39**(16): p. 6138-6146.

229. Zhang, X., et al., *Carbon Nanostructure of Kraft Lignin Thermally Treated at 500 to 1000 °C.* Materials (Basel, Switzerland), 2017. **10**(8): p. 975.

230. Ferrari, A.C. and D.M. Basko, *Raman spectroscopy as a versatile tool for studying the properties of graphene.* Nature Nanotechnology, 2013. **8**: p. 235.

231. Wanninayake, N., et al., *Understanding the effect of host structure of nitrogen doped ultrananocrystalline diamond electrode on electrochemical carbon dioxide reduction.* Carbon, 2020. **157**: p. 408-419.

232. Wollbrink, A., et al., *Amorphous, turbostratic and crystalline carbon membranes with hydrogen selectivity.* Carbon, 2016. **106**: p. 93-105.

233. Li, Z., et al., *X-ray diffraction patterns of graphite and turbostratic carbon.* 2007. **45**(8): p. 1686-1695.

234. Woo, S.-W., et al., *Preparation of three dimensionally ordered macroporous carbon with mesoporous walls for electric double-layer capacitors.* Journal of Materials Chemistry, 2008. **18**(14): p. 1674-1680.

235. Fukuhara, K., et al., *Structure and catalysis of cellulose‐derived amorphous carbon bearing SO3H groups.* ChemSusChem, 2011. **4**(6): p. 778-784.

236. Carrott, P. and M.R. Carrott, *Lignin–from natural adsorbent to activated carbon: a review.* Bioresource technology, 2007. **98**(12): p. 2301-2312.

237. McMichael, A.J., *Global climate change and health: an old story writ large.* Climate change and human health: Risks and responses. Geneva, Switzerland: World Health Organization, 2003.

238. Thakur, V.K., et al., *Progress in green polymer composites from lignin for multifunctional applications: a review.* ACS Sustainable Chemistry & Engineering, 2014. **2**(5): p. 1072-1092.

239. Chakar, F.S. and A.J. Ragauskas, *Review of current and future softwood kraft lignin process chemistry.* Industrial Crops and Products, 2004. **20**(2): p. 131-141.

240. Strassberger, Z., S. Tanase, and G. Rothenberg, *The pros and cons of lignin valorisation in an integrated biorefinery.* RSC Advances, 2014. **4**(48): p. 25310-25318.

241. Tenhaeff, W.E., et al., *Highly Robust Lithium Ion Battery Anodes from Lignin: An Abundant, Renewable, and Low‐Cost Material.* Advanced Functional Materials, 2014. **24**(1): p. 86-94.

242. Simon, P. and Y. Gogotsi, *Materials for electrochemical capacitors.* Nature materials, 2008. **7**(11): p. 845-854.

243. Frackowiak, E., *Carbon materials for supercapacitor application.* Physical chemistry chemical physics, 2007. **9**(15): p. 1774-1785.

244. Brandt, A., et al., *Structural changes in lignins isolated using an acidic ionic liquid water mixture.* Green Chemistry, 2015. **17**(11): p. 5019-5034.

245. Liu, W.-J., H. Jiang, and H.-Q. Yu, *Thermochemical conversion of lignin to functional materials: a review and future directions.* Green Chemistry, 2015. **17**(11): p. 4888-4907.

246. Elmouwahidi, A., et al., *Activated carbons from KOH-activation of argan (Argania spinosa) seed shells as supercapacitor electrodes.* Bioresource Technology, 2012. **111**: p. 185-190.

247. Kubo, S. and J.F. Kadla, *Hydrogen bonding in lignin: a Fourier transform infrared model compound study.* Biomacromolecules, 2005. **6**(5): p. 2815-2821.
248. Shi, J., et al., *Impact of engineered lignin composition on biomass recalcitrance and ionic liquid pretreatment efficiency.* Green Chemistry, 2016. **18**(18): p. 4884-4895.
249. Chaturvedi, V. and P. Verma, *An overview of key pretreatment processes employed for bioconversion of lignocellulosic biomass into biofuels and value added products.* 3 Biotech, 2013. **3**(5): p. 415-431.
250. Gupta, R. and Y.Y. Lee, *Investigation of biomass degradation mechanism in pretreatment of switchgrass by aqueous ammonia and sodium hydroxide.* Bioresource Technology, 2010. **101**(21): p. 8185-8191.
251. Koo, B.-W., et al., *Structural changes in lignin during organosolv pretreatment of Liriodendron tulipifera and the effect on enzymatic hydrolysis.* Biomass and Bioenergy, 2012. **42**(Supplement C): p. 24-32.
252. Lu, F. and J. Ralph, *Derivatization followed by reductive cleavage (DFRC method), a new method for lignin analysis: protocol for analysis of DFRC monomers.* Journal of Agricultural and Food Chemistry, 1997. **45**(7): p. 2590-2592.
253. Mendu, V., et al., *Global bioenergy potential from high-lignin agricultural residue.* Proceedings of the National Academy of Sciences, 2012. **109**(10): p. 4014-4019.
254. Sun, Y. and J. Cheng, *Hydrolysis of lignocellulosic materials for ethanol production: a review.* Bioresource technology, 2002. **83**(1): p. 1-11.
255. Sluiter, A., et al., *Determination of ash in biomass: LAP-005 NREL analytical procedure.* National Renewable Energy Laboratory, Golden, 2004.
256. García, R., et al., *Spanish biofuels heating value estimation. Part II: Proximate analysis data.* Fuel, 2014. **117**: p. 1139-1147.
257. Nevárez, L.A.M., et al., *Biopolymer-based nanocomposites: effect of lignin acetylation in cellulose triacetate films.* Science and technology of advanced materials, 2011. **12**(4): p. 045006.
258. Mukkamala, S., et al., *Formate-Assisted Fast Pyrolysis of Lignin.* Energy & Fuels, 2012. **26**(2): p. 1380-1384.
259. Imel, A.E., A.K. Naskar, and M.D. Dadmun, *Understanding the impact of poly (ethylene oxide) on the assembly of lignin in solution toward improved carbon fiber production.* ACS applied materials & interfaces, 2016. **8**(5): p. 3200-3207.
260. Baker, D.A., N.C. Gallego, and F.S. Baker, *On the characterization and spinning of an organic‐purified lignin toward the manufacture of low‐cost carbon fiber.* Journal of Applied Polymer Science, 2012. **124**(1): p. 227-234.
261. Oh, Y.J., et al., *Oxygen functional groups and electrochemical capacitive behavior of incompletely reduced graphene oxides as a thin-film electrode of supercapacitor.* Electrochimica Acta, 2014. **116**(Supplement C): p. 118-128.
262. Pope, M.A., et al., *Supercapacitor electrodes produced through evaporative consolidation of graphene oxide-water-ionic liquid gels.* Journal of The Electrochemical Society, 2013. **160**(10): p. A1653-A1660.
263. Hosenuzzaman, M., et al., *Global prospects, progress, policies, and*

environmental impact of solar photovoltaic power generation. Renewable and Sustainable Energy Reviews, 2015. **41**: p. 284-297.

264. Cherubini, F., *The biorefinery concept: using biomass instead of oil for producing energy and chemicals.* Energy conversion and management, 2010. **51**(7): p. 1412-1421.
265. Hatakka, A., *Lignin-modifying enzymes from selected white-rot fungi: production and role from in lignin degradation.* FEMS microbiology reviews, 1994. **13**(2-3): p. 125-135.
266. Socha, A.M., et al., *Efficient biomass pretreatment using ionic liquids derived from lignin and hemicellulose.* Proceedings of the National Academy of Sciences of the United States of America, 2014. **111**(35): p. E3587-E3595.
267. Teki, R., et al., *Nanostructured silicon anodes for lithium ion rechargeable batteries.* Small, 2009. **5**(20): p. 2236-2242.
268. Liang, B., Y. Liu, and Y. Xu, *Silicon-based materials as high capacity anodes for next generation lithium ion batteries.* Journal of Power sources, 2014. **267**: p. 469-490.
269. Kim, H. and J. Cho, *Superior lithium electroactive mesoporous Si@ Carbon core− shell nanowires for lithium battery anode material.* Nano letters, 2008. **8**(11): p. 3688-3691.
270. Park, M.-H., et al., *Silicon nanotube battery anodes.* Nano letters, 2009. **9**(11): p. 3844-3847.
271. Tang, H., et al., *Porous reduced graphene oxide sheet wrapped silicon composite fabricated by steam etching for lithium-ion battery application.* Journal of Power Sources, 2015. **286**: p. 431-437.
272. Wang, J.-Z., et al., *Flexible free-standing graphene-silicon composite film for lithium-ion batteries.* Electrochemistry Communications, 2010. **12**(11): p. 1467-1470.
273. Luo, J., et al., *Crumpled graphene-encapsulated Si nanoparticles for lithium ion battery anodes.* The journal of physical chemistry letters, 2012. **3**(13): p. 1824-1829.
274. Wu, D., et al., *Two‐Dimensional Nanocomposites Based on Chemically Modified Graphene.* Chemistry–A European Journal, 2011. **17**(39): p. 10804-10812.
275. Fahmi, R., et al., *The effect of alkali metals on combustion and pyrolysis of Lolium and Festuca grasses, switchgrass and willow.* Fuel, 2007. **86**(10-11): p. 1560-1569.
276. Kubo, S., Y. Uraki, and Y. Sano, *Thermomechanical analysis of isolated lignins.* Holzforschung-International Journal of the Biology, Chemistry, Physics and Technology of Wood, 1996. **50**(2): p. 144-150.
277. Wright, J.T., et al., *Thermal oxidation of silicon in a residual oxygen atmosphere—the RESOX process—for self-limiting growth of thin silicon dioxide films.* Semiconductor Science and Technology, 2016. **31**(10): p. 105007.
278. Evstigneev, E., *Factors affecting lignin solubility.* Russian Journal of Applied Chemistry, 2011. **84**(6): p. 1040-1045.

279. Xu, Y., Y. Zhu, and C. Wang, *Mesoporous carbon/silicon composite anodes with enhanced performance for lithium-ion batteries.* Journal of materials chemistry A, 2014. **2**(25): p. 9751-9757.

280. Downs, R.T. and M. Hall-Wallace, *The American Mineralogist crystal structure database.* American Mineralogist, 2003. **88**(1): p. 247-250.

281. Endou, M., et al., *Method for providing a coating layer of silicon carbide on substrate surface*. 1985, Google Patents.

282. Dong, H., et al., *Structural and electrochemical characterization of Fe–Si/C composite anodes for Li-ion batteries synthesized by mechanical alloying.* Electrochimica acta, 2004. **49**(28): p. 5217-5222.

283. Yang, X., et al., *High-performance silicon/carbon/graphite composites as anode materials for lithium ion batteries.* Journal of the Electrochemical Society, 2006. **153**(7): p. A1341-A1344.

284. Voutsas, A., et al., *Raman spectroscopy of amorphous and microcrystalline silicon films deposited by low‐pressure chemical vapor deposition.* Journal of Applied Physics, 1995. **78**(12): p. 6999-7006.

285. Pimenta, M., et al., *Studying disorder in graphite-based systems by Raman spectroscopy.* Physical chemistry chemical physics, 2007. **9**(11): p. 1276-1290.

286. Santamaria, A., G. Falco, and M. De Commodo, *Raman Features Between Two Clases of Carbon Nanoparticles Generated in Ethylene Flames.* Meet. Ital. Sect. Combust. Inst, 2013: p. 2-7.

287. Mawhinney, D.B., J.A. Glass, and J.T. Yates, *FTIR study of the oxidation of porous silicon.* The Journal of Physical Chemistry B, 1997. **101**(7): p. 1202-1206.

288. Monsivais-Gámez, E., F. Ruiz, and J. Martínez, *Four-membered rings family in the Si–O extended rocking IR band from quantum chemistry calculations.* Journal of sol-gel science and technology, 2007. **43**(1): p. 65-72.

289. Scientific, T.F. *XPS Interpretation of Silicon*. 2019; Available from: https://xpssimplified.com/elements/silicon.php#appnotes.

290. Ma, D., Z. Cao, and A. Hu, *Si-based anode materials for Li-ion batteries: a mini review.* Nano-Micro Letters, 2014. **6**(4): p. 347-358.

291. Ryu, J.H., et al., *Failure modes of silicon powder negative electrode in lithium secondary batteries.* Electrochemical and solid-state letters, 2004. **7**(10): p. A306-A309.

292. Liang, H., et al., *Study of lithiated Nafion ionomer for lithium batteries.* Journal of applied electrochemistry, 2004. **34**(12): p. 1211-1214.

293. Li, J., R. Lewis, and J. Dahn, *Sodium carboxymethyl cellulose a potential binder for Si negative electrodes for Li-ion batteries.* Electrochemical and Solid-State Letters, 2007. **10**(2): p. A17-A20.

294. Chen, Z., L. Christensen, and J. Dahn, *Comparison of PVDF and PVDF-TFE-P as binders for electrode materials showing large volume changes in lithium-ion batteries.* Journal of The Electrochemical Society, 2003. **150**(8): p. A1073-A1078.

295. Xu, J., et al., *Unveiling the critical role of polymeric binders for silicon negative electrodes in lithium-ion full cells.* ACS applied materials & interfaces, 2017. **9**(4): p. 3562-3569.

296. Chen, L., et al., *Binder effect on cycling performance of silicon/carbon composite anodes for lithium ion batteries.* Journal of applied electrochemistry, 2006. **36**(10): p. 1099-1104.

297. Hu, J., et al., *Effects of adhesion and cohesion on the electrochemical performance and durability of silicon composite electrodes.* Journal of Power Sources, 2018. **397**: p. 223-230.

298. Riley, L.A., et al., *Improved mechanical integrity of ALD-coated composite electrodes for Li-ion batteries.* Electrochemical and Solid-State Letters, 2011. **14**(3): p. A29-A31.

299. libraries, T.L., *Bond Energies.* 2019, Sep 29.

300. Sun, C.Q., et al., *Bond-order–bond-length–bond-strength (bond-OLS) correlation mechanism for the shape-and-size dependence of a nanosolid.* Journal of Physics: Condensed Matter, 2002. **14**(34): p. 7781.

VITA

EDUCATION:

M.S., Mechanical Engineering, Iowa State University, 2014

M.S., Chemical Engineering, China University of Petroleum, Huadong, 2006

B.E., Mechanical Engineering, China University of Petroleum, Huadong, 2003

PROFESSIONAL EXPERIENCE:

Process Engineer, Process Engineering Laboratory, Petroleum Research Institute, China National Petroleum Corporation, Beijing, China: August 2006 to July 2014

AWARDS AND HONORS:

1. Boyd-Scott Graduate Research Award, 2nd place, America Society of Agricultural and Biological Engineers, 2018
2. Leading the Bioeconomy Graduate Fellowships, Iowa State University, 2014
3. Science and Technology Award of Petrochemical Research Institute, 3rd place, China National Petroleum Corporation, 2009
4. Science and Technology Award of Petrochemical Research Institute, 1st place, China National Petroleum Corporation, 2008

PUBLICATIONS:

1. Wenqi Li, Kirtley Amos, Mi Li, Yunqiao Pu, Seth Debolt, Yang-Tse Cheng, Arthur J Ragauskas, Jian Shi (2018), Fractionation and characterization of lignin streams from unique high-lignin content endocarp feedstocks, Biotechnology for Biofuels
2. Wenqi Li, Mi Li, Yan Zhang, Lalitendu Das, Yikai Wang, Yunqiao Pu, Doo Young Kim, Yang-Tse Cheng, Arthur J Ragauskas, Jian Shi (2018), Effect of the Structure and Source of Lignin Precursors on Activated Carbon for Energy Storage Application, Bioresource Technology
3. Lalitendu Das, Mi Li, Joseph Stevens, Wenqi Li, Yunqiao Pu, Arthur J. Ragauskas and Jian Shi (2018), Characterization and Catalytic Transfer

Hydrogenolysis of Deep Eutectic Solvent Extracted Sorghum Lignin to Phenolic Compounds, ACS Sustainable Chem. Eng.

4. Siquan Xu, Donghui Pan, Yuanfeng Wu, Xianghai Song, Lijing Gao, Wenqi Li, Lalitendu Das, Guomin Xiao (2018), Efficient production of furfural from xylose and wheat straw by bifunctional chromium phosphate catalyst in biphasic systems, Fuel Processing Technology
5. Wenqi Li, Shuai Zhou, Yuan Xue, Young-Jin Lee, Ryan Smith, and Xianglan Bai. (2017) Understanding Low-Pressure Hydropyrolysis of Lignin Using Deuterated Sodium Formate, ACS Sustainable Chem. Eng.
6. Luyao Zhang, Xuejing Li, Ming Qiao and Wenqi Li. (2009) Progress in Algae Biofuel Research and Development. Sino-Global Energy, 14: 23-26
7. Wenqi Li and Jianyi Chen. (2007) Experimental research of cyclone performance at high temperature, Frontiers of Mechanical Engineering in China, 2(3): 310-317

PROFESSIONAL PRESENTATION:

1. Wenqi Li, Yang-Tse Cheng, Jian Shi. (2019) Understanding co-pyrolysis of lignin with silicon nanoparticles, 2019 ASABE AIM, Jul 7-10, 2019
2. Wenqi Li, Yang-Tse Cheng, Jian Shi. (2019) Lignin derived carbon-silicon nanocomposite materials for energy storage applications, ACS spring 2019 National Meeting, March 31-Apr 4, 2019
3. Wenqi Li, Jian Shi. (2018) Characterization of deep eutectic solvent extracted lignin streams from endocarp biomass, 2018 AIChE annual meeting, Oct 28-Nov 2, 2018
4. Wenqi Li, Jian Shi. (2018) Fractionation and characterization of lignin streams from unique high-lignin content endocarp feedstocks, 2018 ASABE AIM, Jul 30-Aug 1, 2018
5. Wenqi Li, Yang-Tse Cheng, Jian Shi. (2018) Lignin-derived carbon and nanocomposite materials for energy storage applications, 2018 ASABE AIM, Jul 30-Aug 1, 2018

6. Wenqi Li, Lalitendu Das, Doo Young Kim, Yang-Tse Cheng, Arthur J Ragauskas, Jian Shi. (2017) Effects of Structure and Composition of Lignin on the Derived Activated Carbon Materials for Supercapacitor Application, 2017 ASABE AIM, Jul 16-19, 2017
7. Wenqi Li, Shuai Zhou, Xianglan Bai. (2015) Lignin Pyrolysis with Sodium Formate for Stabilization of Pyrolytic Products, AIChE 2015 Spring Meeting, Apr 26-30,2015